8-2023

Lepton Flavor Violation and Lepton Flavor Universality Violation: Opportunity for New Physics Beyond the Standard Model

Fang Xu
Washington University in St. Louis

Recommended Citation

Xu, Fang, "Lepton Flavor Violation and Lepton Flavor Universality Violation: Opportunity for New Physics Beyond the Standard Model" (2023). *Arts & Sciences Electronic Theses and Dissertations*. 3002.
https://openscholarship.wustl.edu/art_sci_etds/3002

WASHINGTON UNIVERSITY IN ST. LOUIS

Department of Physics

Dissertation Examination Committee:
Bhupal Dev, Chair
Francesc Ferrer
José E. Figueroa-López
Michael C. Ogilvie
Saori Pastore

Lepton Flavor Violation and Lepton Flavor Universality Violation: Opportunity for New Physics Beyond the Standard Model

by
Fang Xu

A dissertation presented to
Washington University in St. Louis
in partial fulfillment of the
requirements for the degree
of Doctor of Philosophy

August 2023
St. Louis, Missouri

Table of Contents

List of Figures

List of Tables

Publications

1. P. S. Bhupal Dev, Amarjit Soni and **Fang Xu**, “Hints of natural supersymmetry in flavor anomalies?”, Phys.Rev.D 106 (2022) 1, 015014 [arXiv: 2106.15647]
2. Yoav Afik, P. S. Bhupal Dev, Amarjit Soni and **Fang Xu**, “Probing the muon $(g-2)$ anomaly at the LHC in final states with two muons and two taus”, Phys.Lett.B 843 (2023) 138032 [arXiv: 2212.06160]
3. **Fang Xu**, “Neutral and Doubly-Charged Scalars at Future Lepton Colliders”, Phys.Rev.D 108 (2023) 3, 036002 [arXiv: 2302.08653]
4. P. S. Bhupal Dev, Amarjit Soni and **Fang Xu**, “R-parity Violating Supersymmetry and Neutrino Non-Standard Interactions”, [arXiv: 2308.abcde]
5. Wolfgang Altmannshofer, P. S. Bhupal Dev, Amarjit Soni and **Fang Xu**, “Electric Dipole Moments in the MSSM with R-Parity Violation”, [in preparation]

Acknowledgments

Completing my pursuit of a Ph.D. in Physics at Washington University in St. Louis has been a challenging and fulfilling journey. I am deeply grateful for the unwavering support of my advisor, my beloved family, and my friends, without whom this achievement would not have been possible. Therefore, I would like to take this opportunity to express my heartfelt appreciation to these incredibly significant individuals who have played pivotal roles during my study.

First, I would like to express my gratitude to the Department of Physics at Washington University in St. Louis for their support. Throughout my academic journey, the Department of Physics has provided me with a conducive learning and research environment, offering abundant academic resources and opportunities. The dedicated guidance from professors and the support of the department have laid a solid foundation for my academic growth and achievements. Thanks to the support of the Department of Physics at WashU, I have been able to delve into the field of High-Energy physics and pursue research outcomes. I would like to extend my heartfelt appreciation once again to the Department of Physics for their support and assistance.

I would like to express my heartfelt gratitude to Prof. Bhupal Dev for his invaluable support and guidance throughout these years. He has been instrumental in providing me with not only careful mentorship but also expert guidance in my research endeavors. His encouragement to participate in various conferences has broadened my horizons and expanded my knowledge in the High-Energy field. Whenever I had doubts or questions, Prof. Dev displayed immense patience and offered his unwavering support, which greatly enhanced my research skills. His profound expertise in various aspects of High-Energy physics has been invaluable in shaping my understanding of the subject. I am truly fortunate to have had Prof. Bhupal Dev as my advisor, and I am deeply grateful for his dedicated assistance and mentorship. I am incredibly grateful for the fruitful discussions I have had with Prof. Dev. Every interaction with him has been an enriching experience, resulting in substantial understanding. His insightful perspectives and profound knowledge in the field of Beyond the Standard Model Physics and Particle Astrophysics have consistently provided me with valuable insights and new ideas.

I would like to express my sincere gratitude to the members of my committee: Francesc Ferrer, Saori Pastore, Michael Ogilvie, and José Figueroa-López. In particular, I am deeply appreciative of the insightful suggestions and recommendations provided by Francesc and Saori during our Faculty Mentoring Committee Meetings. These meetings have been instrumental in shaping my research direction and enhancing the quality of my work. The discussions and interactions with Francesc, Saori, and Mike have also been immensely beneficial, allowing me to explore new ideas and receive valuable feedback. I am truly fortunate to have such dedicated and knowledgeable individuals on my committee, and I am grateful for their continuous support and engagement.

I am also deeply grateful to my collaborators, Amarjit Soni, Wolfgang Altmannshofer, and Yoav Afik, for their invaluable contributions to my academic and research journey. Their expertise and knowledge have been instrumental in expanding my understanding of physics and honing my research skills. In particular, I would like to express my deepest gratitude to Soni for his exceptional scientific guidance and the extensive discussions we have had throughout our collaborations. His mentorship has played a pivotal role in shaping my Ph.D. experience and has greatly contributed to my growth as a researcher. I am truly fortunate to have had the opportunity to work with such esteemed collaborators, and I am grateful for their impactful contributions to my academic and research endeavors. I would also like to acknowledge and express my appreciation to my fellow group members, Fapeng Huang, Yongchao Zhang, Garv Chauhan, and Yicong Sui. Our collaborative discussions have been incredibly fruitful, and I have benefited greatly from their insights and perspectives. Their contributions have played a significant role in shaping my research and enhancing my understanding. I am grateful for their support.

Most of all, I am deeply grateful to my family for their unwavering support and guidance throughout my life. They have been there for me during moments of confusion, providing insightful conversations that have helped me find clarity and direction. I am grateful for my parents' constant presence and encouragement which have made a significant support on my journey. Their guidance and accompany have made my Ph.D. life more fulfilling and enjoyable. I am truly fortunate to have such caring and supportive parents.

Fang Xu

Washington University in St. Louis
August 2023

Dedicated to my parents.

ABSTRACT OF THE DISSERTATION

Lepton Flavor Violation and Lepton Flavor Universality Violation: Opportunity for New Physics Beyond the Standard Model

by

Fang Xu

Doctor of Philosophy in Physics

Washington University in St. Louis, 2023

Professor Bhupal Dev, Chair

The Standard Model (SM) of Particle Physics has been remarkably successful in explaining the fundamental forces and classifying elementary particles. However, there are various experimental and theoretical indications that suggest the need to go beyond the SM (BSM) and expand our understanding of the fundamental nature of the universe. From a theoretical perspective, there are several limitations of the SM that suggest the existence of a more fundamental theory. For example, the SM does not incorporate gravity, and it fails to explain the hierarchy problem. Additionally, the nature of dark matter and the origin of the mass hierarchy of elementary particles remain unanswered questions.

To address these issues, numerous theoretical frameworks and models have been proposed as extensions of the SM, such as Supersymmetry (SUSY), Left-Right Symmetric Model (LRSM), and Extra Dimensions, etc. The BSM theories aim to provide explanations for the observed phenomena beyond the capabilities of the SM and offer new insights into the fundamental nature of the universe.

The main motivation behind this dissertation stems from the intriguing experimental results that have hinted at the possibility of Lepton Flavor Violation (LFV) and/or Lepton Flavor

Universality Violation (LFUV). These experimental observations deviate from the predictions of the Standard Model of Particle Physics, which assumes strict conservation of lepton flavors and lepton flavor universality.

In the first project, we address two types of intriguing phenomena that suggest the violation of Lepton Flavor Universality (LFU) within the framework of R-parity violating Supersymmetry (RPV SUSY). Firstly, we investigate the persistent indications of LFU violation in semileptonic decays of B-mesons, where experimental measurements deviate from the predictions of the Standard Model. Secondly, we focus on the long-standing discrepancy between the SM prediction and experimental measurements of the muon anomalous magnetic moment, which also suggests LFU violation. By employing the RPV SUSY framework, we propose theoretical solutions to reconcile these deviations between theory and experiment, aiming to reveal the underlying physics responsible for these anomalies. Thirdly, through our extensive numerical scan of the parameter space, we have identified a notable characteristic in our scenarios, namely the orthogonality between the parameter space of the sbottom and the parameter space of the sneutrino. This feature highlights the distinct nature of our proposed scenarios. Finally, we present two unique signals that can serve as potential tests at the LHC, enabling the exploration of the sbottom and sneutrino parameter spaces in our scenarios.

In the second project, building upon the insights gained from the first project regarding the orthogonality between the sbottom parameter space and the sneutrino parameter space in the sense that the sbottom plays a crucial role in addressing the B-physics anomalies, while the sneutrino primarily addresses the muon $(g-2)$ anomaly, we specifically concentrate on the muon $(g-2)$ anomaly. Again, within the RPV SUSY framework, we propose an alternative solution to address this discrepancy between theory and experiment. Furthermore, we propose and analyze distinctive signals that can be experimentally tested at the LHC, providing evidence for validating our proposed scenarios.

In certain scenarios, neutrino Non-Standard Interactions (NSI) can be induced from and interconnected with Lepton Flavor Violation. In the third project, we specifically concentrate on the LLE interactions in the framework of R-Parity Violating Supersymmetry. We consider various cases where different couplings, both Lepton Flavor Violating and Lepton Flavor Conserving, are non-zero. By investigating these cases, we provide a comprehensive analysis of the NSI parameters that can be contributed by LLE interaction terms under different conditions. This study shows the relationship between LFV and NSI within the context of RPV SUSY, offering valuable insights into the interplay between these phenomena.

In the fourth project, inspired by the Left-Right Symmetric Model, our project delves into the phenomenology of leptophilic new scalars. Specifically, we investigate the behavior and characteristics of electrically neutral and doubly-charged scalars at high-energy e^+e^- colliders, such as the International Linear Collider (ILC) and the Compact Linear Collider (CLIC). We consider both lepton flavor violating (LFV) and lepton flavor conserving (LFC) couplings. We define four distinct configurations representing different combinations of four lepton flavors in the final states in a model-independent manner. By studying multi-lepton final states, including LFV channels, with a center of mass energies ranging from 1 to 3 TeV, we present the sensitivity of the ILC/CLIC experiments in the relevant mass/coupling parameter space and exploit various di-lepton invariant mass distributions to effectively distinguish signal events from background processes.

Chapter 1: Introduction

Particle physics, also known as high-energy physics, plays a pivotal role in advancing our understanding of the fundamental nature of the universe. Through its investigations into the smallest building blocks of matter and the forces that govern them, particle physics unveils the mysteries of the cosmos and shapes our knowledge of the physical world. Its importance cannot be overstated, as it touches upon various aspects of science, technology, and even our philosophical understanding of reality.

Particle physics also drives technological advancements that impact our daily lives. The development of sophisticated particle detectors, such as the Large Hadron Collider (LHC), pushes the boundaries of engineering and computing. These technological breakthroughs find applications beyond the realm of particle physics, leading to advancements in different disciplines.

Beyond its scientific and technological significance, particle physics challenges our understanding of the fundamental nature of reality. It raises philosophical questions about the nature of existence, the fabric of space and time, and the underlying unity of the universe. Through the pursuit of knowledge at the smallest scales, particle physics expands our intellectual horizons and invites us to contemplate the mysteries of the cosmos.

1.1 Standard Model

The Standard Model (SM) of Particle Physics is a theoretical framework that describes the fundamental constituents of matter and their interactions through electromagnetic, weak, and strong forces. It provides a comprehensive understanding of the subatomic world and has been immensely successful in predicting and explaining experimental observations.

At the heart of the SM are the elementary particles, which are divided into two categories: fermions and bosons. Fermions are the building blocks of matter and can be further classified as quarks or leptons. Bosons, on the other hand, are force-carrying particles and mediate the interactions between fermions.

The Standard Model [1] is a non-abelian Yang-Mills gauge theory [2] that exhibits invariance under a local internal symmetry group known as $SU(3)_c \times SU(2)_L \times U(1)_Y$. This symmetry group corresponds to the conservation of specific charges: $SU(3)_c$ represents the color charge, $SU(2)_L$ represents the weak isospin, and $U(1)_Y$ represents the weak hypercharge. To be specific, the Quantum Chromodynamics (QCD) sector is governed by the symmetry group $SU(3)_c$, where the subscript "c" indicates interactions exclusively with particle species carrying the color charge. The Electroweak (EW) sector is characterized by the symmetry group $SU(2)_L \times U(1)_Y$, where the subscript "L" signifies interactions solely with left-handed fermions, and "Y" represents the weak hypercharge.

1.1.1 Electroweak Sector

The Electroweak theory [1, 3], formulated within the framework of the SM, is described by the Lagrangian that incorporates both electromagnetic and weak interactions:

$$\mathcal{L}_{\text{EW}} = \sum_{\psi} \bar{\psi} \gamma^{\mu} D_{\mu} \psi - \frac{1}{4} W_a^{\mu\nu} W_{\mu\nu}^a - \frac{1}{4} B^{\mu\nu} B_{\mu\nu}, \tag{1.1}$$

where the fermion field ψ represents the quarks and leptons, and the gauge fields associated with the electroweak symmetry group $SU(2)_L \times U(1)_Y$ are described by the field tensors $W_a^{\mu\nu}$ and $B^{\mu\nu}$:

$$W_a^{\mu\nu} = \partial^\mu W_a^\nu - \partial^\nu W_a^\mu + g\epsilon^{bca} W_b^\mu G_c^\nu, \tag{1.2}$$

$$B^{\mu\nu} = \partial^\mu B^\nu - \partial^\nu B^\mu. \tag{1.3}$$

The $W_a^{\mu\nu}$ field tensor transforms as $F^{\mu\nu} \to UF^{\mu\nu}U^{-1}$ under $SU(2)_L$, while the $B^{\mu\nu}$ field tensor transforms as $F^{\mu\nu} \to UF^{\mu\nu}U^{-1}$ under $U(1)_Y$. These field tensors are crucial in determining the interactions between the fermions and the gauge bosons.

The covariant derivative D_μ defined as

$$D_\mu = \partial_\mu - i\left(g_s G_\mu + gW_\mu^a \frac{\tau_a}{2} + g' B_\mu \frac{Y}{2}\right), \tag{1.4}$$

which incorporates the gauge fields, acts on the fermion fields to preserve the local gauge symmetry. Under a specific transformation, known as electroweak mixing,

$$\begin{pmatrix} A^\mu \\ Z^\mu \end{pmatrix} = \begin{pmatrix} \cos\theta_W & \sin\theta_W \\ -\sin\theta_W & \cos\theta_W \end{pmatrix} \begin{pmatrix} B^\mu \\ W_3^\mu \end{pmatrix}, \tag{1.5}$$

the B field and the W_3 field combine to give rise to two well-known particles: the photon and the Z boson.

In the electroweak theory, the fermion fields are often classified according to their left- and right-handed components, which exhibit distinct transformation properties under the $SU(2)_L \times U(1)_Y$ gauge group [4].

$$Q_L = \begin{pmatrix} u_L \\ d_L \end{pmatrix} := (2, 1/3), \tag{1.6}$$

$$u_R := (1, 4/3), \tag{1.7}$$

$$d_R := (1, -2/3), \tag{1.8}$$

for quarks, and

$$L_l = \begin{pmatrix} \nu_{eL} \\ \ell_{eL} \end{pmatrix} := (2, -1), \tag{1.9}$$

$$\ell_{eR} := (1, -2), \tag{1.10}$$

for leptons. These fermion fields are typically denoted with numbers in parentheses, representing their transformation properties under $SU(2)_L$ and $U(1)_Y$, respectively.

1.1.2 Higgs Mechanism

The electroweak theory, which combines electromagnetic and weak interactions, introduces the Higgs mechanism to explain the origin of particle masses and the breaking of electroweak symmetry [5, 6, 7, 8, 9, 10]. The Higgs field is unique in that its vacuum expectation value does not vanish, leading to the spontaneous breaking of electroweak symmetry. The Higgs mechanism is a fundamental concept in the Standard Model of Particle Physics, where it is based on the addition of a complex scalar Higgs field

$$\Phi = \begin{pmatrix} \phi^+ \\ \phi^0 \end{pmatrix}. \tag{1.11}$$

In order to maintain gauge invariance and ensure renormalizability, the Lagrangian for the Higgs field is structured as

$$\mathcal{L}_{\text{Higgs}} = \left(D_\mu \Phi\right)\left(D^\mu \Phi\right) + \frac{1}{2}\mu^2 \Phi\Phi - \frac{1}{4}\lambda_h (\Phi\Phi)^2, \tag{1.12}$$

which includes kinetic and potential terms that govern the dynamics and spontaneous symmetry breaking properties. For a positive μ^2, this scalar field undergoes a process known as spontaneous symmetry breaking, where it acquires a non-zero vacuum expectation value (VEV)

$$\langle \Phi \rangle = \begin{pmatrix} 0 \\ \frac{v}{\sqrt{2}} \end{pmatrix}. \tag{1.13}$$

The breaking of electroweak symmetry results in the generation of three massive gauge bosons: the $W^\pm$ and Z bosons

$$m_W = \frac{1}{2} v g \tag{1.14}$$

$$m_Z = \frac{1}{2} v \sqrt{g^2 + g'^2} \tag{1.15}$$

where g is the $SU(2)_L$ gauge coupling, and g' is the $U(1)_Y$ gauge coupling.

1.1.3 Yukawa Interaction

In order to give mass to fermions within the Standard Model, people introduce the Yukawa interaction between fermion fields and the Higgs field

$$\mathcal{L}_{\text{Yukawa}} = -\left((y_\ell)_{ij} \bar{L}_{L_i} \Phi \ell_{R_j} + (y_d)_{ij} \bar{Q}_{L_i} \Phi d_{R_j} + (y_u)_{ij} \bar{Q}_{L_i} \widetilde{\Phi} u_{R_j}\right) + \text{ H.c. }, \tag{1.16}$$

where $\widetilde{\Phi} = i\tau_2\Phi^*$ and the indices i and j in the Yukawa interaction terms represent the generation indices of the fermions involved in the interaction.

The Yukawa interaction provides a mechanism for the fermions to acquire mass through their coupling to the Higgs field. After spontaneous symmetry breaking, the Lagrangian is given by

$$\mathcal{L}_{\text{Yukawa}} = -\frac{(y_\ell)_{ij} v}{\sqrt{2}} \bar{\ell}_{L_i} \ell_{R_j} - \frac{(y_d)_{ij} v}{\sqrt{2}} \bar{d}_{L_i} d_{R_j} - \frac{(y_u)_{ij} v}{\sqrt{2}} \bar{u}_{L_i} u_{R_j} + \text{ H.c. } . \tag{1.17}$$

Hence, the fermion mass matrices can be obtained by multiplying the vacuum expectation values (VEVs) with the corresponding Yukawa coupling matrices. Therefore, after spontaneous symmetry breaking, the Lagrangian undergoes a transformation and takes on a new form. In this new form, the fermion mass matrices can be derived by combining the vacuum expectation values (VEVs) of the Higgs field with the corresponding Yukawa coupling matrices. This mechanism allows for the generation of mass for fermions, as the interaction between the fermion fields and the Higgs field leads to the multiplication of the VEVs and the Yukawa coupling matrices. By incorporating these elements, the theory provides a framework for understanding the origins of fermion masses within the Standard Model.

At this stage, we can summarize the Lagrangian as the sum of all the different components we have introduced thus far

$$\mathcal{L}_{\text{SM}} = \mathcal{L}_{\text{fermion}} + \mathcal{L}_{\text{gauge}} + \mathcal{L}_{\text{Higgs}} + \mathcal{L}_{\text{Yukawa}} . \tag{1.18}$$

This comprehensive Lagrangian encapsulates the interactions and dynamics of the fundamental particles and fields in the Standard Model. It serves as the mathematical framework that allows us to describe and understand the behavior of particles and their interactions according to the principles of the Standard Model.

1.2 Lepton Flavor Violation and Lepton Flavor Universality Violation

1.2.1 Lepton Flavor and Lepton Flavor Universality in the Standard Model

The concept of Lepton Flavor Universality (LFU) is a fundamental principle within the framework of the Standard Model of Particle Physics. It posits that the three families of leptons, namely the electron, muon, and tau, are equivalent in terms of their interactions and couplings, except for their differences in mass. The leptonic Yukawa couplings are the primary cause of the Lepton Flavor Universality Violation in the Standard Model. This principle has been extensively tested and confirmed by experimental observations in various processes involving leptons.

To be specific, Eq. (1.18) can be further summarized as follows:

$$\mathcal{L}_{\text{SM}} = \mathcal{L}_{\text{SM-Yukawa}} + \mathcal{L}_{\text{Yukawa}} . \tag{1.19}$$

where $\mathcal{L}_{\text{SM-Yukawa}}$ exhibits an accidental global symmetry of $U(3)_q \times U(3)_u \times U(3)_d \times U(3)_\ell \times U(3)_e$ [11]. However, this symmetry gets broken due to the presence of the Yukawa terms in $\mathcal{L}_{\text{Yukawa}}$.

Upon closer examination of the lepton sector, the $U(1)_e \times U(1)_\mu \times U(1)_\tau$ group that corresponds to the Lepton Flavor symmetry and the $U(3)_L$ group that corresponds to the

Lepton Flavor Universality symmetry are the subgroups of the accidental $U(3)_\ell \times U(3)_e$ symmetry of $\mathcal{L}_{\text{SM-Yukawa}}$. The Lepton Flavor symmetry would be preserved if the Yukawa matrix y_ℓ in Eq. (1.17) possessed a diagonal form. Furthermore, the Lepton Flavor Universality symmetry would be preserved if the Yukawa matrix y_ℓ in Eq. (1.17) is proportional to the identity matrix.

Considering the fact that $y_\ell \ll$ gauge couplings, Lepton Flavor Universality is a highly accurate symmetry in the Standard Model, with only a minor violation caused by the small Yukawa couplings. The symmetry $U(1)_e \times U(1)_\mu \times U(1)_\tau$ is explicitly broken when neutrino masses are introduced. However, even when considering the neutrino masses, the Lepton Flavor symmetry remains an excellent approximate symmetry due to the tiny values of the neutrino masses.

Since the Lepton Flavor symmetry group $U(1)_e \times U(1)_\mu \times U(1)_\tau$ is a subgroup of the Lepton Flavor Universality symmetry group $U(3)_L$, any violation in Lepton Flavor necessarily implies a violation in Lepton Flavor Universality. However, the reverse is not true, as a violation of Lepton Flavor Universality does not necessarily imply a violation of Lepton Flavor.

1.2.2 Experimental Investigations

1.2.2.1 Lepton Flavor Universality Violation

The possibility of violations of Lepton Flavor Universality has been a subject of great interest and investigation in the context of models beyond the Standard Model. These violations could arise from the presence of new physics particles that couple preferentially to certain generations of leptons.

The exploration of LFV and LFUV in high-energy physics experiments provides a unique opportunity to probe new physics beyond the Standard Model. Through careful analysis of the patterns exhibited by lepton flavor-changing processes and their comparison with theoretical predictions, significant insights can be gained regarding the fundamental physics underlying these phenomena. Such investigations offer an opportunity to explore and unravel new theoretical frameworks, facilitating a deeper understanding of the fundamental nature of particles and their interactions.

Experimental studies have been carried out to search for potential violations of lepton flavor universality in various processes, such as decays of B mesons and tau leptons, as well as in measurements of the muon anomalous magnetic moment. The observed discrepancies between the SM predictions and experimental results in some of these processes have sparked considerable excitement and motivated further investigations into possible explanations within the realm of new physics.

Intriguing evidence of Lepton Flavor Universality Violation has been seen in a number of processes in recent years. Notably, this violation has been seen in the charged current (CC) tree-level process in $b \to c\ell\nu$ and the neutral current (NC) loop-level process in $b \to s\ell\ell$. These observations combined imply a convincing pattern of anomalies. If these anomalies are confirmed, it might be the first instance of physics that deviates from the Standard Model. The exploration of these anomalies opens up new avenues for investigating and understanding the fundamental principles underlying particle interactions beyond the Standard Model.

Measurements of the Lepton Flavor Universality ratios R_D and R_{D^*}, conducted by experiment collaborations such as BaBar [12, 13], LHCb [14, 15], and Belle [16, 17, 18, 19], have revealed significant deviations from the predictions of the Standard Model. The combined analysis of these measurements indicates a significant deviation from the SM at a level of approximately 3 - 4 standard deviations. The LFU observables R_D and R_{D^*} are defined as follows:

$$R_{D^{(*)}} = \frac{\mathrm{BR}(B \to D^{(*)}\tau\nu)}{\mathrm{BR}(B \to D^{(*)}\ell\nu)}, \tag{1.20}$$

where $\ell = e, \mu$. The consistent nature of these deviations across different experiments highlights the potential presence of new physics phenomena that go beyond the established framework of the SM.

There are also several measurements conducted by the LHCb collaboration have shown notable deviations from the predictions of the Standard Model, with a significance level of approximately 2 - 3 standard deviations. These observed deviations also provide strong indications of physics beyond the SM. The discrepancies are observed in various observables, such as angular distributions in $B \to K^*\mu^+\mu^-$ [20, 21] and branching fractions of the decay processes $B \to K\mu^+\mu^-$, $B \to K^*\mu^+\mu^-$, and $B_s \to \phi\mu^+\mu^-$ [22, 23, 24, 25]. When considering the combined measurements of the LFU ratios, R_K and R_{K^*} [26, 27, 28, 29], a significant deviation of around 3 σ from the predictions of the Standard Model is observed [1]. This means that the observed values of these ratios, which are associated with the $b \to s\ell\ell$ transitions in rare B meson decays suggest the possibility of new physics phenomena influencing these decay processes. The LFU observables R_K and R_{K^*} are defined as follows:

$$R_{K^{(*)}} = \frac{\mathrm{BR}(B \to K^{(*)}\mu^+\mu^-)}{\mathrm{BR}(B \to K^{(*)}e^+e^-)}. \tag{1.21}$$

Another long-standing anomaly that also hints at the violation of Lepton Flavor Universality is the discrepancy between the SM and experimental values of the muon anomalous magnetic moment, $(g-2)_\mu$. The measurement of the anomalous magnetic moment of the muon, conducted at Brookhaven National Laboratory (BNL) [32] and Fermi National Accelerator Laboratory (FNAL) [33], exhibit a significant combined deviation of 4.2 σ from the

---

[1] In light of the recent LHCb result, it agrees with the SM now [30, 31]. But they still have 3σ anomaly in the angular observables.

predictions of the Standard Model. This notable deviation implies that the experimentally measured values of a_μ differ significantly from what is expected based on the theoretical calculations within the SM. The 4.2 σ deviation signifies a strong indication of physics beyond the SM. It suggests the presence of additional contributions to the magnetic moment of the muon that are not accounted for by the SM. The definition of a_μ is

$$a_\mu = \frac{g-2}{2} \tag{1.22}$$

where g is the g factor of the muon. The precise measurement of a_μ plays a crucial role in testing the validity of the SM and probing for physics beyond it. However, on the theoretical side, the lattice simulation result from the BMW collaboration [34] increases the leading hadronic contribution of $a_\mu^{\rm SM}$ with a relatively larger uncertainty. There are several new lattice results available now come from other collaborations [35, 36, 37, 38, 39, 40] seem to agree with the BMW result and would result in a discrepancy of about 3.3σ. The magnitude of the $3.3 - 4.2\sigma$ deviation in the measurement of the muon anomalous magnetic moment is substantial and warrants careful examination. Such a large deviation from the Standard Model prediction is highly intriguing and suggests the possibility of new physics beyond the Standard Model. It serves as a strong indication that there may exist additional particles, interactions, or phenomena that are yet to be accounted for in our current theoretical framework.

In conclusion, the search for lepton flavor universality violations continues to be an active area of research, both experimentally and theoretically. It offers an opportunity to probe the nature of particles and interactions at energies beyond those accessible by current experiments. By studying these violations, we aim to unravel the mysteries of the underlying physics and uncover new phenomena that may lie beyond the familiar territory of the Standard Model.

1.2.2.2 Lepton Flavor Violation

Lepton Flavor Violation refers to the transitions between different lepton sectors, and does not conserve the lepton family number. The evidence of LFV can be observed through neutrino oscillations, where neutrinos change between muon, electron, and tau neutrinos according to the Pontecorvo-Maki-Nakagawa-Sakata (PMNS) matrix. Experimental observations from various experiments such as Main injector neutrino oscillation search (MINOS) [41, 42, 43], KEK to Kamioka (K2K) [44, 45, 46], Super-Kamiokande Neutrino Detection Experiment (Super-K) [47, 48, 49], and Oscillation Project with Emulsion-tRacking Apparatus (OPERA) [50, 51, 52] have independently detected muon neutrino disappearance or the presence of tau neutrinos in muon neutrino beams over long baselines.

While LFV is observed for neutral leptons (neutrinos), the detection of Charged Lepton Flavor Violation (CLFV) would provide a direct signal of new physics [53, 54]. CLFV involves the violation of flavor and generation and has the potential to distinguish between different models and scenarios that explain the hints of Lepton Flavor Universality Violation in B meson decays. Currently, there is no experimental evidence for CLFV, but LFV decays are being actively searched for as they offer valuable opportunities to uncover new physics.

As discussed in Sec. 1.2.1, it is important to note that a violation of Lepton Flavor Universality does not necessarily imply a violation of Lepton Flavor. LFV is model-dependent, and therefore, we can distinguish between different theoretical frameworks and models that explain the observed deviations from LFU in various experimental measurements by investigating LFV phenomena. LFV processes serve as sensitive probes to test the validity of different new physics scenarios and can help to unveil the underlying physics principles governing the behavior of leptons.

Since the charged Lepton Flavor Violation is extremely suppressed in the Standard Model, $\ell_\alpha \to \ell_\beta < \mathcal{O}(10^{-54})$, while the current experimental limits of the Lepton Flavor Violation transitions are measured between $\mathcal{O}(10^{-8}) \sim \mathcal{O}(10^{-13})$, the pursuit of more stringent tests of Lepton Flavor Violation plays a vital role in narrowing down the potential candidates for new physics. Table 1.1 summarizes some current experimental constraints on the Lepton Flavor Violation transitions at 90% CL. These constraints are obtained from a variety of experiments conducted in different collaborations such as Mu to E Gamma (MEG), BaBar, Belle, and SINDRUM. By conducting precise measurements and imposing stricter constraints on LFV processes, we can effectively probe or set limits on the parameter space of new physics scenarios. This, in turn, enables us to identify the most viable candidates that can account for the observed LFV phenomena.

Table 1.1: Summary of experimental constraints on Lepton Flavor Violation (LFV) transitions at 90% CL.

LFV transitions	Current experimental bounds
BR($\mu \to e\gamma$)	4.2×10^{-13} [55]
BR($\tau \to e\gamma$)	3.3×10^{-8} [56]
BR($\tau \to \mu\gamma$)	4.2×10^{-8} [57]
BR($\mu \to eee$)	1.0×10^{-12} [58]
BR($\tau \to eee$)	2.7×10^{-8} [59]
BR($\tau \to \mu\mu\mu$)	2.1×10^{-8} [59]
BR($\tau \to e\eta$)	9.2×10^{-8} [60]
BR($\tau \to \mu\eta$)	6.5×10^{-8} [60]

Therefore, the investigation of LFV is crucial for advancing our knowledge of the fundamental nature of particles, their interactions, and the potential existence of new physics that extends beyond the current theoretical framework of the Standard Model.

1.2.3 Organization of the Rest Part of the Dissertation

In this dissertation, the focus is on exploring new physics beyond the Standard Model based on theoretical and experimental motivations. The previous section provided a comprehensive overview of the theoretical background and experimental evidence that justifies the need to investigate different BSM models. Building upon this foundation, the subsequent chapters of the dissertation delve into specific aspects of new physics models, experimental methods, data analysis, and the interpretation of results. By addressing the gaps and limitations of the SM, this research aims to contribute to our understanding of fundamental physics and provide insights into the nature of the underlying physical laws.

Chapter 2 presents the collaborative work [61] conducted with P. S. Bhupal Dev and Amarjit Soni. In Chapter 2, my focus lies on investigating two intriguing phenomena within the framework of R-parity violating Supersymmetry that suggest the violation of Lepton Flavor Universality. Firstly, we delve into the persistent indications of LFU violation observed in semileptonic decays of B-mesons, where experimental measurements deviate from the predictions of the Standard Model. These deviations provide valuable clues for the presence of new physics beyond the SM. Secondly, we address the well-known discrepancy between the SM prediction and experimental measurements of the muon anomalous magnetic moment, which also hints at LFU violation. To explore these phenomena, we employ the RPV SUSY framework, which offers theoretical solutions to reconcile the discrepancies between SM and the experiment. Through an extensive numerical scan of the parameter space, we have identified a remarkable characteristic in our scenarios: the orthogonality between the parameter space of the sbottom and the parameter space of the sneutrino. This feature underscores the distinct nature of our proposed scenarios and opens up new avenues for understanding LFU violations within RPV SUSY. Moreover, we present two novel signals that can serve as potential tests at the LHC, offering exciting opportunities for probing the sbottom and sneutrino parameter spaces in our scenarios. These signals have the potential to provide valuable experimental evidence and further illuminate the underlying physics responsible for the observed anomalies.

Chapter 3 presents the collaborative work [62] conducted with Yoav Afik, P. S. Bhupal Dev, and Amarjit Soni. In Chapter 3, we start from the insights gained from the work in Chapter 2, which highlighted the orthogonality between the sbottom and sneutrino parameter spaces, with the sbottom addressing B-physics anomalies and the sneutrino primarily addressing the muon $(g-2)$ anomaly. In this chapter, our focus is specifically on addressing the muon $(g-2)$ anomaly within the RPV SUSY framework. Building upon this framework, we propose an alternative solution to reconcile the observed discrepancy between theory and experiment in the muon $(g-2)$ measurement. Furthermore, we go beyond theoretical considerations and analyze distinctive signals that can be experimentally tested at the LHC. These signals serve as crucial probes to validate our proposed scenarios and provide experimental evidence supporting the presence of RPV SUSY as a solution to the muon $(g-2)$ anomaly.

Chapter 4 presents the collaborative work [63] conducted with P. S. Bhupal Dev and Amarjit Soni. Chapter 4 focuses specifically on the LLE interactions within the framework of R-Parity Violating Supersymmetry. We delve into various scenarios where different couplings, including both Lepton Flavor Violating (LFV) and Lepton Flavor Conserving (LFC), are non-zero. Through a systematic investigation of these cases, we provide a comprehensive analysis of the neutrino Non-Standard Interaction (NSI) parameters that can arise from the LLE interaction terms under different conditions. This analysis shows the relationship between LFV and NSI within the context of RPV SUSY, revealing intriguing connections and correlations between these phenomena.

Chapter 5 presents my work [64] on neutral and doubly-charged scalars. Chapter 5 takes inspiration from the Left-Right Symmetric Model and focuses on the phenomenology of leptophilic new scalars. Specifically, I explore the behavior and unique characteristics of electrically neutral and doubly-charged scalars in the context of future lepton colliders, such as the International Linear Collider (ILC) and the Compact Linear Collider (CLIC). My investigation considers both lepton flavor violating (LFV) and lepton flavor conserving

(LFC) couplings of these scalars. I define four distinct configurations that represent different combinations of four lepton flavors in the final states, ensuring a model-independent approach. I present the sensitivity of the ILC/CLIC experiments in the relevant mass/coupling parameter space. Additionally, I exploit various di-lepton invariant mass distributions to effectively distinguish signal events from background processes.

Chapter 6 serves as the conclusion of this dissertation, where we provide a comprehensive summary and discussion of the important role of Lepton Flavor Violation and Lepton Flavor Universality Violation in Beyond the Standard Model physics researches. Our findings demonstrate that LFV and LFUV provide valuable insights into the nature of new physics beyond the Standard Model and serve as powerful probes to test and validate different theoretical frameworks. The observed deviations from the SM predictions in experimental measurements strongly suggest the presence of new physics.

Chapter 2: Flavor Anomalies in R-Parity Violating Supersymmetry

This chapter is based on my work with P. S. Bhupal Dev and Amarjit Soni [61].

2.1 Introduction

A growing number of experimental data from various fields of physics, including flavor physics, neutrinos, and dark matter, show intriguing deviations from the predictions of the Standard Model (SM) at a significance level of a few standard deviations [65], indicating that we are entering a new age of anomalies. These anomalies have generated a great deal of attention and are the focus of extensive research in the scientific community.

While it is important to approach these anomalies with caution and carefully evaluate the possible sources of the deviations, including statistical fluctuations, systematic effects, theory/background uncertainties, and experimental errors, it is equally crucial to explore the possibility that some of these anomalies might be indicative of genuine new physics beyond the SM. This exploration is motivated by the idea that these deviations could provide valuable insights into the fundamental nature of the universe and potentially uncover new physics phenomena.

2.1.1 Semileptonic Decays of B-meson

Of the existing statistically significant ($\gtrsim 3\sigma$) anomalies in particle physics, one of the most intriguing and persistent deviations from the predictions of the Standard Model is the Lepton

Flavor Universality Violation (LFUV) observed in semileptonic decays of B-mesons. This phenomenon has been reported by multiple independent experiments, including BaBar [66], Belle [67, 68, 69, 70, 71], and LHCb [72, 73, 74, 75, 76], each with their own distinct datasets and analysis techniques. The combined significance of the LFUV measurements from these experiments is estimated to be approximately 4.5σ [77], indicating a strong deviation from the SM predictions. This discrepancy in lepton flavor universality is particularly striking because it implies a violation of the principle that the weak interactions treat all three generations of leptons (electron, muon, and tau) equally.

Furthermore, the LFUV observables observed in the context of semileptonic B-meson decays are often expressed in terms of the ratio of branching ratios (BRs) involving different flavors of charged leptons.

$$R_{D^{(*)}}^{\tau/\ell} = \frac{\mathrm{BR}(B \to D^{(*)}\tau\overline{\nu})}{\mathrm{BR}(B \to D^{(*)}\ell\overline{\nu})}, \tag{2.1}$$

with $\ell = e, \mu$ and

$$R_{K^{(*)}}^{\mu/e} = \frac{\mathrm{BR}(B \to K^{(*)}\mu^+\mu^-)}{\mathrm{BR}(B \to K^{(*)}e^+e^-)} \tag{2.2}$$

This choice of observables provides a convenient way to quantify the deviations from the Lepton Flavor Universality predicted by the Standard Model. The precise determination of these LFUV observables is a challenging task that requires accurate measurements of the decay rates and careful control of systematic uncertainties.

These LFUV observables have the advantage of being theoretically clean. This means that they are less susceptible to uncertainties arising from hadronic effects [1] and CKM (Cabibbo-

---

[1] The hadronic uncertainties refer to the uncertainties associated with the strong interactions between

Kobayashi-Maskawa) angle uncertainties [2]. Theoretical clean observables are particularly valuable because they are less influenced by higher-order quantum corrections [78, 79], making their predictions more reliable and precise. By virtue of their theoretical cleanliness, LFUV observables provide a more direct and reliable probe of lepton flavor universality violation. The reduced sensitivity to hadronic and CKM-angle uncertainties enhances the sensitivity to new physics effects, allowing for a clearer distinction between the SM predictions and potential signals of new physics.

In addition to the LFUV observables mentioned above, there are other intriguing aspects of the experimental data that warrant attention. A notable observation, as pointed out in Ref. [80], is the pattern seen in the charged-current B-decays: $B \to D^{(*)}\ell\nu$ and $B_c \to J/\psi\, \ell\nu$ (with $\ell = e, \mu, \tau$), Remarkably, all of the 11 different measurements performed to date for these decays consistently exhibit central values that are above the central value predicted by the Standard Model. This collective deviation from the SM prediction in charged-current B-decays is an intriguing phenomenon. The observed pattern suggests the possibility of new physics contributions affecting these decay processes. The fact that all measurements consistently show higher central values than expected raises the question of whether there is a common underlying mechanism at play.

Furthermore, the measurements of R_K [76] and R_{K^*} [74] by the LHCb collaboration provide additional evidence for physics beyond the Standard Model. These observables, however, consistently exhibit values below the unity predicted by the SM. The deviations of R_K and R_{K^*} from their SM predictions offer valuable information for distinguishing between different beyond the SM scenarios. One intriguing aspect is that certain BSM models incorporating right-handed currents can predict an anti-correlation between R_K and R_{K^*}.

---

quarks within the B-mesons. These interactions can affect the decay rates and introduce uncertainties in the calculations.

[2] Similarly, the CKM-angle uncertainties, which arise from the parameterization of the CKM matrix elements, also have a reduced impact on LFUV observables. The CKM matrix describes the mixing of quark flavors and plays a crucial role in flavor-changing processes.

This correlation provides a unique signature that can help identify or constrain specific classes of new physics models.

Additionally, it is noteworthy that the more recent update of the R_K measurement by LHCb, which utilized a larger dataset [76], did not significantly change the central value compared to the previous measurement. The central value remains at 0.846, with a precision of up to three decimal places [75]. This stability in the central value indicates that the observed deviation from the SM prediction may not be a statistical fluctuation or a result of limited data, but rather a persistent discrepancy that calls for further investigation. Looking ahead, the prospects for clarifying the status of the B-anomalies appear promising. The LHCb experiment and the Belle-II experiment are expected to accumulate even more data in the near future. The increased statistics from these experiments will provide additional precision and help to further constrain the measurements of R_K and other related observables.

As a result, the statistically significant LFUV anomalies found in semileptonic B-meson decays cast doubt on the SM's predictions and offer tantalizing hints of new physics that lies beyond the scope of our existing knowledge. The nature of these anomalies, their relationships to other reported deviations, and the fundamental physics governing the behavior of leptons and their interactions are the subjects of ongoing theoretical and experimental research.

2.1.2 Muon Anomalous Magnetic Moment

Another intriguing anomaly that suggests LFUV is the long-standing discrepancy between the predictions of the SM and the experimental measurements of the muon anomalous magnetic moment $(g-2)_\mu$ [81]. This discrepancy has recently witnessed an important development with the release of the first result from the Fermilab $(g-2)$ experiment[82], which is found to be consistent with the previous measurement from the BNL experiment [83] up to six significant figures.

Combining the results from Fermilab and BNL and comparing them with the world-average prediction from the SM [84], the significance of the $(g-2)_\mu$ anomaly is increased to 4.2σ [82]. This level of significance indicates that the deviation between the experimental measurement and the SM prediction is unlikely to be a statistical fluctuation and may indeed be a genuine indication of new physics. The compatibility between the Fermilab and BNL results provides additional confidence in the presence of the $(g-2)_\mu$ anomaly and motivates further investigations into its origin.

Indeed, obtaining an accurate theoretical prediction for the muon anomalous magnetic moment $(g-2)_\mu$ within the Standard Model is a challenging task. Over the years, significant progress has been made in developing systematic and data-driven strategies to calculate this quantity. One widely used approach is the R-ratio method [85, 86, 87, 88, 89], which is based on dispersion relations [90, 91, 92] and provides a systematic framework for improving the theoretical prediction. Another completely independent and non-perturbative lattice simulation method that has been used to compute $(g-2)_\mu$ has significantly matured over the years [93, 94, 95, 96, 97, 98, 99, 34]; see Ref. [84] for a review. Indeed, the recent lattice QCD result from the BMW collaboration [34] has provided a competitive calculation of the muon anomalous magnetic moment $(g-2)_\mu$ within the Standard Model (SM). This result claims compatibility between their calculation and the experimental measurement at a level of 1.5σ. However, it is important to note that this result is based on a particular fermion discretization method known as "staggered fermions". Interestingly, there is a significant discrepancy between the BMW lattice result and the R-ratio method results, which are based on dispersion relations and utilize experimental data. The disagreement between the BMW result and the R-ratio results is estimated to be around 3.7σ [100, 34]. And the disagreement is also in $\approx 2.5\sigma$ tension [100] with another lattice/data ("window method") result of RBC-UKQCD collaboration [95] using domain-wall fermions [101, 102, 103, 104]. Because domain-wall fermions act like continuum-like fermions and the domain-wall approach essentially preserves the chiral symmetry of the continuum theory at any lattice spacing, the associated chiral perturbation theory is remarkably similar to the continuum theory [105]. Contrary to staggered fermions, which entail numerous unphysical degrees of freedom that only decouple in the continuum limit, extrapolating to the continuum limit requires a somewhat laborious study of staggered chiral perturbation theory [106, 107, 108]. Another issue with the BMW result, for example, is that other issues with global electroweak fit may arise if a modification in the hadronic vacuum polarization contribution, as claimed by the BMW collaboration, pushes the SM value of $(g-2)_\mu$ closer to the experimental value [109, 110, 111, 112] (Refer to the rebuttal provided in Ref. [34] for further details and counterarguments). There is a widely held and long-standing consensus within the lattice community that significant physics results should be treated with due seriousness only when there is consistency and agreement among various fermion discretization methods in the continuum limit.

2.1.3 Flavor Anomalies

Considering the current state of these three flavor anomalies, namely $R_{D^{(*)}}$, $R_{K^{(*)}}$, and $(g-2)_\mu$, it is evident that they collectively present compelling evidence for the presence of flavor-nonuniversal physics beyond the Standard Model. The combined significance of these anomalies exceeds 5σ [80]. With the forthcoming updates from Belle-II, LHCb, and Fermilab experiments, there is heightened anticipation that the anomalies observed will withstand further scrutiny. If these anomalies persist, it would signify a significant departure from the expectations set by the Standard Model. This would suggest that nature is actively addressing long-standing and persistent issues that have remained unresolved within the framework of the SM. One fundamental issue with the Standard Model is its remarkable degree of fine-tuning, often referred to as unnaturalness. This arises from the radiative instability of the Higgs boson, which is primarily driven by the substantial mass of the top quark belonging to the third generation. The LFUV observable $R_{D^{(*)}}$, which involves the decay process $b \to c\tau\nu$, is particularly intriguing as it includes interactions between at least two fermions from the third generation. Motivated by experimental hints of LFUV and the issue of radiative stability in the SM, researchers have explored alternative theoretical frameworks to explain these anomalies. One such proposal is a particular minimal R-parity-violating supersymmetry framework [113], known as "RPV3". In this framework, the superpartners of the third-generation particles are predicted to be lighter compared to those of the first two generations. This choice is driven by the desire for minimality and addressing the specific LFUV anomaly observed in the $R_{D^{(*)}}$ measurements. The RPV3 scenario provides a compelling and theoretically well-motivated solution within the framework of supersymmetry. In a subsequent study [80], it is found that $R_{K^{(*)}}$ and $(g-2)_\mu$ can also be addressed within the RPV3 framework. The specific parameter setup of Case 3 presented in Ref. [80], which explains the observed flavor anomalies, is actually problematic when considering LFV decays such as $\mu \to e\gamma$ and $B_s \to e\mu$. By carefully selecting specific values for the relevant parameters, it is possible to achieve a consistent explanation for these three independent anomalies.

In this chapter, we undertake an extensive investigation of the minimal RPV3 parameter space, aiming to provide a comprehensive analysis of its capability to simultaneously explain the observed flavor anomalies. We take into account the most recent updates from experimental measurements and carefully consider all relevant collider and flavor constraints. By exploring various regions of the parameter space, we aim to identify the parameter sets that can successfully address the anomalies while satisfying the experimental bounds from a wide range of observables. The RPV3 framework is subject to a multitude of experimental constraints arising from various decay processes and mixing phenomena involving particles such as Z, W, τ, D^0, B, B_s, and B_c. These constraints impose significant restrictions on the allowed parameter space of RPV3, rendering it a rather constrained framework. However, the RPV3 framework still remains highly predictive and testable.

We also proposed specific collider signatures that can serve as independent probes of the preferred regions within the RPV3 parameter space. These signatures are motivated by general crossing symmetry arguments and offer unique opportunities to explore the RPV3 framework at the energy frontier. By investigating these collider signatures, we aim to complement the information obtained from intensity frontier observables and further constrain the RPV3 framework. The complementarity between the collider signatures and low energy constraints enhances the predictive power of the RPV3 framework and enables more stringent tests of its validity. With ongoing and upcoming collider experiments, we anticipate that these proposed collider signatures will play a crucial role in probing and validating the preferred RPV3 region. Note also that there exists significant motivation and rationale for this theoretical scenario from an entirely different perspective [114]. Moreover, the presence of heavy first two generations in the renormalization group (RG) evolution effects plays a significant role in achieving the observed 125 GeV Higgs mass. This feature renders the model less fine-tuned compared to the constrained Minimal Supersymmetric SM (cMSSM) [115, 116]. While the RPV3 framework offers several appealing features, it is important to acknowledge two significant caveats associated with this model. These caveats will be briefly discussed later in this chapter.

2.2 R-Parity Violating Supersymmetry

One intriguing possibility in the realm of BSM physics is the introduction of R-parity violating supersymmetry (RPV SUSY). R-parity is a hypothetical symmetry that assigns a quantum number of +1 to SM particles and -1 to their supersymmetric partners. R-parity conservation is a key assumption in supersymmetry, ensuring the stability of the lightest supersymmetric particle (LSP), often considered a candidate for dark matter. However, in RPV SUSY,

R-parity conservation is relaxed, allowing for interactions that violate lepton number (L) and baryon number (B). The inclusion of R-parity violation in SUSY introduces new terms in the superpotential and/or the soft SUSY breaking terms [117]. These new terms can lead to a variety of interesting and phenomenologically rich phenomena. In particular, RPV SUSY can give rise to new decay modes for the sparticles (supersymmetric particles).

In this analysis, we restrict our focus to the trilinear R-Parity Violating superpotential terms within the framework of the Minimal Supersymmetric Standard Model (MSSM).

$$W_{\text{RPV}} = \frac{1}{2}\lambda_{ijk}L_iL_jE^c_k + \lambda'_{ijk}L_iQ_jD^c_k + \frac{1}{2}\lambda''_{ijk}U^c_iD^c_jD^c_k, \tag{2.3}$$

where L_i and Q_i denote the $SU(2)_L$ doublet, E^c_i, U^c_i, and D^c_i correspond to the $SU(2)_L$ singlet chiral superfields with $i, j, k = 1, 2, 3$ represent the generation indices. In Eq. (2.3), the λs are the couplings of LLE-type interactions, the λ's are the couplings of LQD-type interactions, and the λ''s are the couplings of UDD-type interactions. It is worth noting that the $SU(2)_L$ and $SU(3)_c$ gauge invariance in the RPV superpotential leads to the requirement of antisymmetry in the coupling parameters λ_{ijk} and λ''_{ijk} with respect to their i, j or j, k indices respectively.

In the context of studying Lepton Flavor Universality Violation, our focus is specifically on the terms in the superpotential that involve leptons. Therefore, we narrow our attention to the LLE and LQD parts, as these terms are directly relevant to our investigation of LFUV and its potential implications in the framework we are considering. Furthermore, it is important to note that in the presence of both λ and λ' couplings, constraints from proton decay need to be considered. However, these constraints can be satisfied as long as the relevant λ'' (UDD-type) couplings are sufficiently suppressed [117]. This suppression can be achieved by implementing a baryon triality mechanism [118, 119]. By ensuring the appropriate suppression of these couplings, we maintain consistency with experimental limits on proton decay while still allowing for the presence of both λ and λ' interactions in our framework.

The effective number of relevant degrees of freedom in the RPV3 framework for the three LFUV observables is higher, about the order of $\mathcal{O}(36)$, compared to the $\mathcal{O}(15)$ degrees of freedom in the Standard Model (SM). This naturally raises the question: What benefits do we gain by doubling the number of degrees of freedom? The answer lies in the deeper Bose-Fermi symmetry rationale and the numerous attractive features that come automatically with supersymmetry. These features include the radiative stability of the Higgs boson, the generation of neutrino masses through radiative processes, electroweak symmetry breaking through radiative effects, the stability of the electroweak vacuum, the potential for gauge coupling unification, the possibility of (gravitino) dark matter, and the potential for baryogenesis [117]. Furthermore, as an essential extension of the Yang-Mills theory [2], it is imperative to incorporate all interactions permitted by the expanded internal symmetry of the theory. This inclusiveness inherently eliminates the coincidental flavor symmetry present in the Standard Model and naturally gives rise to the phenomenon of LFUV.

RPV3 framework exhibits additional noteworthy characteristics that align with experimental observations. For instance, it naturally predicts values of R_K and R_{K^*} that are less than one, consistent with the measured values. Furthermore, the polarizations of D^* mesons and tau leptons in RPV3 are essentially identical to those predicted by the Standard Model, as RPV3 encompasses the chiral gauge couplings of the SM. These features emerge automatically within the RPV3 framework, further supporting its viability in explaining the observed phenomena.

It is noteworthy that the semileptonic B-meson decays under consideration involve interactions of a bottom quark, which belongs to the third generation of quarks, in terms of $b \to c\ell^-\overline{\nu}$ or $b \to s\ell^+\ell^-$ transitions. However, semileptonic decays of charmed mesons such as $D \to X\ell^+\nu$ ($X = \pi, K, \omega, \eta, \rho$) [120, 121, 122, 123, 124] that involve the transition of $c \to d\ell^+\nu$, the ratio of the rates of leptonic kaon decays $K^\pm \to e^\pm\nu$ and $K^\pm \to \mu^\pm\nu$ [125, 126], Λ-baryon decays $\Lambda \to pe^-\overline{\nu}$ and $\Lambda \to p\mu^-\overline{\nu}$ [127] all completely concur with the Standard Model. Hence, it is plausible to consider that the third-generation fermions possess distinctive characteristics within the framework of the Standard Model. Similarly, in the context of RPV3, we can adopt the notion of specialness for the third-generation sfermions, aligning with the concept of the "natural SUSY" hypothesis.

The $R_{D^{(*)}}$ anomaly can be explained within the RPV3 framework through the tree-level contributions arising from the LQD interactions [113, 128, 129, 130, 131, 132, 133, 134]:

$$\begin{aligned}\mathcal{L}_{LQD} &= \lambda'_{ijk}[\tilde{\nu}_{iL}\overline{d}_{kR}d_{jL} + \tilde{d}_{jL}\overline{d}_{kR}\nu_{iL} + \tilde{d}^*_{kR}\overline{\nu}^c_{iL}d_{jL} \\ &\qquad - \tilde{e}_{iL}\overline{d}_{kR}u_{jL} - \tilde{u}_{jL}\overline{d}_{kR}e_{iL} - \tilde{d}^*_{kR}\overline{e}^c_{iL}u_{jL}] + \text{H.c.}\end{aligned} \tag{2.4}$$

Similarly, the $R_{K^{(*)}}$ anomaly can be addressed by considering the contributions from both tree and loop-level LQD interactions, either independently or in combination with LLE interactions [135, 130, 136, 137, 131, 133, 138, 139]:

$$\mathcal{L}_{LLE} = \frac{1}{2}\lambda_{ijk}[\tilde{\nu}_{iL}\overline{e}_{kR}e_{jL} + \tilde{e}_{jL}\overline{e}_{kR}\nu_{iL} + \tilde{e}^*_{kR}\overline{\nu}^c_{iL}e_{jL} - (i \leftrightarrow j)] + \text{H.c.} \tag{2.5}$$

The muon $g-2$ receives additional contributions from both LQD and LLE terms [140]. However, in our parameter space of interest, we will find that the contribution from LLE interactions is more significant.

Out of the $3^3 = 27$ independent RPV couplings λ'_{ijk} in Eq. (2.4) and the $3^2 = 9$ independent λ_{ijk} (because the λ couplings are antisymmetric in the first two indices, i.e. $\lambda_{ijk} =$

$-\lambda_{jik}$) in Eq. (2.5), we focus our attention on the RPV couplings involving third-generation sfermions within our RPV3 framework, specifically consider the 19 independent λ'_{ijk} couplings in Eq. (2.4) and the 7 independent λ_{ijk} in Eq. (2.5). Subsequently, based on the parameter space, we proceed to calculate the contributions of RPV3 to the flavor anomalies.

2.2.1 R_D and R_{D^*}

The $b \to c\ell\nu$ transition relevant for the $R_{D^{(*)}}$ anomaly receives a contribution from beyond the Standard Model (BSM) at tree level through the LQD interactions, specifically via the exchange of the right-handed sbottom ($\tilde{b}_R$), as depicted in Figure 2.1. It gives rise to an effective Hamiltonian that resembles the one in the Standard Model

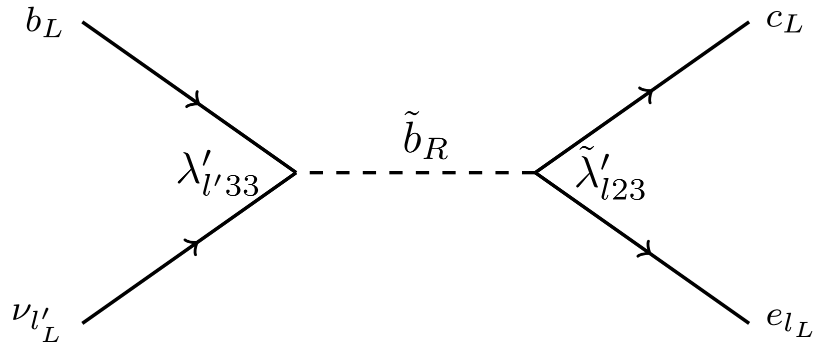

Figure 2.1: RPV3 contribution to $R_{D^{(*)}}$ via sbottom exchange involving λ' couplings. Here $\widetilde{\lambda'}_{ijk}$ is defined as $\lambda'_{ilk}V_{jl}$ (with V_{jl} being the CKM matrix elements).

$$\mathcal{H}_{\text{eff}}^{b\to c\ell\nu} = \frac{4G_F}{\sqrt{2}}V_{cb}\left(1 + C_{V_L}\right)\mathcal{O}_{V_L} + \text{H.c.}, \tag{2.6}$$

where G_F is the Fermi constant and V_{cb} is the (2,3) CKM element with the operator $\mathcal{O}_{V_L} = (\bar{c}_L\gamma^\mu b_L)(\bar{\ell}_L\gamma_\mu\nu_{\ell L})$ with a corresponding coefficient $C_{V_L} \simeq 0.09$, as preferred by the q^2 and D^* polarization data [141]. We can then derive the following expression [131]

$$\begin{aligned}\frac{R_D}{R_D^{\rm SM}} &= \frac{R_{D^*}}{R_{D^*}^{\rm SM}} = \frac{|\Delta^c_{31}|^2 + |\Delta^c_{32}|^2 + |1+\Delta^c_{33}|^2}{|\Delta^c_{21}|^2 + |1+\Delta^c_{22}|^2 + |\Delta^c_{23}|^2}\ , \qquad (2.7)\\ \text{with } \Delta^c_{ll'} &= \frac{v^2}{4m^2_{\tilde b_R}}\lambda'_{l'33}\left(\lambda'_{l33} + \lambda'_{l23}\frac{V_{cs}}{V_{cb}} + \lambda'_{l13}\frac{V_{cd}}{V_{cb}}\right)\ ,\end{aligned}$$

with $v = (\sqrt{2}G_F)^{-1/2}$ denoting the electroweak scale. The $R_{D^{(*)}}$ anomaly can be explained by the value of the ratio in Eq. (2.7) being 1.15 ± 0.04 [80], which determines the allowed parameter space in the $(m_{\tilde b_R}, \lambda'_{lk3})$ plane that is consistent with the observed values of $R_{D^{(*)}}$.

From Eq. (2.4), for the LQD interactions in RPV3, we can see that the dimension-six effective interaction for the semileptonic $B \to D^{(*)}$ decays is virtually the same as the $(V-A)\times(V-A)$ structure of the SM effective Hamiltonian (after the appropriate Fierz transformation) with a difference that only affects the overall coefficient. Therefore, the fact that the experimentally observed q^2 distribution and the D^* and τ polarizations prefer the $\mathcal{O}_{V_L}$ operator [141] conforms to our RPV3 scenario.

There is yet another contribution to $R_{D^{(*)}}$ from RPV3 with left-handed stau exchange in the presence of LLE interactions [80]. Although right-handed bottom and charged lepton are involved, the appropriate effective operator $\mathcal{O}_{V_R}$ does not offer the best match to the observables for $b \to c\ell\nu$ [141]. Therefore, to ensure that the stau channel is irrelevant, we select the coupling $\lambda'_{323} = 0$. In a similar vein there are extra contributions involving $B \to D^{(*)}\ell\tilde\chi$ for a light neutralino $\tilde\chi$, but they end up being sub-dominant [80].

It is worth highlighting that in the MSSM with two Higgs doublets, a conventional R-parity conserving (RPC) contribution to $b \to c\ell\nu$ exists, arising from charged Higgs exchange. However, this contribution exhibits the opposite behavior and is significantly smaller in the case of R_{D^*} [13, 142]. Furthermore, it is important to note that this scenario is in tension with LHC mono-τ data [143], and it leads to a significant BR$(B_c \to \tau\nu) > 50\%$ which poses challenges [144, 145, 146] (although there are alternative interpretations, as discussed in

Ref. [147]). Hence, within a supersymmetric (SUSY) framework, one needs to consider the RPV interactions mentioned above in order to explain the anomalies observed in $b \to c\ell\nu$ transitions.

2.2.2 R_K and R_{K^*}

Simultaneous contributions of RPV interactions to both electron and muon final states in the $b \to s\ell^+\ell^-$ transitions, addressing the $R_{K^{(*)}}$ anomaly, would face strong constraints from lepton flavor violating (LFV) searches such as $\mu \to e\gamma$. Therefore, in light of recent global fits [148], we focus solely on corrections to the muonic channel, as it is favored by the data. The effective Hamiltonian relevant to this analysis is given by

$$\mathcal{H}_{\text{eff}}^{b\to s\ell\ell} = -\frac{4G_F}{\sqrt{2}} V_{ts}^* V_{tb} \frac{e^2}{16\pi^2} \sum_{i=9,10} [C_i^\ell Q_i^\ell + C_i'^\ell Q_i'^\ell] \tag{2.8}$$

with the operators $Q_9^\ell = (\bar{s}\gamma_\alpha P_L b)(\bar{\ell}\gamma^\alpha \ell)$, $Q_{10}^\ell = (\bar{s}\gamma_\alpha P_L b)(\bar{\ell}\gamma^\alpha\gamma_5 \ell)$, and $Q'_{9,10}$ are obtained from $Q_{9,10}$ by replacing $P_L \to P_R$. Global fits of all relevant data, including angular observables, absolute rates for $B \to K^{(*)}\mu^+\mu^-$, and the rate for $B_s \to \phi\mu^+\mu^-$, indicate a preference for the Wilson coefficients $C_9^\mu = -C_{10}^\mu = -0.35 \pm 0.08$ [148]. On the other hand, the Wilson coefficients $C_9'^\mu$ and $C_{10}'^\mu$ are found to be compatible with zero at a 2σ level.

In the RPV3 scenario, both tree-level and loop-level contributions arise for $b \to s\ell\ell$ transitions. The tree-level exchange of stops introduces contributions to the wrong chirality of Wilson coefficients,

$$C_9'^\mu \ = \ -C_{10}'^\mu = -\frac{v^2}{2m_{\tilde{t}_L}^2} \frac{\pi}{\alpha_{\text{em}}} \frac{\lambda'_{233}\lambda'_{232}}{V_{tb}V_{ts}^*}\ , \tag{2.9}$$

where α_{em} is the fine structure constant. This can be approximated as an upper bound at the 3σ confidence level (CL) on

$$|\lambda'_{233}\lambda'_{232}| \lesssim 10^{-3} \times \left(\frac{m_{\tilde{t}_L}}{1\,\text{TeV}}\right)^2 . \tag{2.10}$$

This condition can be fulfilled by either increasing the mass of the stop or by choosing a small value for one of the λ'_{23k} couplings (with $k = 2$ or 3).

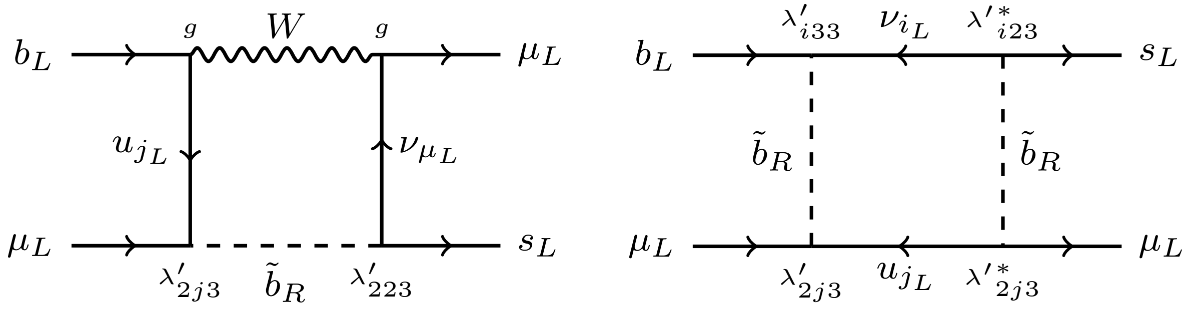

Figure 2.2: Representative box diagrams for the dominant RPV3 contributions to $b \to s\mu^+\mu^-$ in our scenario.

At the one-loop level, there are additional contributions to the $b \to s\ell\ell$ process involving sbottoms, stops, staus, and sneutrinos in the loop [136, 137, 131, 80]. For the minimal RPV3 scenario under consideration, the only relevant diagrams are those shown in Fig. 2.2. After accounting for all possible combinations of box diagrams, the resulting Wilson coefficients are determined as follows:

$$C_9^\mu = -C_{10}^\mu = \frac{m_t^2}{m_{\tilde{b}_R}^2}\frac{|\lambda'_{233}|^2}{16\pi\alpha_{\text{em}}} - \frac{v^2}{m_{\tilde{b}_R}^2}\frac{X_{bs}X_{\mu\mu}}{64\pi\alpha_{\text{em}}V_{tb}V_{ts}^*}, \tag{2.11}$$

where $X_{bs} = \sum_{i=1}^3 \lambda'_{i33}\lambda'_{i23}$ and $X_{\mu\mu} = \sum_{j=1}^3 |\lambda'_{2j3}|^2$. By demanding that Eq. (2.11) is consistent with the global-fit outcome, we establish the parameter space allowed by the $R_{K^{(*)}}$ anomaly in the $(m_{\tilde{b}_R}, \lambda'_{lk3})$ plane. It is worth noting that the correlation between R_K and $R_{K^{(*)}}$, where both exhibit the same trend, naturally emerges within the RPV3 framework due to the shared gauge structure with the Standard Model.

It is crucial to emphasize that within the MSSM framework with only R-parity conserving (RPC) couplings, the generation of lepton-flavor non-universal contributions to $b \to s\ell\ell$ transitions necessitates the involvement of box diagrams with light winos (or binos) and significant non-universality in slepton masses [149, 150]. Nevertheless, achieving the required value of $C_9^\mu \sim -0.35$ within this framework necessitates an extremely light spectrum of winos and smuons at around 100 GeV, as well as sbottoms with masses around 500 GeV. However, such light particle masses are strongly disfavored by the available LHC data [151]. Therefore, similar to the explanation of the $R_{D^{(*)}}$ anomaly, addressing the $R_{K^{(*)}}$ anomaly within the framework of supersymmetry requires the inclusion of RPV interactions.

2.2.3 Muon $(g-2)$

The RPV3 framework can provide contributions to the muon anomalous magnetic moment $(g-2)_\mu$ through both the λ and λ' couplings [140], as illustrated in Fig. 2.3.

$$\Delta a_\mu = \frac{m_\mu^2}{96\pi^2} \sum_{k=1}^{3} \left(\frac{2(|\lambda_{32k}|^2 + |\lambda_{3k2}|^2)}{m_{\tilde{\nu}_\tau}^2} - \frac{|\lambda_{3k2}|^2}{m_{\tilde{\tau}_L}^2} - \frac{|\lambda_{k23}|^2}{m_{\tilde{\tau}_R}^2} + \frac{3|\lambda'_{2k3}|^2}{m_{\tilde{b}_R}^2} \right) , \tag{2.12}$$

which is used to compare with the observed discrepancy of $\Delta a_\mu^{\rm obs} = (251 \pm 59) \times 10^{-11}$ [82].

It is worth noting that the contributions from staus to $(g-2)_\mu$ have the wrong sign and should be sub-dominant by having relatively heavier staus. In our RPV3 scenario, we will see that the dominant contribution to $(g-2)_\mu$ comes from sneutrinos through the λ coupling, while the contribution from sbottoms through the λ' coupling is less significant. There are other diagrams, as shown in Ref. [80], which are not relevant to our discussion. It is interesting to note that the diagrams involving stop mediators cancel each other out, leading to their absence in Fig. 2.3. Additionally, the diagram featuring a right-handed stau mediator does not contribute in this scenario, as one of the corresponding couplings is assumed to be zero.

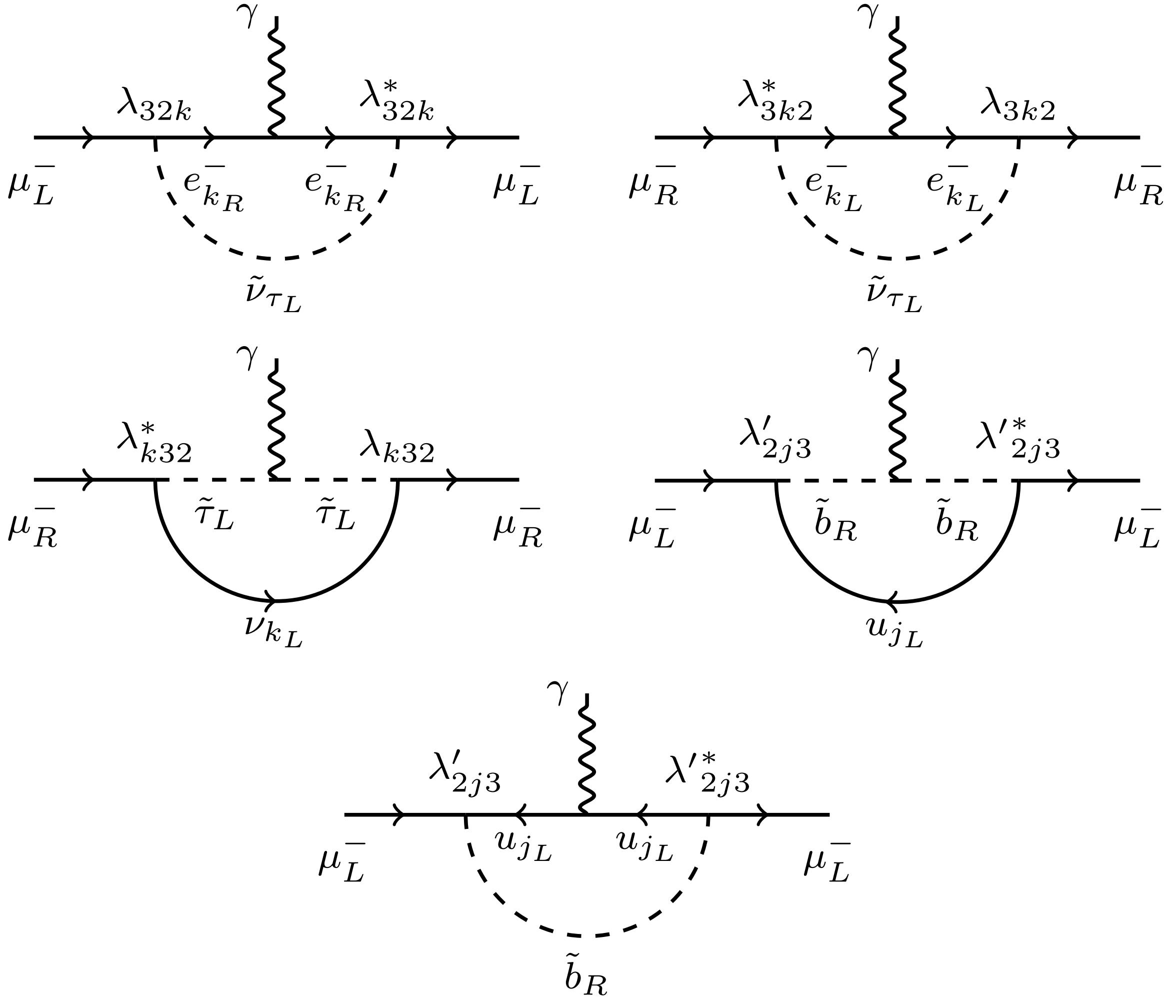

Figure 2.3: Relevant contribution to the $(g-2)_\mu$ from λ and λ' couplings in our RPV3 scenario.

While there are additional contributions to Δa_μ from RPC SUSY involving smuons and muon sneutrinos [152, 153, 154], these contributions are decoupled from the low-energy theory in RPV3 due to the decoupling of second-generation sfermions. Therefore, we focus solely on the RPV contributions to Δa_μ in our analysis.

2.3 Numerical Scan

Our objective is to identify the minimal set of RPV3 model parameters that can simultaneously explain all three flavor anomalies while remaining consistent with other low-energy flavor constraints and the high-energy LHC data. Additionally, we aim to identify potential collider signals that can serve as an independent test of the observed anomalies. For a more detailed discussion and explicit expressions of the low energy constraints, please refer to Appendix A and Ref. [80]. To achieve our objective, we focus on a 6-dimensional parameter space that turns out to be the most important for pursuing collider implications:

$$\{\lambda_{232}, \lambda'_{233}, \lambda'_{223}, \lambda'_{232}, m_{\tilde{b}_R}, m_{\tilde{\nu}_\tau}\} \tag{2.13}$$

Furthermore, unless explicitly stated otherwise, we omit any mention or consideration of the remaining couplings and masses in our analysis. Due to the specific behavior of renormalization group (RG) evolution, where the RG evolution of any RPV coupling is proportional to the coupling itself (up to the two-loop level) [155], it is noteworthy that couplings set to zero at the initial scale will remain zero at all scales throughout the RG flow.

Regarding the selection of our couplings, it is important to highlight that when choosing a non-zero value for λ_{232} (which is equal to $-\lambda_{322}$) to account for the $(g-2)_\mu$ anomaly [cf. Eq. (2.12)], other λ_{3ij} couplings must not be large simultaneously. This is necessary to satisfy the constraints imposed by lepton flavor-violating decays such as $\tau^- \to \mu^+\mu^-\mu^-$ and $\mu \to e\gamma$. Likewise, it is important to note that only certain λ'_{2ij} couplings are permitted to be large concurrently with λ_{232}. In contrast, selecting λ'_{3ij} in combination with λ_{232} and a light tau-sneutrino propagator would result in significant tree-level decays of mesons $\overline{d}_i d_j \to \mu^+\mu^-$. It is important to highlight that the chosen of couplings $\lambda'_{3ij} = 0$ preclude the single production of tau-sneutrinos at the LHC. Consequently, our discussion in the main text focuses solely on their pair production.

Regarding the omission of the remaining third-generation sfermion masses from Eq. (2.13), it is worth noting that the right-stau mass $m_{\tilde{\tau}_R}$ is irrelevant. It only affects the expression for $(g-2)_\mu$ in Eq.(2.12), where it is associated with the coupling λ_{k23}, which we have set to zero in our benchmark points. The left-stau term in Eq. (2.12) has a negative contribution and its effect can be ignored for $m_{\tilde{\tau}_L} \gtrsim \mathcal{O}(2\ \text{TeV})$. For the sake of concreteness, we will fix the left-stau mass to be $m_{\tilde{\tau}_L} = 4$ TeV in the subsequent analysis. Similarly, the left-stop mass $m_{\tilde{t}_L}$ only has influence on the C_9' and C_{10}' [cf. Eq. (2.10)] and the constraint from $B_s \to \mu^+\mu^-$, if both λ'_{233} and λ'_{232} are large at the same time. In this situation, we can make $m_{\tilde{t}_L}$ appropriately heavier using Eq. (2.10) without affecting any other observables. Therefore, we exclude the parameter $m_{\tilde{t}_L}$ from Eq. (2.13). Finally, the left-sbottom mass $m_{\tilde{b}_L}$ does not influence the anomaly observables, but is only relevant for constraints like $b \to s\gamma$, $B \to K\nu\overline{\nu}$ and B_s-$\overline{B}_s$. In this chapter, for simplicity, we will assume $m_{\tilde{b}_L} = m_{\tilde{b}_R}$ whenever applicable.

We proceed by conducting a random scan over the 6-dimensional parameter space defined in Eq. (2.13), considering the following ranges:

$$\begin{aligned}
&|\lambda_{232}| \in [2.5,\ 3.5],\ |\lambda'_{233}| \in [0.01,\ 3],\\
&|\lambda'_{223}| \in [0.01,\ 3],\ |\lambda'_{232}| \in [0.01,\ 3],\\
&m_{\tilde{b}_R} \in [1.2,\ 10]\ \text{TeV},\ m_{\tilde{\nu}_\tau} \in [0.7,\ 1.2]\ \text{TeV},
\end{aligned} \tag{2.14}$$

We subsequently search for solutions that can successfully account for the $R_{D^{(*)}}$, $R_{K^{(*)}}$, and $(g-2)_\mu$ anomalies, with a focus on those that fall within the 2σ or 3σ range. Additionally, we ensure that these solutions remain consistent with all the aforementioned low-energy constraints. Out of the 30 million points that were scanned, only 1570 solutions were identified. This can be observed in the scatter plots presented in Figure 2.4. It should be noted that the lower edges of the scan ranges for $m_{\tilde{\nu}_\tau}$ and $m_{\tilde{b}_R}$ are determined by the current limits set by the LHC, as discussed in Section 2.5.

The obtained solutions are divided into three distinct regions, represented by the red, blue, and yellow points in the Fig. 2.4. In particular, from Fig. 2.4(c), we see that the yellow (blue) points correspond to $|\lambda'_{232}| < 0.2$ and $|\lambda'_{223}| < (>)1$, while the red points correspond to $|\lambda'_{232}| > 0.2$ and $1.5 < \lambda'_{223}/\lambda'_{232} < 5.5$, and the green points simply correspond to the crossover region from red to blue. Several observations can be made from these plots, as follows:

(i) From Figs. 2.4(b,c), we see that there are both yellow and blue solutions with very small (or almost vanishing) λ'_{232} which means that for these points, we can automatically satisfy the $C'_9 - C'_{10}$ constraint discussed in main text, as well as the $B_s \to \mu^+\mu^-$ constraint for any value of the stop mass.

(ii) From Fig. 2.4(c), we see that the red points cluster around $\lambda'_{223}/\lambda'_{232} \sim 3$; this helps to avoid the $B_s - \overline{B}_s$ constraint due to an accidental cancellation.

(iii) From Figs. 2.4(a,b,c), we find that λ'_{233} and λ'_{223} must have opposite signs. This is mainly needed to make the second term of Eq. (2.11) negative in order to satisfy the $R_{K^{(*)}}$ anomaly. Similarly, λ'_{223} and λ'_{232} are preferred to have the same sign to get cancellation in $B_s - \overline{B}_s$ mixing. On the other hand, as Eq. (2.12) suggests and as shown in Fig. 2.4(i), the sign of λ_{232} does not matter.

(iv) According to Fig. 2.4(i), the different colored points are totally mixed, which implies mutual orthogonality between the $(m_{\tilde{\nu}_\tau}, \lambda)$ and $(m_{\tilde{b}_R}, \lambda')$ parameter spaces. In other words, $(m_{\tilde{\nu}_\tau}, \lambda)$ mostly influences the $(g-2)_\mu$ solutions, whereas $(m_{\tilde{b}_R}, \lambda')$ influences the $R_{D^{(*)}}$ and $R_{K^{(*)}}$ solutions and the low-energy flavor constraints. This is further illustrated in Figs. 2.5 and 2.6.

(v) From Fig. 2.4(e), we find that $|\lambda'_{223}| \lesssim 0.57\,(m_{\tilde{b}_R}/1\text{ TeV})$, which is mainly due to the

$D^0 \to \mu^+\mu^-$ constraint. Similarly, from Fig. 2.4(d), we get $|\lambda'_{233}| \lesssim 1.0\,(m_{\tilde{b}_R}/1\text{ TeV})$. These two conditions imply that the λ' contributions to $(g-2)_\mu$ in Eq. (2.12) cannot be large; therefore, the bulk of the RPV3 contribution must come from the λ sector, which requires relatively larger $\lambda_{232} \gtrsim 2.8$ and smaller $m_{\tilde{\nu}_\tau} \lesssim 0.9$ TeV (to keep λ_{232} perturbative) to satisfy the $(g-2)_\mu$ anomaly, as confirmed in Fig. 2.4(i).

(vi) From Fig. 2.4(g), we find that $\sqrt{-\lambda'_{223}\lambda'_{233}} \sim (0.20-0.28)\,(m_{\tilde{b}_R}/1\text{ TeV})$, which mainly comes from the $B \to K\nu\overline{\nu}$ constraint.

(vii) From Fig. 2.4(a), we find that for the yellow and blue points, $|\lambda'_{233}\lambda'_{223}|$ is small to satisfy the $B_s - \overline{B}_s$ mixing constraint.

(viii) From Fig. 2.4(f), we see that $|\lambda'_{232}| \lesssim 1.5$. Thus, according to Fig. 2.4(c), $|\lambda'_{232}|$ should be either small (yellow and blue) or $\sim |\lambda'_{223}|/3$ (red). Also, from Fig. 2.4(d), $|\lambda'_{233}| \gtrsim 0.20$ and from Fig. 2.4(e), $|\lambda'_{223}| \gtrsim 0.12$.

(ix) Figs. 2.4(d,e,f) suggest that $m_{\tilde{b}_R} \gtrsim 1.44$ TeV, slightly stronger than the direct LHC bound of 1.23 TeV [156].

(x) Fig. 2.4(h) gives the range of $X_{bs}X_{\mu\mu}$ for the RPV3 contribution to $R_{K^{(*)}}$, since the second term in Eq. (2.11) gives the correct sign, whereas the first term gives the wrong sign.

2.4 Benchmark Points

We will choose our benchmark points for the collider study in the next section based on the results of our numerical scan in Fig. 2.4 and the above-mentioned observations. Specifically, we choose three benchmark points (BP1, BP2, BP3), one each from the red (BP1), yellow (BP2) and blue (BP3) solutions found above.

- BP1 (Red): $\lambda'_{233} = -\lambda'_{223} = -3\lambda'_{232}$. The allowed region in this case is shown in Fig. 2.5 (a) by the red shaded region.

- BP2 (Yellow): $\lambda'_{233} = -8\lambda'_{223}$, $\lambda'_{232} = 0$. The allowed region in this case is shown in Fig. 2.5 (b) by the yellow shaded region.
- BP3 (Blue): $\lambda'_{223} = -6\lambda'_{233}$, $\lambda'_{232} = 0$. The allowed region in this case is shown in Fig. 2.5 (c) by the blue shaded region.

The size of the allowed region in each case is directly correlated with the density of the corresponding points in Fig. 2.4. Therefore, our BP1 is taken from the densest region of the red solution, in order to maximize the overlap region in Fig. 2.5. For BP2 and BP3, we just choose $\lambda'_{232} = 0$ for simplicity. Since the λ coupling and the tau-sneutrino mass are relevant only for $(g-2)_\mu$, we fix $\lambda_{232} = -\lambda_{322} = 2.8$ and $m_{\tilde{\nu}_\tau} = 0.7$ TeV (see Fig. 2.6) in all three cases to explain the $(g-2)_\mu$ anomaly at 3σ (2σ) CL, as shown by the orange shaded regions with solid (dashed) boundaries in Fig. 2.5.

Fig. 2.5 shows the three RPV3 benchmark cases in the $(m_{\tilde{b}_R}, \lambda'_{233})$ parameter space explaining the flavor anomalies. The cyan, pink, and orange shaded regions with solid (dashed) boundaries explain the $R_{D^{(*)}}$, $R_{K^{(*)}}$ and $(g-2)_\mu$ anomalies at 3σ (2σ) respectively. The black-shaded region is excluded by the current LHC search for sbottoms in the bottom+neutralino channel, whereas the dark green-shaded region is the LHC exclusion derived from a $\mu^+\mu^- + 1b$ search. The horizontal dotted line shows the perturbativity limit of $\sqrt{4\pi}$. Other shaded regions show the relevant low-energy flavor constraints on the parameter space from $B \to K\nu\overline{\nu}$ (brown), $B_s - \overline{B}_s$ mixing (magenta), $D^0 \to \mu^+\mu^-$ (purple), $b \to s\gamma$ (grey) and $Z \to \ell^+\ell^-$ (violet). The allowed overlap regions simultaneously explaining the $R_{D^{(*)}}$, $R_{K^{(*)}}$ and $(g-2)_\mu$ anomalies are shown by the red (top), yellow (bottom left) and blue (bottom right) shaded regions for the three benchmark cases. The $*$ mark on the top panel gives representative values of $m_{\tilde{b}_R}$ and λ'_{233} in the BP1 scenario that are used in Fig. 2.6. The green solid, dashed, and dot-dashed contours respectively show the 2σ sensitivities of the 14 TeV LHC, 27 TeV, and 100 TeV pp colliders in the $\bar{t}\mu^+\mu^-$ channel discussed previously.

In BP1, since both λ'_{233} and λ'_{232} are nonzero, there is a lower limit on the stop mass from the $C'_9 - C'_{10}$ constraint [cf. Eq. (2.10)] : $m_{\tilde{t}_L} \gtrsim (14-40)$ TeV for the overlap region. According to Ref. [157], stop masses lower than about 10 TeV are preferred from naturalness point of view. For a quantitative measure, the level of fine-tuning must be less than some fixed amount, taken there to be the arbitrary threshold of 10%. However, this limit does not apply for BP2 and BP3, since $\lambda'_{232} = 0$ in those cases; therefore, the stop can be as light as the current LHC bound of ~ 800 GeV [151] in these cases. We have also checked that the constraints from $B_s \to \mu^+\mu^-$, whose amplitude is proportional to $C^{\mu}_{10} - C'^{\mu}_{10}$ [158], is easily satisfied for all three BPs, with the RPV3 contribution to $\mathrm{BR}(B_s \to \mu^+\mu^-) \lesssim 10^{-12}$, well below the current experimental precision: $\mathrm{BR}(B_s \to \mu^+\mu^-)_{\rm exp} = \left(2.69^{+0.37}_{-0.35}\right) \times 10^{-9}$ [159].

We should also comment on the $B_s - \overline{B}_s$ mixing constraint. For our benchmark points, the last term in Eq. (A.2) does not contribute, as both λ'_{332} and λ'_{323} are set to zero. As discussed before, a non-zero λ'_{3ij} combined with λ_{232} and light tau-sneutrino propagator will lead to strong tree-level meson decays $\overline{d}_i d_j \to \mu^+\mu^-$. The excellent agreement between the experimental measurement [159] and SM prediction [160] of $\mathrm{BR}(B^0_s \to \mu^+\mu^-)$ requires an almost zero last term in Eq. (A.2). For BP1 with $\lambda'_{223}/\lambda'_{232} = 3 \simeq -P^{LR}_1/P^{VLL}_1$, there is a cancellation (at the level of 5%) between the other two terms in Eq. (A.2), thus enabling us to explain $R_{K^{(*)}}$ within 1σ, while this is not the case in BP2 and BP3 where $R_{K^{(*)}}$ can only be explained at 3σ level. Note that one can always assume a non-zero λ'_{232} for BP2 and BP3 (corresponding to the yellow and blue points out of the vertical axis in Figs. 2.4(b,c)) to make $B_s - \overline{B}_s$ mixing constraint weaker and enlarge the allowed parameter space for $R_{K^{(*)}}$, but this makes the $B \to K\nu\overline{\nu}$ constraint stronger, which limits the allowed region in BP2.

Our fit results for the best-case scenario are shown in Figs. 2.5 and 2.6 for the mutually orthogonal parameter spaces of $(m_{\tilde{b}_R}, \lambda')$ and $(m_{\tilde{\nu}_\tau}, \lambda)$ respectively. In Fig. 2.5, the cyan, pink, and orange-shaded regions with solid (dashed) boundaries explain the $R_{D^{(*)}}$, $R_{K^{(*)}}$, and $(g-2)_\mu$ anomalies respectively at 3σ (2σ) CL. The black-shaded region is the 13 TeV LHC exclusion derived from a sbottom search in the bottom+neutralino channel [156]. The dark-green-shaded region is the 13 TeV LHC exclusion derived from a $\mu^+\mu^- + 1b$ search [161] that is also applicable to our RPV3 scenario; see Sec. 2.5. The horizontal dashed line shows the perturbativity limit of $\sqrt{4\pi}$. Other shaded regions in Fig. 2.5 show the relevant low-energy flavor constrains on the $(m_{\tilde{b}_R}, \lambda'_{233})$ parameter space from $B \to K\nu\overline{\nu}$ (brown), $B_s - \overline{B}_s$ mixing (magenta), $D^0 \to \mu^+\mu^-$ (purple), $b \to s\gamma$ (grey) and $Z \to \ell^+\ell^-$ (violet); see Appendix A for more details.

Now turning to the $(m_{\tilde{\nu}_\tau}, \lambda_{232})$ parameter space, the $(g-2)_\mu$-preferred region at 3σ (2σ) is shown by the solid (dashed) orange contours in Fig. 2.6. We have fixed the other RPV3 parameters using a benchmark point from the allowed region in Fig. 2.5 as shown by the $*$ mark. The purple-shaded region is excluded by recasting the results of a recent 13 TeV LHC multi-lepton search [162], whereas the green curve is the 14 TeV HL-LHC sensitivity; see Sec. 2.5. The horizontal black dashed line shows the perturbativity limit of $\sqrt{4\pi}$ as before. Because of the orthogonality between the $(m_{\tilde{b}_R}, \lambda')$ and $(m_{\tilde{\nu}_\tau}, \lambda)$ parameter spaces, the position of the $*$ in Fig. 2.6 will not change much for BP2 and BP3; therefore, we do not include the corresponding figures for BP2 and BP3.

Since the required λ-couplings are fairly large in our scenario, we also show the Landau pole positions by the horizontal gray dashed lines, which are obtained by numerically solving the relevant one-loop RG equations (RGEs) [155]. Because the non-zero λ' couplings in our scenario do not couple to the third-generation slepton or sneutrino, the RGE for the λ_{232} coupling (and similarly, for the λ_{322} coupling) is very simple at one-loop level:

$$\frac{\mathrm{d}}{\mathrm{d}t}\lambda_{232} \simeq \frac{\lambda_{232}}{16\pi^2}\left(4\lambda_{232}^2 - \frac{9}{5}g_1^2 - 3g_2^2\right) \approx \frac{1}{4\pi^2}\lambda_{232}^3\,, \tag{2.15}$$

where g_1 and g_2 are the $U(1)_Y$ and $SU(2)_L$ gauge couplings, respectively, both of which are much smaller than the λ_{232} coupling in the parameter space shown in Fig. 2.6. We find that the benchmark point shown in Fig. 2.6 hits the Landau pole at 12.4 TeV.

One possible way out of the Landau pole issue is to consider a non-zero λ_{233} coupling instead of λ_{232}. This does not affect the $R_{D^{(*)}}$ and $R_{K^{(*)}}$ fit results presented in Fig. 2.5 because of the orthogonality between the λ' and λ parameter space mentioned before. As for the $(g-2)_\mu$-preferred region in the $(m_{\tilde{\nu}_\tau}, \lambda_{233})$ parameter space, the main difference with respect to Fig. 2.6 is that the allowed λ couplings can now be as low as 0.8, thus pushing the Landau pole to as high as 2.5×10^{16} GeV. The reason is that the relevant LHC constraint for λ_{233} comes from $\mu^+\mu^-\tau^+\tau^-$ final state (in contrast with the $\mu^+\mu^-\mu^+\mu^-$ final state in Fig. 2.6). We did not find any 13 TeV LHC analysis in this channel, and using the old 8 TeV analysis from Ref. [163], we obtain a lower bound of only 150 GeV on the sneutrino mass. A dedicated 13 TeV analysis to update this bound is currently underway.

2.5 Collider Signals

Simple crossing symmetry arguments have been used to establish high-p_T model-independent tests of the $R_{D^{(*)}}$ and $R_{K^{(*)}}$ anomalies in the CMS and ATLAS experiments [113, 164, 165, 166, 143, 167, 80]. The basic idea is that the underlying quark-level processes $b \to c\tau\nu$ for $R_{D^{(*)}}$ and $b \to s\ell^+\ell^-$ for $R_{K^{(*)}}$ necessarily imply, by crossing symmetry, the existence of processes like $pp \to \tau\nu$, $pp \to \ell^+\ell^-$, $pp \to b\tau\nu$ and $pp \to b\ell^+\ell^-$, which can be searched for in the high-p_T LHC experiments. In fact, a recent CMS study has found a mild discrepancy in the ratio of differential $\mu^+\mu^-$ to e^+e^- pair-production cross sections [168], which might turn out to be important for the $R_{K^{(*)}}$ anomaly. However, the model-independent effective field theory treatments relating the low-energy operators to the high-p_T LHC signals might break down, if the new physics cut-off scale is smaller than the LHC energies. Thus, it is important to explore all possible high-p_T LHC signals in the context of a given BSM scenario in order to distinguish it from other BSM interpretations of the flavor anomalies.

To this effect, we propose some striking LHC signals that could be used as an independent probe of the allowed RPV3 parameter space shown in Figs. 2.5 and 2.6 at the high-p_T LHC and future colliders. For the $(m_{\tilde{b}_R}, \lambda')$ parameter space in Fig. 2.5, we propose the process $pp \to \bar{t}(t)\mu^+\mu^-$ mediated by an sbottom; see Fig. 2.7. There is no $pp \to \bar{t}(t)\mu^+\mu^-$ final state in the SM, so the dominant SM background comes from $pp \to \bar{t}(t)\mu^+\mu^- X$ where X can be either a light jet (j), b-jet, or a gauge boson decaying to jets or leptons, which are somehow missed in the detector. We perform a parton-level simulation for the signal and background processes using MadGraph5_aMC@NLO v2.7.0 [169]. We assume that the (anti)top quark can be identified from its decay products and use the minimal trigger cuts $p_T^{t,\mu} > 20$ GeV, $|\eta^{t,\mu}| < 2.5$, $\Delta R^{\mu\mu} > 0.4$ and $\Delta R^{t\mu} > 0.4$ for the $t(\bar{t})\mu^+\mu^- X$ final states. To estimate the SM background, we further require that the X containing jets, leptons, or missing transverse energy is soft enough to evade detection, i.e. $p_T^{j,b,\ell} < 20$ GeV and $E_T^{\text{miss}} < 20$ GeV.

For the RPV3 signal, we use the three benchmark points discussed in the previous section. It is easy to see that the $pp \to t\mu^+\mu^-$ and $pp \to \bar{t}\mu^+\mu^-$ give similar cross-sections for the signal, because in all three cases, $\lambda'_{k13} = 0$, and therefore, the first-generation quarks do not participate in the initial state. For our parameter choice, the main contribution comes from $\bar{c}(c)g$ initial states as shown in Fig. 2.7. Since the $\bar{c}$ and c contents in proton are very similar, the resulting cross-section should also be the same. However, for the SM background, $t\mu^+\mu^- X$ final state has two times more background than $\bar{t}\mu^+\mu^- X$, which mainly comes from the fact that the u content in proton is much larger than the $\bar{u}$ content. Therefore, we will only consider the $pp \to \bar{t}\mu^+\mu^-$ final state to show our sensitivity contours.

With the basic trigger cuts, we find that the total SM background for the $pp \to \bar{t}\mu^+\mu^-(+X)$ final state at $\sqrt{s} = 14$ TeV is 0.4 fb, which is dominated by $X = j$. For comparison, the corresponding signal cross section for the $*$ point in BP1 in Fig. 2.5 is only

1.5×10^{-3} fb. However, we can improve the signal-to-background substantially by using their different kinematic features. First of all, the $\mu^+\mu^-$ in the SM background case mainly comes from Z decay, so we expect the dimuon invariant mass $M_{\mu^+\mu^-}$ to peak at the Z-mass and to drop significantly at higher masses; see Fig. 2.8 (green). On the other hand, in our RPV3 case, one of the muons in the final state comes from sbottom decay, so we expect a longer tail in the $M_{\mu^+\mu^-}$ distribution, as confirmed in Fig. 2.8 (red). Therefore, using an appropriate cut on $M_{\mu^+\mu^-} > 400$ GeV, we can maximize the signal-to-background ratio. We find that the corresponding signal at the $*$ point in BP1 and background cross sections after the $M_{\mu^+\mu^-}$ cut are respectively 1.1×10^{-3} fb and 4.2×10^{-4} fb. Further improvements in the signal-to-background can in principle be achieved using the fact that for an on-shell sbottom decaying to $\bar{t}\mu^+$, we expect a peak at the sbottom mass in the invariant mass $M_{\bar{t}\mu^+}$ distribution for the signal, but not for the background. However, since the final-state reconstruction involving top quarks is somewhat involved, especially for the leptonic decay of the W boson coming from the top, and also the sbottom mass is not known a priori (we use it as a free parameter in Fig. 2.5), we refrain from using the $M_{\bar{t}\mu^+}$ cut in our analysis.

Assuming an integrated luminosity of $\mathcal{L} = 3000$ fb^{-1}, we show the 2σ signal significance in Fig. 2.5 by the green solid, dashed and dot-dashed contours for $\sqrt{s} = 14$, 27 and 100 TeV colliders, respectively. We find that a portion of the overlap region explaining all flavor anomalies can already be accessed at the HL-LHC, while the proposed future colliders should be able to access the entire allowed parameter space.

Now for the $(m_{\tilde{\nu}_\tau}, \lambda)$ parameter space in Fig. 2.6 relevant only for the $(g-2)_\mu$ anomaly, we focus on the spectacular four-muon final state [170] coming from the sneutrino pair-production, followed by each sneutrino decaying into two muons via the λ_{232} coupling; see Fig. 2.9. Such multilepton channels are very clean even at the hadron colliders, and in fact, the results of a recent ATLAS multilepton analysis [162] can already be recast into a new bound on the sneutrino mass. Using the 95% CL observed cross section limit of 0.044 fb for the 4ℓ, off-Z signal region with $M_{4\mu} > 400$ GeV[3] and the same selection criteria as in Ref. [162], we obtain a lower bound of $m_{\tilde{\nu}_\tau} \gtrsim 670$ GeV, as shown by the purple-shaded region in Fig. 2.6. This LHC constraint already rules out a big chunk of the $(g-2)_\mu$-preferred region and pushes the λ_{232} coupling toward the perturbativity limit. The HL-LHC can completely cover the remaining $(g-2)_\mu$-preferred region, as shown by the green curve in Fig. 2.6.

2.6 Discussion

In this section, we make a few remarks on our results before concluding our discussion.

2.6.1 Interplay Between Anomalies

We find in Fig. 2.6 that only a narrow region in the $(m_{\tilde{\nu}}, \lambda_{232})$ parameter space is allowed that could explain the $(g-2)_\mu$ anomaly in our minimal RPV3 setup. It is worth checking how does the $(g-2)_\mu$-preferred region gets affected on its own, and more importantly, if dropping the $R_{D^{(*)}}$ and $R_{K^{(*)}}$ anomalies could open up more parameter space in Fig. 2 2.6. To this effect, we find that allowing $\lambda'_{213} \neq 0$ in Eq. (2.12), the $(g-2)_\mu$ solution can be improved only slightly, compared to Fig. 2.6. With $m_{\tilde{b}_R} = 1.23$ TeV (the minimum value allowed by LHC 13 TeV data) and $|\lambda'_{233}| = 1.57$ (the maximum value allowed from the Z-decay universality constraint g_A^μ / g_A^e, where g_A^ℓ is the axial-vector coupling of Z to leptons), the lower 3σ bound of $(g-2)_\mu$ starts at $(0.7\ \text{TeV}, 2.66)$ and ends at $(0.93\ \text{TeV}, \sqrt{4\pi})$ in the $(m_{\tilde{\nu}_\tau}, \lambda_{232})$ parameter space. The lower 2σ bound is still not reached for $\lambda_{232} < \sqrt{4\pi}$. Because of the constraints $B \to K\nu\bar{\nu}$ and $K \to \pi\nu\bar{\nu}$, $\lambda'_{213}, \lambda'_{223} \approx 0$ and thus cannot contribute much to the $(g-2)_\mu$ anomaly in this optimal $(g-2)_\mu$ case.

Nevertheless, it is important to mention that due to the orthogonality between $(m_{\tilde{\nu}_\tau}, \lambda)$

---

[3] This also removes potential contributions from heavy neutral Higgs to ZZ final states.

and $(m_{\tilde{b}_R}, \lambda')$ parameter spaces in our RPV3 scenario, even if the four-muon signal completely rules out the $(g-2)_\mu$-favored region in Fig. 2.6 (drawn for BP1, but similar for BP2 and BP3 as we can see from Fig. 2.4(i)), the $R_{D^{(*)}}$ and $R_{K^{(*)}}$ anomalies can still be explained by the $(m_{\tilde{b}_R}, \lambda')$ parameter space shown in Fig. 2.5. Similarly, suppose the $pp \to \bar{t}\mu^+\mu^-$ signal completely rules out one of the overlap regions in Fig. 2.5, but it will not affect the $(g-2)_\mu$ solution in Fig. 2.6.

2.6.2 Leptoquark Versus RPV3

Several BSM scenarios have been invoked to explain the flavor anomalies, but very few have the ability to explain all the flavor anomalies simultaneously in a minimal, theoretically well-motivated setup like the RPV3. Leptoquarks (LQs) have been a popular choice, but a single scalar LQ solution has now been disfavored by global fits [171]. A single vector LQ $U_1(\mathbf{3}, \mathbf{1}, 2/3)$ still remains a viable option [172, 173, 174], but must be embedded in some ultraviolet completion like the Pati-Salam gauge group [175, 176, 177], thus necessarily requiring more particles to cancel gauge anomalies, and hence, losing its minimality feature. Another alternative is to invoke more than one scalar LQs [178, 179, 180, 181, 182, 183]. The right-sbottom with λ' couplings in our RPV3 scenario behaves exactly like the $SU(2)_L$-singlet LQ $S_1(\mathbf{3}, \mathbf{1}, -1/3)$ originally invoked in Ref. [184], which still gives an excellent fit to the $b \to c\tau\nu$ data, including polarization observables and forward-backward asymmetry [185]. However, the same S_1 LQ cannot explain the $b \to s\mu^+\mu^-$ data simultaneously [186], while being consistent with the low-energy constraints, in particular from $B_s - \overline{B}_s$ mixing. This is a key difference with RPV3, where a TeV-scale sbottom by itself can explain both $R_{D^{(*)}}$ and $R_{K^{(*)}}$, owing to a (partial) cancellation in the $B_s - \overline{B}_s$ mixing [cf. Eq. (A.2)]. Another important difference is the λ coupling, which gives rise to the distinct four-lepton signal in the RPV3 scenario and uniquely distinguishes our scenario from LQ models.

2.6.3 Precision Tests

Apart from the collider tests proposed here, our RPV3 solution to the flavor anomalies can also be probed via low-energy precision observables at LHCb and Belle-II. For instance, the $*$ benchmark point in Fig. 2.5 predicts the ratio [cf. Eq. (A.1)] $R_{B\to K\nu\overline{\nu}} = 2.1$, which is just below the Belle 95% CL upper limit of 3.2 [187, 188]. The future Belle-II sensitivity can improve this limit by up to a factor of 5 [189], which should be able to completely probe the overlap region. In particular, the red, yellow, and blue overlap regions in Fig. 2.5 can be completely excluded for $R_{B\to K\nu\overline{\nu}} < 1.7$, 2.0 and 1.1 respectively. This is a distinct feature of our RPV3 scenario.[4] Similarly, future lattice improvements in the precision of the SM prediction for $B_s - \overline{B}_s$ mixing could be fateful for the overlap region in Fig. 2.5. In addition, hints of LFUV in other independent observables involving the third generation, such as LFV τ and B decays, $b \to c\mu\nu/b \to ce\nu$ and baryonic decay modes like $\Lambda_b \to \Lambda\ell^+\ell^-$, would provide critical further tests of our proposal. Furthermore, there are other lepton flavor violating B and τ decays that could get enhanced contributions from RPV3 within reach of Belle II sensitivity [80]. If the flavor anomalies persist and grow in statistical significance, the precision flavor observables mentioned above, in conjunction with the collider observables discussed in Sec. 2.5, might be able to uniquely distinguish our RPV3 interpretation from other BSM interpretations.

2.6.4 Caveats

In spite of all the above-mentioned attractive features of our RPV3 scenario, there are a few weak points that we just lay out here for future contemplation.

- **L**andau Pole: In the minimal RPV3 setup presented here, some of the λ' and λ couplings are required to be fairly large $\gtrsim \mathcal{O}(1)$. Such large couplings would hit the Landau pole

---

[4] For instance, in the U_1 vector LQ case, there is no tree-level contribution to $B \to K\nu\overline{\nu}$ and any prediction involving loop-processes depends on the UV-completion details.

very quickly, preventing the model from being valid all the way up to the gauge coupling unification scale. For instance, the benchmark point shown in Fig. 2.6 hits the Landau pole at 12.4 TeV. There might be a way out in the general RPV-MSSM with more parameters, but a detailed analysis of the full MSSM parameter space is beyond the scope of this work.

- **N**eutrino Mass: The trilinear RPV couplings in Eqs. (2.4) and (2.5) contribute to neutrino masses at one-loop level through the lepton-slepton and quark-squark loops [190, 191, 117]. To ensure that the neutrino masses remain small and satisfy the cosmological bound on the sum $\sum_i m_{\nu_i} \lesssim 0.1$ eV [192], we require some degree of cancellation between the soft trilinear A-terms and the $\mu \tan\beta$ term [80], depending on the other SUSY parameters.
- **D**ark Matter: In RPV scenarios, the lightest supersymmetric particle (LSP) is no longer stable, but decays to SM particles. Therefore, it cannot be the dark matter of the Universe, unless it is sufficiently long-lived, which requires extremely small values of the RPV couplings. In our RPV3 scenario with $\mathcal{O}(1)$ RPV couplings, the neutralino LSP cannot be the dark matter. However, a gravitino LSP with its naturally Planck-suppressed decays can in principle have a lifetime much longer than the age of the universe, and hence, be the dark matter [193].
- **H**ierarchy of RPV Couplings: For our numerical analysis, we have treated the relevant RPV couplings as free parameters and find the best-fit that explains the flavor anomalies. We find that some of the RPV couplings need to be fairly large $\gtrsim \mathcal{O}(1)$, while some others need to be hierarchically smaller, and yet others need to be extremely small or vanishing. One could in principle invoke a flavor symmetry (similar to Ref. [131] for instance) to explain such hierarchy between couplings; so this need not be an insurmountable issue, although it would require further work.

2.7 Conclusion

The recent results from the Fermilab muon $g-2$ experiment, as well as the persisting hints of lepton flavor universality violation in B-meson decays, present a very strong case for flavor-nonuniversal new physics beyond the Standard Model. We asserted that a minimal R-parity violating supersymmetric scenario with relatively light third-generation sfermions (dubbed as 'RPV3') provides a natural, well-motivated framework for the simultaneous explanation of all flavor anomalies while being consistent with a multitude of low-energy flavor constraints, as well as with limits from high-energy collider searches. We further propose complementary tests and distinct signatures of this scenario in the high-p_T searches at current and future colliders. Specifically, we find that a sbottom in the mass range of 2–12 TeV accounts for $R_{D^{(*)}}$ and $R_{K^{(*)}}$ flavor anomalies and it only plays a minor role in the $(g-2)_\mu$ anomaly, whereas a sneutrino with a mass between 0.7–1 TeV is the dominant player for $(g-2)_\mu$. In this context, we propose specific collider signatures of sbottom via its decays to $\bar{t}(t)\mu^+\mu^-$, and of sneutrino pairs with their decays leading to a highly distinctive and spectacular four-muon final state, which can be used to completely probe the RPV3 parameter space of interest.

The flavor anomalies might already be giving us the first glimpse of natural supersymmetry with light third-generation sfermions and with R-parity violating couplings. We have proposed a simple, testable RPV3 scenario that simultaneously explains the $R_{D^{(*)}}$, $R_{K^{(*)}}$ and $(g-2)_\mu$ anomalies with TeV-scale sbottom and tau sneutrino which are easily accessible at the HL-LHC. With experimental updates from LHCb, Belle-II, and Fermilab muon $(g-2)$ experiments in the next few years, as well as with better limits on third-generation sfermion masses from the LHC, our knowledge of the anomalies will surely evolve, and the allowed RPV3 ranges shown in Figs. 2.5 and 2.6 may have to be modified accordingly. But let us hope SUSY prevails in the end.

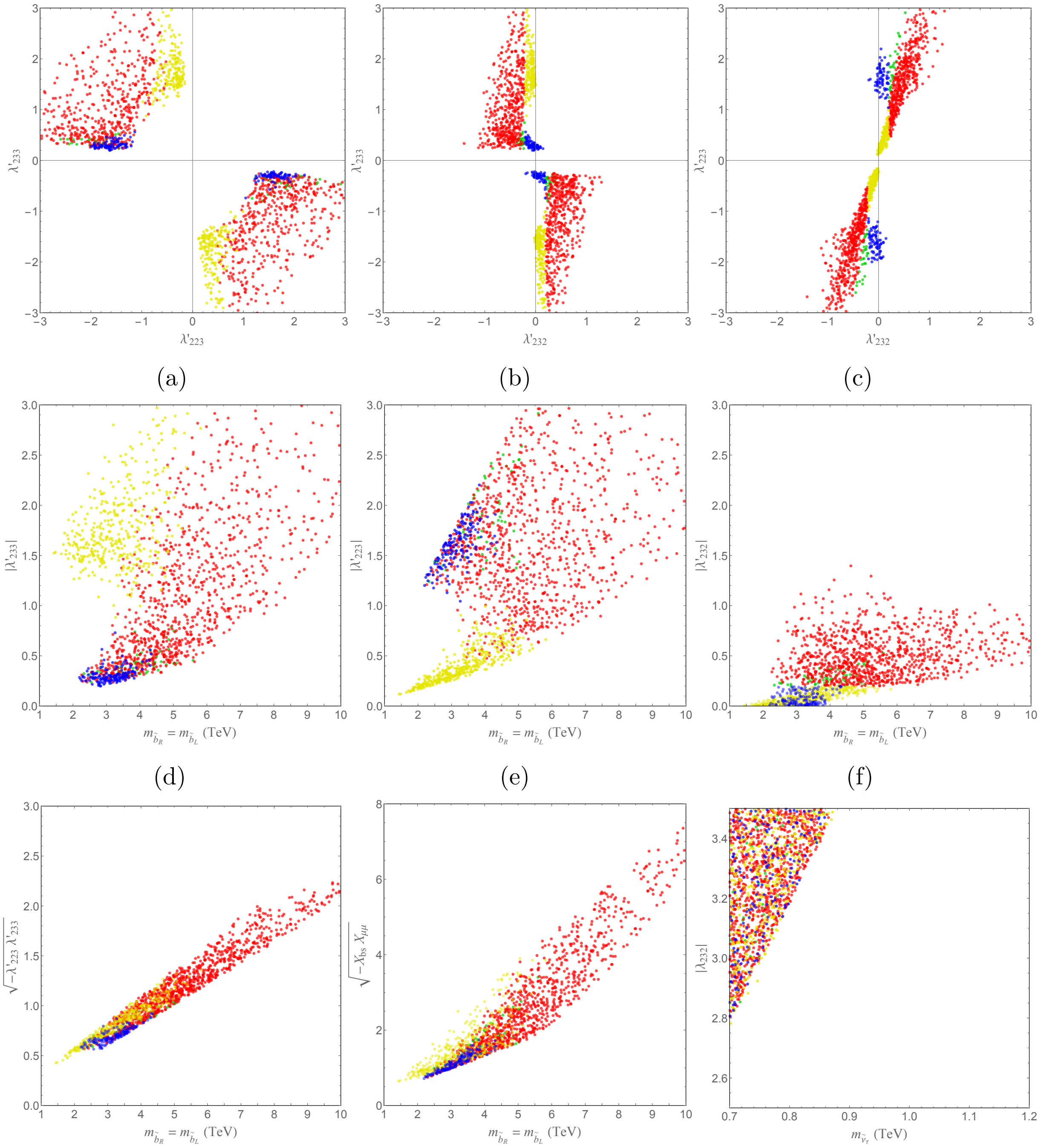

(a) (b) (c)

(d) (e) (f)

(g) (h) (i)

Figure 2.4: Scatter plots showing the correlations between various RPV3 parameters in Eq. (2.13). All these points can simultaneously explain $R_{D^{(*)}}$, $R_{K^{(*)}}$ and $(g-2)_\mu$ anomalies at 3σ CL, while being consistent with all the low-energy and LHC constraints. The yellow (blue) points correspond to $|\lambda'_{232}| < 0.2$ and $|\lambda'_{223}| < (>)1$. The red points correspond to $|\lambda'_{232}| > 0.2$ and $1.5 < \lambda'_{223}/\lambda'_{232} < 5.5$. The green points correspond to the crossover region from red to blue.

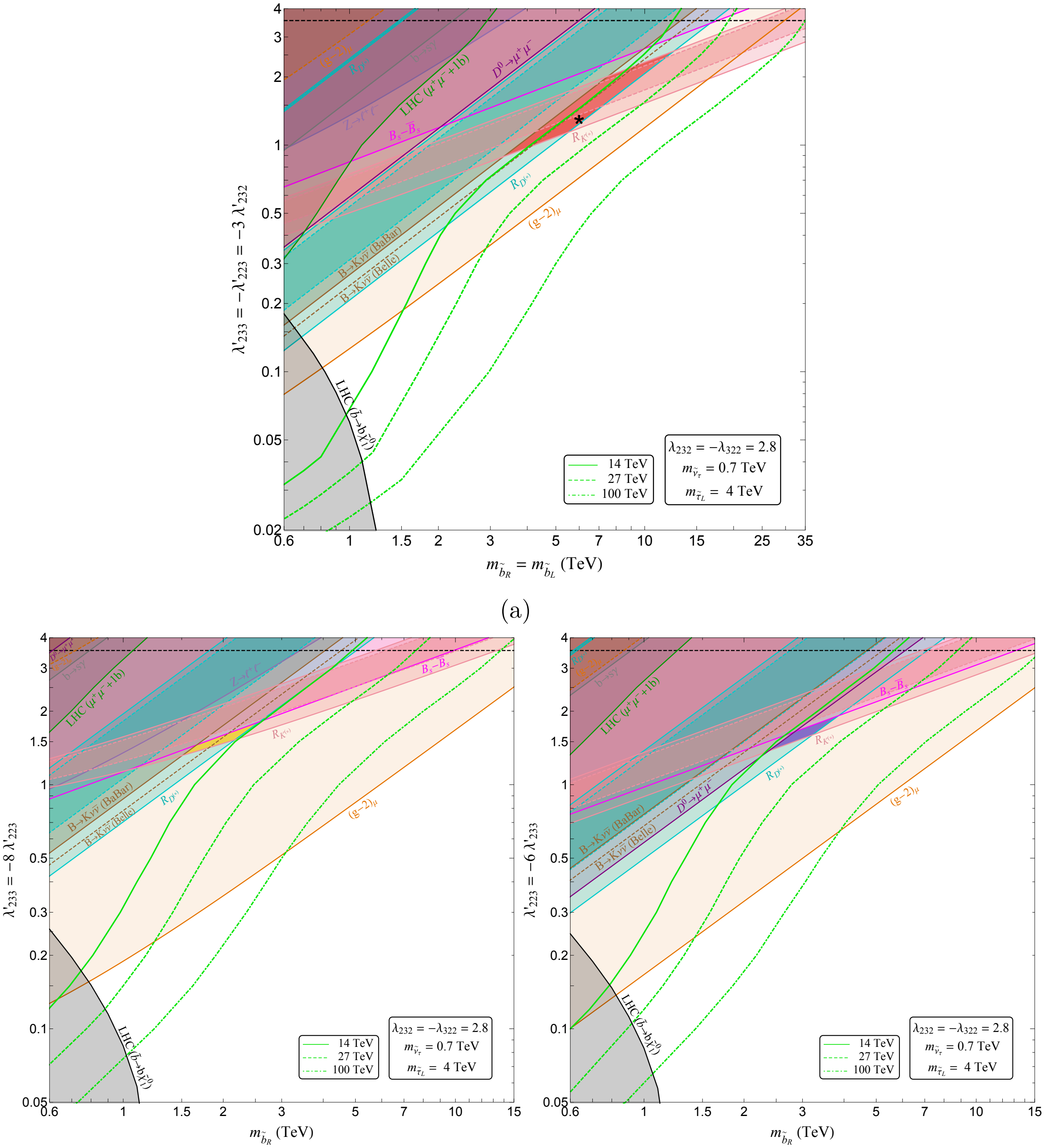

(a)

(b)

(c)

Figure 2.5: Three RPV3 benchmark cases in the $(m_{\tilde{b}_R}, \lambda'_{233})$ parameter space explaining the flavor anomalies. The cyan, pink and orange shaded regions with solid (dashed) boundaries explain the $R_{D^{(*)}}$, $R_{K^{(*)}}$ and $(g-2)_\mu$ anomalies at 3σ (2σ) respectively. The black-shaded region is excluded by the current LHC search for sbottoms in the bottom+neutralino channel, whereas the dark green-shaded region is the LHC exclusion derived from a $\mu^+\mu^- + 1b$ search. The horizontal dotted line shows the perturbativity limit of $\sqrt{4\pi}$.

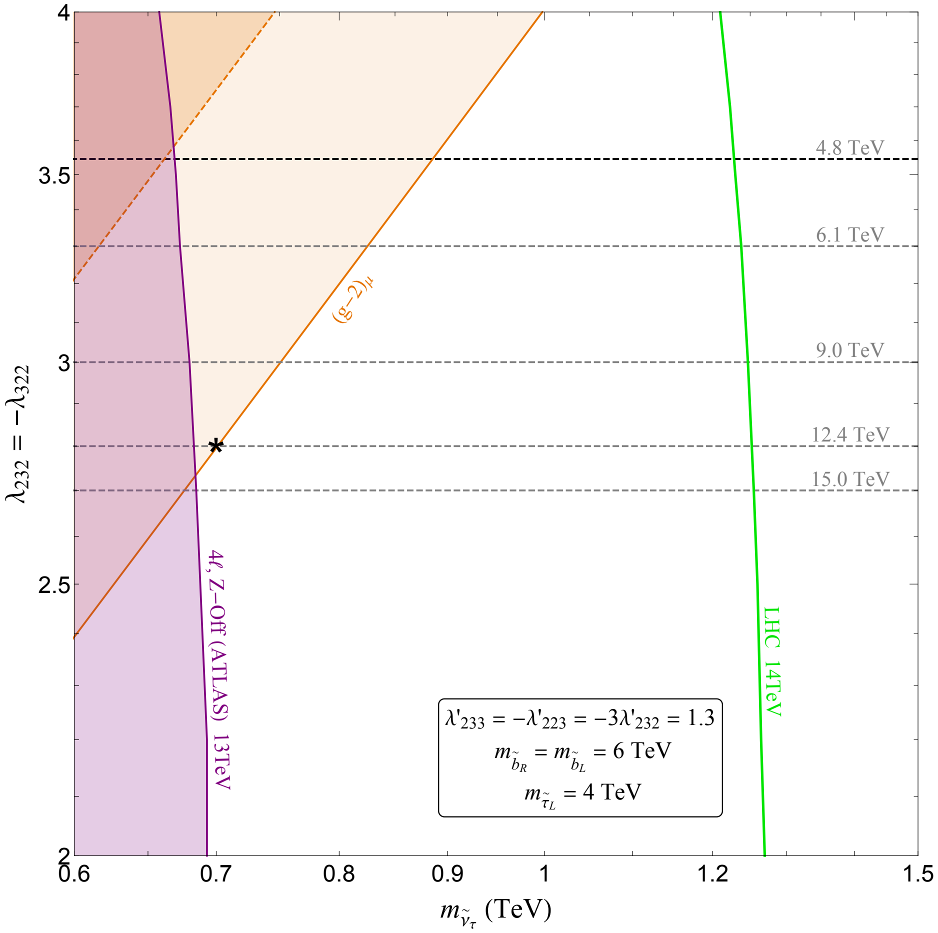

Figure 2.6: The $(g-2)_\mu$-preferred region (orange-shaded) of the $(m_{\tilde{\nu}_\tau}, \lambda_{232})$ parameter space. The purple-shaded region is excluded by a 13 TeV LHC multi-lepton search, whereas the green curve is the 14 TeV HL-LHC sensitivity. The horizontal (gray) dashed lines show the positions of the Landau pole for given λ-couplings and the black dashed line shows the perturbativity limit. The $*$ gives representative values of $m_{\tilde{\nu}_\tau}$ and λ_{232} used in Fig. 2.5.

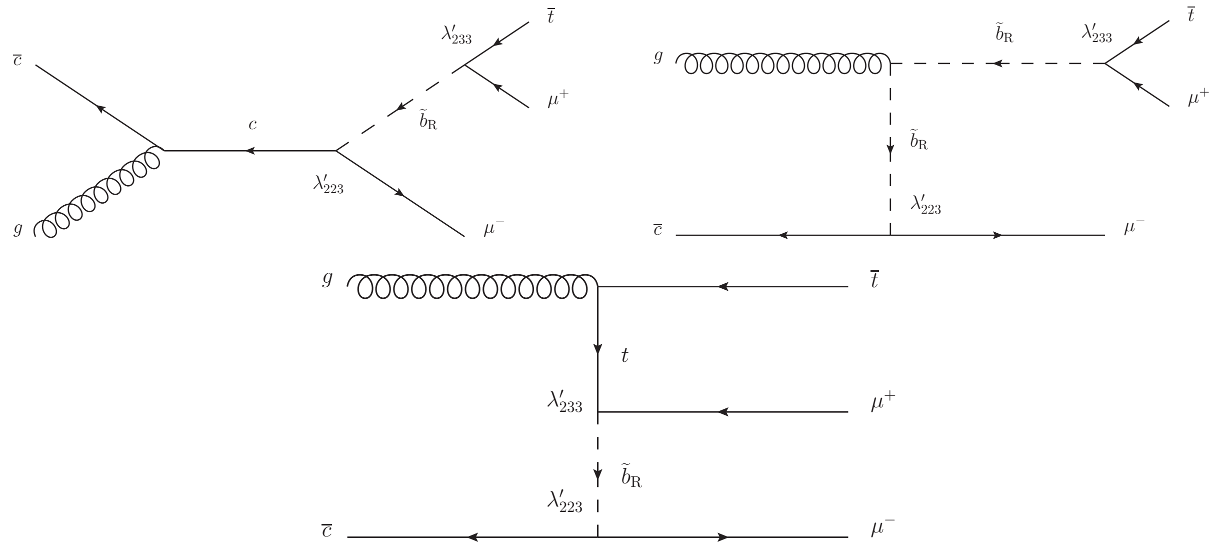

Figure 2.7: Representative Feynman diagrams for the signal process $pp \to \bar{t}\mu^+\mu^-$. There are similar diagrams for the process $pp \to t\mu^+\mu^-$, however, the SM background is larger for top-quark final states, compared to the anti-top, so we only consider the latter case for drawing the sensitivity contours in Fig. 2.5.

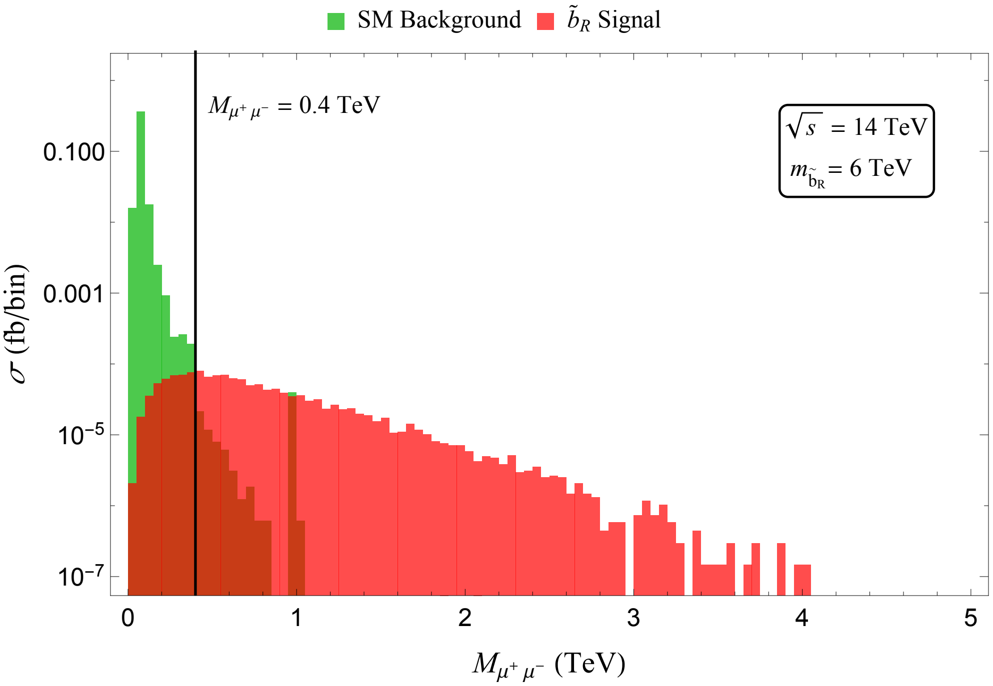

Figure 2.8: Dimuon invariant mass distribution for the RPV3 signal at the $*$ point in BP1 (red) and SM background (green) in the $pp \to \bar{t}\mu^+\mu^-$ channel at 14 TeV LHC.

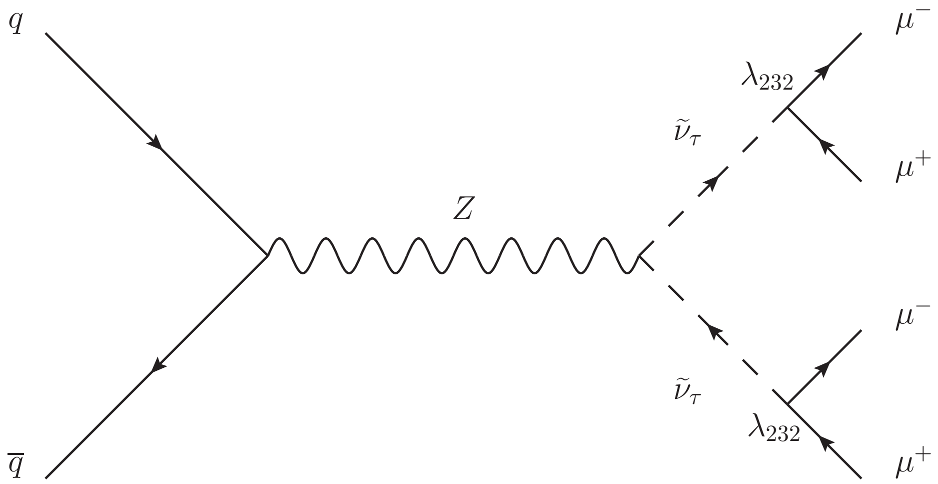

Figure 2.9: Feynman diagram for the four-lepton signal from the sneutrino pair-production in our RPV3 model.

Chapter 3: Muon (g - 2) Anomaly at LHC with Four Lepton Final States

This chapter is based on my work with Yoav Afik, P. S. Bhupal Dev, and Amarjit Soni [62].

3.1 Introduction

The longstanding muon $(g-2)$ anomaly, as well as some hints of lepton flavor universality violation in B-meson decays, could be signaling new physics beyond the Standard Model (SM). A minimal R-parity-violating supersymmetric framework with light third-generation sfermions (dubbed as 'RPV3') provides a compelling solution to these flavor anomalies, while simultaneously addressing other pressing issues of the SM.

In Chapter 2, we demonstrated the orthogonality between the parameter spaces associated with the tau sneutrino and sbottom in our RPV3 scenarios. This orthogonality is significant because it allows us to investigate the muon $(g-2)$ anomaly and B-physics anomalies independently, without affecting each other. Building upon this feature, we proposed an alternative scenario within the sneutrino parameter space that specifically addresses the muon $(g-2)$ anomaly while remaining compatible with the $R_{D^{(*)}}$ and $R_{K^{(*)}}$.

Furthermore, as we will discuss in detail in this chapter, the muon $(g-2)$ anomaly is closely connected to the observation of four-lepton signals at the LHC and other high-energy colliders in our RPV scenarios. These distinctive signals provide a valuable opportunity to test the validity of our models and differentiate the LLE couplings that play a role in contributing to the muon $(g-2)$ anomaly.

The magnetic moment of the muon (g_μ) is one of the most precisely measured quantities in particle physics and an important ingredient to precision tests of the Standard Model [194]. Intriguingly, the anomalous magnetic moment of the muon, $a_\mu \equiv (g_\mu - 2)/2$, arising from loop corrections to the fermionic electromagnetic vertex, was found to have a 3.7σ discrepancy between the experimental value from the E821 experiment at Brookhaven and the SM prediction [32]. The situation became even more interesting recently, as the first result from the Fermilab Muon $(g-2)$ experiment [33], utilizing a more intense muon beam and improved detectors was shown to be consistent with the old Brookhaven measurement to six significant figures. When combined and compared with the world average of the SM prediction using the "R-ratio method" [84], the discrepancy increases to 4.2σ:

$$\Delta a_\mu \equiv a_\mu^{\mathrm{exp}} - a_\mu^{\mathrm{SM}} = (251 \pm 59) \times 10^{-11}\,. \tag{3.1}$$

It should be noted here that simultaneously with the announcement of the Fermilab result in 2021, a new lattice simulation result from the BMW collaboration was also published [34]. The BMW result for the leading hadronic contribution to a_μ reduces the discrepancy in Δa_μ to only 1.5σ. At that time most other lattice collaborations did not have their results available. This situation has changed now. Several lattice collaborations have made their results available [35, 36, 37, 38, 39, 40] in the "intermediate distance regime", i.e. from 0.4 to 1.0 fermi. In that intermediate regime, almost all lattice collaborations now seem to agree with BMW. The interpretation of these new lattice results seems to be that the tension with the experiment is only of order 3.1σ, i.e. somewhat less than the R-ratio method indicated. However, the new lattice results are in some tension with the low energy $e^+e^- \to$ hadrons cross-section data [109, 110, 195, 40], so further clarification is needed. In the coming years, more refined lattice results should be forthcoming and are eagerly awaited. Until all these issues get resolved we choose to use the discrepancy quoted in Ref. [33] and shown in Eq. (3.1).

Taking the muon $(g-2)$ anomaly at face value, one could ask what kind of beyond the SM physics might be responsible. The answer is many [196, 197, 198]. The leading one-loop contribution from any new physics (NP) source is parametric of the order of

$$a_\mu^{\rm NP} \sim \frac{g_{\rm NP}^2}{16\pi^2}\frac{m_\mu^2}{m_{\rm NP}^2}\,, \tag{3.2}$$

which should coincidentally be at the same level as the SM electroweak contribution [199]

$$a_\mu^{\rm EW}[1-{\rm loop}] = \frac{g^2}{16\pi^2}\frac{m_\mu^2}{m_W^2} f \simeq 194.8\times 10^{-11}\,, \tag{3.3}$$

(where $f = \left[5+(1-4\sin^2\theta_W)^2\right]/12 \simeq 0.4$) in order to explain the discrepancy in Eq. (3.1). Hence, there are essentially two types of solutions, depending on whether the new physics contains (i) small couplings and small masses compared to the electroweak scale, as in axion, dark photon, and light Z' models; or (ii) $\mathcal{O}(1)$ interactions and $\mathcal{O}(100~\text{GeV})$ masses, In some new physics models, the SM-like scaling $a_\mu^{\rm NP} \propto m_\mu^2$ in Eq. (3.2) can be avoided by chiral enhancement inside the loop, thus allowing for viable solutions with higher masses up to tens of TeV [153, 200, 201], as in two-Higgs doublet, supersymmetry, and leptoquark models [196, 197]. There is no restriction on the new particle(s) in the loop contributing to $g-2$, except that in most cases we need to invoke flavor non-universal couplings to avoid other experimental constraints. In this context, the models with a new coupling to the $\mu-\tau$ sector are particularly appealing, because of the relatively weaker constraints involving the tau lepton. We will assume this to be the case for the solution to the muon $(g-2)$ anomaly, and explore how this scenario can be directly tested at the LHC using final states with two muons and two taus.[1]

A particularly attractive BSM scenario is R-parity violating supersymmetry (RPV-SUSY) [117], which has the virtue to address many shortcomings of the SM, such as nonzero

---

[1] For other interesting ideas on testing the muon $(g-2)$ at colliders, see e.g. Refs. [202, 203, 204, 205]. The same final state was also considered in Ref. [206] in the context of an $SU(2)_H$ model for large neutrino magnetic moments.

neutrino masses, radiative stability of the Higgs boson, radiative electroweak symmetry breaking, stability of the electroweak vacuum, gauge coupling unification, (gravitino) dark matter and baryogenesis. Here we focus on a minimal, well-motivated RPV-SUSY framework with the third-generation superpartners lighter than the first two, hence dubbed as 'RPV3' [113], which preserves all the attractive features of SUSY mentioned above. On top of that, it was shown in Chapter 2 that RPV3 can simultaneously explain the muon $(g-2)$ anomaly, along with other persistent hints of lepton flavor universality violation in semileptonic B-meson decays, most significantly the $R_{D^{(*)}}$ and $R_{K^{(*)}}$ anomalies.[2] The important feature of the RPV3 solution proposed in Chapter 2 is that the muon $(g-2)$ anomaly is primarily governed by the LLE-type interactions [cf. Eq. (3.4)], while the $R_{D^{(*)}}$ and $R_{K^{(*)}}$ anomalies are governed by the LQD-type interactions [cf. Eq. (3.5)]. This mutual orthogonality allows us to explore here the LHC prospects of probing the muon $(g-2)$-preferred parameter space, irrespective of the fate of the B-anomalies.

For the benchmark scenario considered in Chapter 2 with only $\lambda_{232} = -\lambda_{322} \neq 0$ (and all other $\lambda_{ijk} = 0$), there is a spectacular four-muon signal at the LHC [170], coming from the tau sneutrino pair-production, followed by each sneutrino decaying into two muons via the λ_{232} coupling. Recasting a recent ATLAS multilepton analysis [162], we obtained a lower bound of $m_{\tilde{\nu}_\tau} \gtrsim 670$ GeV, which ruled out most of the muon $(g-2)$-preferred region and pushed the λ_{232} coupling toward the perturbative limit of $\sqrt{4\pi}$.

Given the fact the collider signals involving tau final states are in general less constrained than those involving electrons or muons, in this Chapter we explore a new RPV3 benchmark with $\lambda_{233} = -\lambda_{323} \neq 0$, which leads to a final state with two muons and two taus at the LHC [cf. Fig. 3.2]. To the best of our knowledge, there are no existing constraints on sneutrinos that can be directly applied to this scenario (without any additional assumptions),

---

[2] For reviews of the B-anomalies and BSM interpretations, see e.g. Refs. [65, 207]. For RPV-SUSY interpretations of the flavor anomalies, see also Refs. [128, 135, 129, 208, 136, 137, 131, 132, 133, 134, 138, 139, 209, 210].

except the model-independent LEP limit of $m_{\tilde{\nu}_\tau} > 41$ GeV from Z invisible decay width measurements [211]. Our goal in this chapter is to remedy this situation and derive the first direct LHC limit on sneutrinos for the $\lambda_{233} \neq 0$ case. To this end, we repurpose a recent ATLAS analysis [212] to study the $\mu^+\mu^-\tau^+\tau^-$ signal and background at $\sqrt{s} = 13$ TeV LHC with an integrated luminosity of 139 fb^{-1}. As a result, we are able to put a new robust lower limit on $m_{\tilde{\nu}_\tau}$ extending to about 400 GeV. When contrasted with the muon $(g-2)$-preferred region, we get a conclusion similar to Chapter 2, i.e. only large values of λ_{233} close to the perturbative limit are compatible with the muon $(g-2)$ anomaly in this scenario. We also give the future projections at the high-luminosity phase of the LHC (HL-LHC), which will be able to completely probe the remaining muon $(g-2)$-preferred parameter space, thus providing an independent probe of the muon $(g-2)$ anomaly.

3.2 Muon $(g-2)$ in the RPV3 Framework

As suggested earlier [113, 80, 61], the RPV3 framework provides an appealing solution to the flavor anomalies. The relevant pieces of the Lagrangian read as follows:[3]

$$\begin{aligned}
\mathcal{L}_{LLE} =& \frac{1}{2}\lambda_{ijk}[\tilde{\nu}_{iL}\bar{e}_{kR}e_{jL} + \tilde{e}_{jL}\bar{e}_{kR}\nu_{iL} + \tilde{e}^*_{kR}\bar{\nu}^c_{iL}e_{jL} \\
& - (i \leftrightarrow j)] + \text{H.c.} \qquad (3.4) \\
\mathcal{L}_{LQD} =& \lambda'_{ijk}[\tilde{\nu}_{iL}\bar{d}_{kR}d_{jL} + \tilde{d}_{jL}\bar{d}_{kR}\nu_{iL} + \tilde{d}^*_{kR}\bar{\nu}^c_{iL}d_{jL} \\
& - \tilde{e}_{iL}\bar{d}_{kR}u_{jL} - \tilde{u}_{jL}\bar{d}_{kR}e_{iL} - \tilde{d}^*_{kR}\bar{e}^c_{iL}u_{jL}] + \text{H.c.} \qquad (3.5)
\end{aligned}$$

Note that the simultaneous presence of λ and λ' couplings is consistent with proton decay constraints, as long as the relevant λ" (UDD-type) couplings are either switched

---

[3] We have ignored the bilinear RPV couplings in this work.

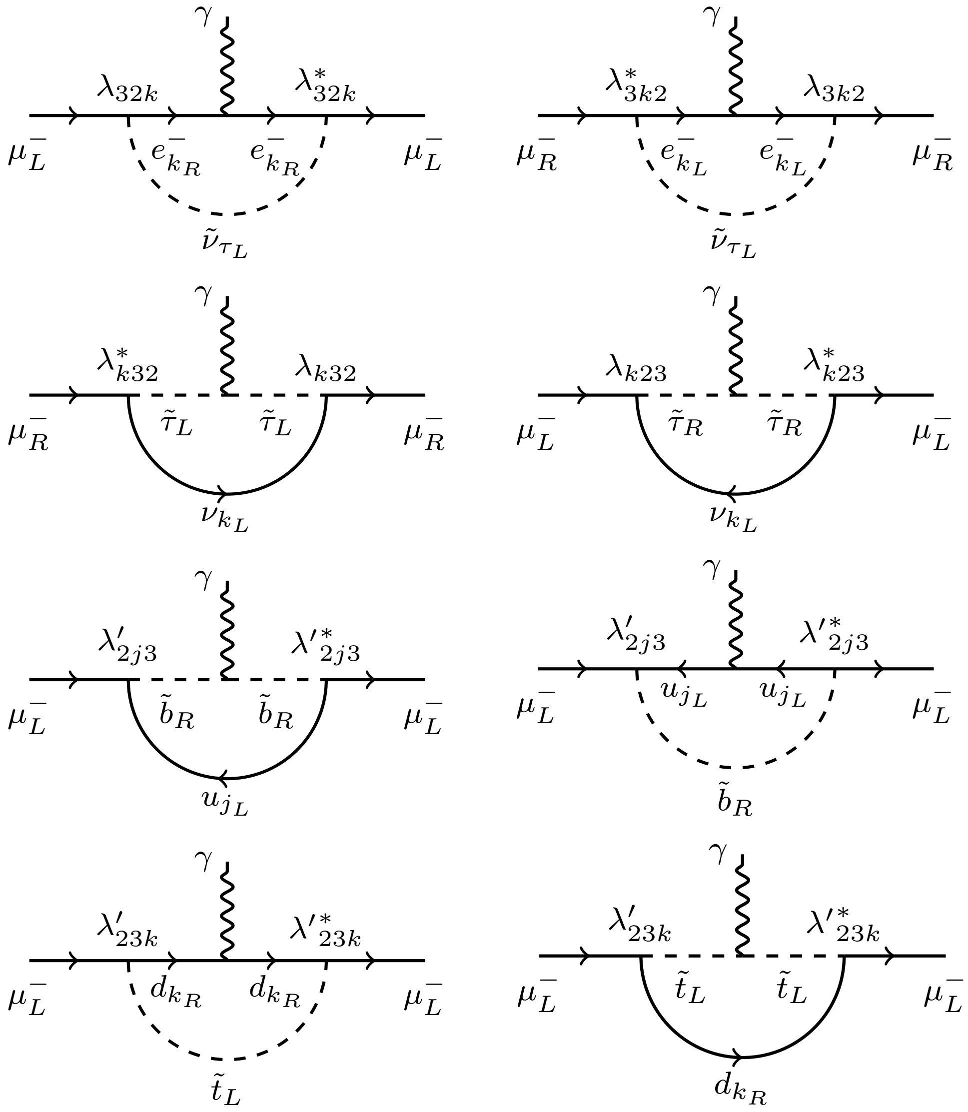

Figure 3.1: Relevant contributions to the muon $(g-2)$ from λ and λ' couplings in our RPV3 scenario. Note that the stop contributions (the last two diagrams) add up to zero.

off or sufficiently small. In general, the above Lagrangians feature $3^3 = 27$ independent λ'_{ijk} couplings and $3^2 = 9$ independent λ_{ijk} couplings.[4] However, in the RPV3 framework with the first two generations of sfermions decoupled, the total number of relevant RPV couplings reduces to $19 + 7 = 26$. Moreover, because of the orthogonality between the $R_{D^{(*)}}$, $R_{K^{(*)}}$-preferred region which is mostly controlled by the λ' couplings and the muon

---

[4] λ_{ijk} is antisymmetric in the first two indices.

$(g-2)$-preferred region which is controlled by the λ couplings, we only focus on the λ couplings in this chapter and find a new solution for the muon $(g-2)$ anomaly with $\lambda_{233} \neq 0$, without affecting the allowed parameter space for $R_{D^{(*)}}$ and $R_{K^{(*)}}$ reported in Ref. [61].

The RPV3 contributions to $(g-2)_\mu$ can, in principle, arise from both λ and λ' couplings [140], as shown in Fig. 3.1. Applying the general results from Ref. [213], one obtains [140]

$$\Delta a_\mu = \frac{m_\mu^2}{96\pi^2} \sum_{k=1}^{3} \left(\frac{2(|\lambda_{32k}|^2 + |\lambda_{3k2}|^2)}{m_{\tilde{\nu}_\tau}^2} - \frac{|\lambda_{k32}|^2}{m_{\tilde{\tau}_L}^2} - \frac{|\lambda_{k23}|^2}{m_{\tilde{\tau}_R}^2} + \frac{3|\lambda'_{2k3}|^2}{m_{\tilde{b}_R}^2} \right) . \tag{3.6}$$

Note that the λ'-contribution, as well as the λ-contribution from sneutrinos, is always positive definite, whereas the λ-contribution from staus has the wrong sign and is required to be sub-dominant in order to explain the observed discrepancy in Eq. (3.1).[5] As a rough estimation of Eq. (3.6), to get the center value of Δa_μ, the terms in the parentheses (masses in TeV) should be ~ 213. To reach the 3σ lower bound of Δa_μ, the terms in the parentheses (masses in TeV) should be $\gtrsim 63$. For a 400 GeV $\tilde{\nu}_\tau$, to satisfy $(g-2)_\mu$, we need the coupling $|\lambda_{233}| > 2.3$.

As shown in Chapter 2, the λ'-contribution from sbottom is sub-dominant to the λ-contribution from sneutrinos, mainly because the LHC lower limits on the masses of colored sfermions like the sbottom are much stronger than those on sneutrinos. In particular, $m_{\tilde{b}_R}$ is typically between 1.5 TeV and 10 TeV, and $|\lambda'|/(m_{\tilde{b}_R}/1\ \text{TeV}) \lesssim 1$ to explain the $R_{D^{(*)}}$ and $R_{K^{(*)}}$ anomalies [61]. This makes the sbottom contribution to muon $(g-2)$ negligible.

Thus, focusing only on the λ-contributions in Eq. (3.6), we see that there are only four relevant couplings, namely, λ_{132}, λ_{231}, λ_{232} and λ_{233}, that lead to a positive contribution

---

[5] R-parity preserving SUSY contributions involving smuons and muon sneutrinos [152, 154, 214] are small in RPV3 because the first two generations of sfermions are heavy.

to Δa_μ in Eq. (3.6). However, any two of them cannot be large simultaneously because of the lepton flavor violation constraints from low-energy processes like $\tau^- \to e^- \mu^+ \mu^-$, $\tau^- \to \mu^- \mu^+ \mu^-$, $\mu \to e\gamma$, etc. Therefore, it is safe to assume only one of these couplings to be large, while the rest can be set to zero.

In Chapter 2, the nonzero coupling was chosen to be λ_{232}, which led to four-muon final states at the LHC via resonant sneutrino-pair production. Here, we study the case where $\lambda_{233} \neq 0$, which leads to a final state of two muons and two taus at the LHC. We expect this case to be more promising, because of the relatively weaker LHC constraints on signals with tau final states, which in turn are expected to give a weaker bound on the sneutrino mass, thus allowing for a larger contribution to Δa_μ, since it is inversely proportional to the square of sneutrino mass [cf. Eq. (3.6)]. For instance, for $m_{\tilde{\nu}_\tau} \sim 100$ GeV, $\lambda_{233} \sim 1$ can explain the central value of Δa_μ in Eq. (3.1). The remaining two cases, namely with either λ_{132} or λ_{231} nonzero, which give rise to final states with two electrons and two muons, will give a bound on the sneutrino mass comparable to that in the four-muon case studied in Ref. [61].

We have also assumed λ'_{311} to be small in order to avoid the resonance production of $\tilde{\nu}_\tau$, which gives stringent bounds from the LHC. For $\lambda'_{311} = 0.1$, the limit on $m_{\tilde{\nu}_\tau}$ is $\mathcal{O}(\text{TeV})$ [215]. For the sub-TeV $\widetilde{\nu_\tau}$ considered here, we therefore need $\lambda'_{311} < \mathcal{O}(0.01)$.

3.2.1 Low-energy Constraints

With $\lambda_{233} = -\lambda_{323} \neq 0$ (and all other $\lambda_{ijk} = 0$), the left-handed stau contribution to Δa_μ in Eq. (3.6) is absent. As for the right-handed stau contribution, which is of the wrong sign, we need to make sure that it is sub-dominant to the sneutrino contribution. This is automatically enforced by the low-energy constraint from tau decay because $\tilde{\tau}_R$ with coupling $\lambda_{233} \neq 0$ has a tree-level contribution to the process $\tau \to \mu\nu\bar{\nu}$. The effective four-fermion Lagrangian for the tau decay (after integrating out the $\tilde{\tau}_R$) is

$$\mathcal{L}^{\lambda_{233}}_{\tau\to\mu\nu\bar{\nu}} \;=\; -\frac{|\lambda_{233}|^2}{2m^2_{\tilde{\tau}_R}}(\overline{\mu}_L\gamma^\mu\nu_{\mu L})(\bar{\nu}_{\tau L}\gamma_\mu\tau_L). \tag{3.7}$$

The effective Lagrangian has the same chiral structure as the SM contribution to tau decay. This can only affect the g^V_{LL} coupling (in the notation of Ref. [216]), and because of the normalization condition of the couplings, our scenario does not influence the Michel parameters [53].

However, it still affects the $e-\mu$ universality in tau decays, measured by the ratio

$$R_{\mu e} \equiv \frac{\Gamma(\tau\to\mu\nu\bar{\nu})}{\Gamma(\tau\to e\nu\bar{\nu})}\,. \tag{3.8}$$

The SM prediction including mass effects gives $R^{\rm SM}_{\mu e} = 97.26\%$ while the experimental measurement prefers a slightly larger central value $R^{\rm exp}_{\mu e} = (97.62 \pm 0.28)\%$ [194]. The ratio between the experimental value and the theoretical prediction in our scenario is given by

$$\frac{R^{\rm exp}_{\mu e}}{R^{\rm SM}_{\mu e}} \simeq \left(1+\frac{1}{4\sqrt{2}G_{\rm F}}\frac{|\lambda_{233}|^2}{m^2_{\tilde{\tau}_R}}\right)^2\,, \tag{3.9}$$

where G_F is the usual Fermi constant. Allowing for 3σ uncertainty in the experimental value, we obtain a limit on λ_{233} as

$$|\lambda_{233}| \lesssim 0.65\left(\frac{m_{\tilde{\tau}_R}}{1\text{ TeV}}\right). \tag{3.10}$$

A slightly stronger limit can be derived by comparing the decays $\tau\to\mu\nu\bar{\nu}$ and $\mu\to e\nu\bar{\nu}$ [217], which is described by the observable

$$R_{\tau/\mu} \equiv \frac{\mathrm{BR}(\tau \to \mu\nu\bar{\nu})_{\mathrm{exp}}/\mathrm{BR}(\tau \to \mu\nu\bar{\nu})_{\mathrm{SM}}}{\mathrm{BR}(\mu \to e\nu\bar{\nu})_{\mathrm{exp}}/\mathrm{BR}(\mu \to e\nu\bar{\nu})_{\mathrm{SM}}}. \tag{3.11}$$

The current value is measured to be $R_{\tau/\mu} = 1.0022 \pm 0.0030$ [131]. Using expressions analogous to Eq. (3.9), and taking 3σ uncertainties in the measured value, it converts to a slightly stronger bound on λ_{233}:

$$|\lambda_{233}| \lesssim 0.61 \left(\frac{m_{\tilde{\tau}_R}}{1\ \mathrm{TeV}}\right). \tag{3.12}$$

Eq. (3.12) is satisfied for any $|\lambda_{233}| < \sqrt{4\pi}$ (perturbative limit), as long as $m_{\tilde{\tau}_R} \gtrsim 5.8$ TeV. For such $m_{\tilde{\tau}_R}$ values, the $\tilde{\tau}_R$ contribution to Δa_μ can be safely neglected.

3.2.2 Neutrino Mass Constraint

The *LLE* interactions contribute to neutrino mass at one-loop level through the lepton-slepton loop [190, 191, 218, 117]. In the RPV3 scenario, we have

$$\begin{aligned} M^{\nu}_{ij} \simeq & \frac{1}{16\pi^2} \sum_k \lambda_{ik3}\lambda_{j3k} m_{e_k} \frac{(\widetilde{m}^e_{LR})^2_{33}}{m^2_{\tilde{\tau}_R} - m^2_{\tilde{\tau}_L}} \log\left(\frac{m^2_{\tilde{\tau}_R}}{m^2_{\tilde{\tau}_L}}\right) \\ & + (i \leftrightarrow j)\,, \end{aligned} \tag{3.13}$$

where $(\widetilde{m}^e_{LR})^2$ is the left-right slepton mixing matrix, given by

$$(\widetilde{m}^e_{LR})^2_{ij} = \frac{v_d}{\sqrt{2}} \left(A^e_{ij} - \mu \tan\beta\, y^e_{ij}\right)\,, \tag{3.14}$$

where A^e is the soft trilinear term, μ is the Higgs-Higgs mixing (or off-diagonal Higgsino mass) term, y^e is the lepton Yukawa coupling, and $\tan\beta = v_u/v_d$ is the ratio of the vacuum expectation values of the two Higgs doublets. In the basis of diagonal charged lepton masses, it is customary to assume that the A-term is proportional to the Yukawa coupling, i.e. $A^e_{33} = A^\tau y^\tau$. We also assume that $m_{\tilde{\tau}_L} = m_{\tilde{\tau}_R}$, in which case $\log\left(m^2_{\tilde{\tau}_R}/m^2_{\tilde{\tau}_L}\right) / \left(m^2_{\tilde{\tau}_R} - m^2_{\tilde{\tau}_L}\right) = 1/m^2_{\tilde{\tau}_R}$. Then Eq. (3.13) simplifies to

$$\begin{aligned} M^\nu_{23} &\simeq \frac{|\lambda_{233}|^2}{8\pi^2}\frac{m^2_\tau}{m^2_{\tilde{\tau}_R}}(A^\tau - \mu\tan\beta) \\ &= (0.05\text{ eV})|\lambda_{233}|^2\left(\frac{6\text{ TeV}}{m_{\tilde{\tau}_R}}\right)^2\frac{(A^\tau - \mu\tan\beta)}{45\text{ MeV}}\,. \end{aligned} \tag{3.15}$$

Thus the neutrino mass constraint can be easily satisfied, albeit with some fine-tuning in the SUSY parameters A^τ and $\mu\tan\beta$, which however do not affect the muon $(g-2)$ solution in our case.

3.3 Signal and Background Analysis

We use the results of the analysis done by the ATLAS collaboration in Ref. [212], with the data recorded during Run-2 of the LHC at a center-of-mass energy of $\sqrt{s} = 13$ TeV and integrated luminosity of 139 fb^{-1}, which targeted a search for RPV-SUSY in final states with four or more charged leptons (electrons, muons and taus). Later we will emphasize how the signal sensitivity can be enhanced with more dedicated selections.

The $\tau^+\tau^-\mu^+\mu^-$ signal that is relevant to the muon $(g-2)$-anomaly comes from the sneutrino pair-production, followed by each sneutrino decaying into $\tau^-\mu^+$ pair via the λ_{233} coupling, as shown in Fig. 3.2. Note that there are also some contributions to this final state from pair production of muons or taus, followed by sneutrino single production from a lepton leg and its subsequent decay into $\tau^-\mu^+$ pair. However, in the parameter space of interest, we find that the sneutrino single production contributes far less than the pair production shown

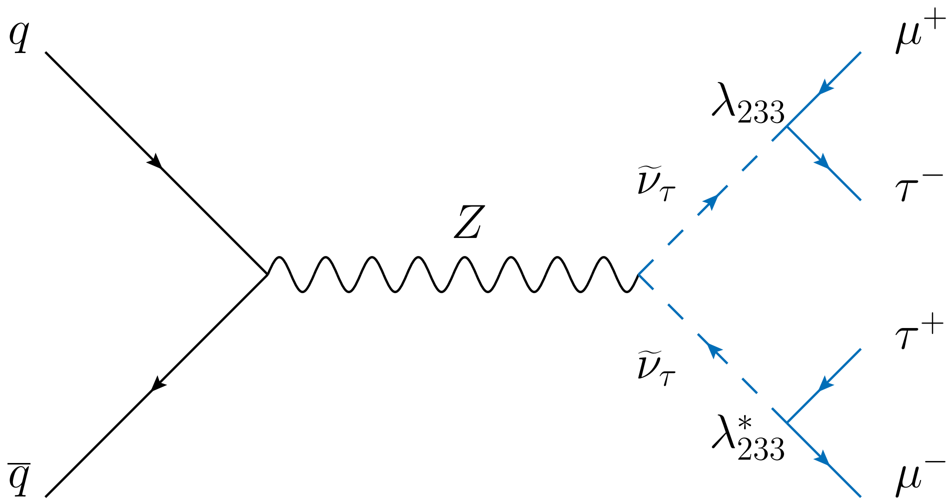

Figure 3.2: Feynman diagram for the $\tau^+\tau^-\mu^+\mu^-$ signal from the sneutrino pair-production in our RPV3 scenario. The blue portion of the figure is closely related to the muon $(g-2)$, i.e. if we join the τ legs and attach a photon to it, it resembles the first two diagrams in Fig. 3.1.

in Fig. 3.2. Also, note that because of the particular structure of the LLE interaction terms in Eq. (3.4), $\tilde{\nu}_\tau \to \tau^+\mu^-$ is not allowed if we assume only $\lambda_{233} \neq 0$, and thus, we cannot have a more distinguishing signal like $\tau^+\tau^+\mu^-\mu^-$ or $\tau^-\tau^-\mu^+\mu^+$ in our scenario.

3.3.1 Simulated Event Samples

All event samples for the signal and the SM backgrounds were generated using MadGraph5_aMC@NLO [169] at leading order (LO) parton-level. The SM background events are not used directly for the estimation of the sensitivity, but as a cross-check that after applying the selections stated in Ref. [212] we get a similar background estimation. In addition, we use the simulation of the SM backgrounds in order to estimate the efficiency of our proposed dedicated selection. For the RPV-SUSY signal, a dedicated universal FeynRules Output (UFO) model was produced using FeynRules [219]. For all of the samples, both signal and background, the 5-flavor scheme was used for the event generation with the NNPDF30LO parton distribution function (PDF) set [220] and the default MadGraph5_aMC@NLO LO dynamical scale, which is the transverse mass calculated by a k_t-clustering of the final-state partons [221]. After generation, events were interfaced with the PYTHIA 8 [222] parton shower, and different jet-multiplicities were matched using the MLM scheme [223] with the default MADGRAPH5_aMC@NLO parameters. Finally, all samples were processed through DELPHES 3 [224], which simulates the detector effects, applies simplified reconstruction algorithms, and was used for the reconstruction of all objects.

According to Ref. [212], the dominant SM backgrounds are ZZ, $t\bar{t}Z$, $VVV\,(V = W, Z)$ and Higgs production. We note that off-shell production is included for W and Z. All of those processes can have four leptons in the final state, similar to our signal. All of those backgrounds were simulated and similar selections of the analysis as in Ref. [212] were applied. In addition to those irreducible backgrounds, there are dominant reducible backgrounds that contain processes that have at least one fake lepton, such as $t\bar{t}$, Z+jets, WZ, WW, WWW, $t\bar{t}W$.

3.3.2 Event Selection and Background

The reconstruction of electrons and muons (light leptons) was done based on efficiency parametrization which depends on transverse momentum (p_{T}) and pseudo-rapidity (η), and with an isolation from other energy-flow objects applied in a cone of $\Delta R = 0.4$. Electrons must have $|\eta| < 2.47$ GeV and $p_{\mathrm{T}} > 7$ GeV, while muons are required to have $|\eta| < 2.7$ GeV and $p_{\mathrm{T}} > 5$ GeV.

The reconstruction of jets was done using the anti-k_t [225] clustering algorithm with radius parameter of $R = 0.4$ implemented in FASTJET [226, 227]. Jets are required to have $p_{\mathrm{T}} > 20$ GeV and $|\eta| < 2.8$. The identification of b-tagged jets was done by applying a p_{T}-dependent weight based on the jet's associated flavor and the MV2c20 tagging algorithm [228] in the 70% working point, which is the default one provided by DELPHES 3.[6]

Hadronically decaying taus have a visible part coming from the hadrons involved in the process and an invisible part coming from the neutrino. The visible part ($\tau_{\mathrm{had}}^{\mathrm{vis}}$) is reconstructed using jets, with $|\eta| < 1.37$ or $1.52 < |\eta| < 2.47$ and $p_{\mathrm{T}} > 20$ GeV [229], using information about the tracks within $\Delta R = 0.2$ of the jet direction.

The missing transverse momentum $\vec{p}_{\mathrm{T}}^{\mathrm{miss}}$ and its magnitude $E_{\mathrm{T}}^{\mathrm{miss}}$ are reconstructed as the negative sum of the p_{T} of all objects in the event and a soft term built from all tracks not associated to any reconstructed object.

The event selection applied in Ref. [212] which yields the best sensitivity for the signal scenario considered here, is noted with two Signal Regions (SRs): $\mathrm{SR2}_{\mathrm{bveto}}^{\mathrm{loose}}$ and $\mathrm{SR2}_{\mathrm{bveto}}^{\mathrm{tight}}$. These SRs contain two light leptons (electrons or muons) and at least two $\tau_{\mathrm{had}}^{\mathrm{vis}}$. In addition, a b-veto is applied by requiring no b-tagged jets in the events. In order to reduce events with a Z-boson decaying to a pair of leptons, events with a pair of opposite-sign and same-flavor (OSSF) leptons within the mass range of $81.2 - 111.2$ GeV are removed. The main discriminating variable used in Ref. [212] is m_{eff}, defined as:

$$m_{\mathrm{eff}} = \sum_i p_{\mathrm{T},\ell_i} + \sum_j p_{\mathrm{T},\tau_{\mathrm{had}_j}^{\mathrm{vis}}} + \sum_k p_{\mathrm{T,jet}_k>40} + E_{\mathrm{T}}^{\mathrm{miss}}, \tag{3.16}$$

where p_{T,ℓ_i} is the p_{T} of a light lepton, $p_{\mathrm{T},\tau_{\mathrm{had}_i}^{\mathrm{vis}}}$ is the p_{T} of a $\tau_{\mathrm{had}}^{\mathrm{vis}}$ and $p_{\mathrm{T,jet}_i>40}$ is the p_{T} of a jet with a minimum transverse momentum of 40 GeV. $\mathrm{SR2}_{\mathrm{bveto}}^{\mathrm{loose}}$ and $\mathrm{SR2}_{\mathrm{bveto}}^{\mathrm{tight}}$ differ from each other by a looser or a tighter selection of m_{eff}, respectively. Based on these SRs, we emphasize how the results would improve with a dedicated selection of only two muons as the light leptons. We call these selections $\mathrm{SR2}_{\mathrm{bveto}}^{\mathrm{loose}}$-$\mu\mu$ and $\mathrm{SR2}_{\mathrm{bveto}}^{\mathrm{tight}}$-$\mu\mu$. All of the selections are summarized in Table 3.1. The distribution of m_{eff} with a selection of only two muons

---

[6] We note that in Ref. [212] the 85% working point is used for b-tagging, but since we have no b-jets in our signal production, the impact of this difference on the signal selection is negligible.

as the light leptons is shown in Fig. 3.3, along with the dominant backgrounds. Additional distributions with our improved selection are given in Appendix B.

3.3.3 Bounds from Current Data

The observed number of signal events with 95% confidence level (CL), S^{95}_{obs}, is reported in Ref. [212]. The meaning of this number is that given a signal hypothesis, if the expected yield in the signal region is higher than S^{95}_{obs}, the signal hypothesis is excluded with 95% CL. For the selection described above, these values are 8.45 and 5.63 for $\text{SR2}^{\text{loose}}_{\text{bveto}}$ and $\text{SR2}^{\text{tight}}_{\text{bveto}}$, respectively. Using these numbers, we set limits on our signal hypothesis.

3.3.4 Expected Improved Bounds

Given the limits set by using an existing analysis, a few remarks are in place:

- In Ref. [212] an inclusive selection of the light lepton flavor is done. In the signal

Table 3.1: Selections for the analysis. $\text{SR2}^{\text{loose}}_{\text{bveto}}$ and $\text{SR2}^{\text{tight}}_{\text{bveto}}$ apply the selection used in ATLAS analysis, while $\text{SR2}^{\text{loose}}_{\text{bveto}}$-$\mu\mu$ and $\text{SR2}^{\text{tight}}_{\text{bveto}}$-$\mu\mu$ apply similar selections, but with only muons as the light leptons.

Selection	$\text{SR2}^{\text{loose}}_{\text{bveto}}$	$\text{SR2}^{\text{loose}}_{\text{bveto}}$-$\mu\mu$	$\text{SR2}^{\text{tight}}_{\text{bveto}}$	$\text{SR2}^{\text{tight}}_{\text{bveto}}$-$\mu\mu$
N_ℓ	$= 2$			
N_μ	0-2	$= 2$	0-2	$= 2$
N_e	0-2	$= 0$	0-2	$= 0$
$N_{\tau^{\text{vis}}_{\text{had}}}$	≥ 2			
N_b	$= 0$			
$m^{\text{OSSF}}_{\ell\ell}$ [GeV]	< 81.2 & > 101.2			
m_{eff} [GeV]	> 600		> 1000	

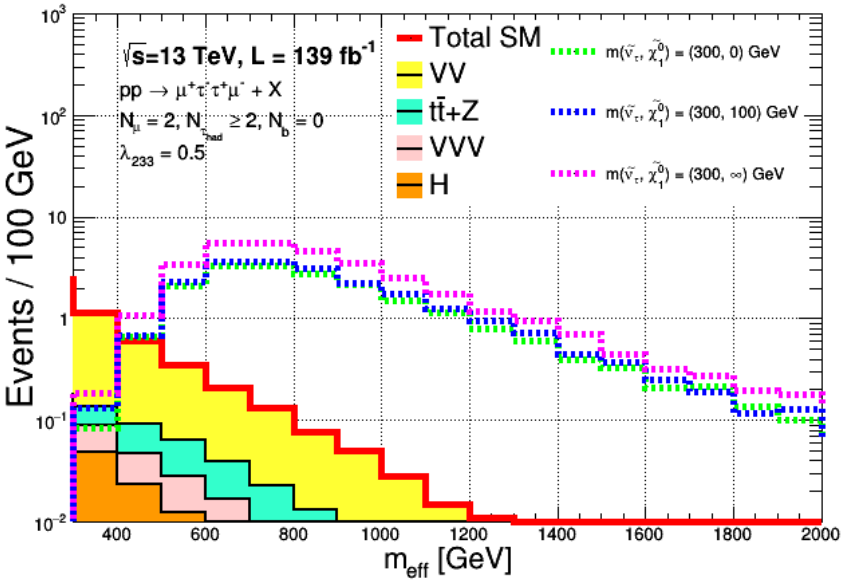

Figure 3.3: Distribution of the effective mass m_{eff} defined in Eq. (3.16). All of the selections of SR2$^{\text{loose}}_{\text{bveto}}$-$\mu\mu$ and SR2$^{\text{tight}}_{\text{bveto}}$-$\mu\mu$ are implemented, as described in Tab. 3.1, beside the m_{eff} selection. Three signal points are presented by setting $m_{\tilde{\nu}_\tau} = 300$ GeV and $\lambda_{233} = 0.5$, for three benchmark values of $m_{\tilde{\chi}_1^0}$: with a very small value (0 GeV), 100 GeV, and a very large value (∞).

hypothesis mentioned in this chapter, only final states with two muons are relevant. This selection is expected to reduce the SM irreducible background, and has no impact on the signal scenario we consider.

- About a third of the background contribution in SR2$^{\text{loose}}_{\text{bveto}}$-$\mu\mu$ is coming from the reducible background. Typically, this background is more dominant for final states with electrons. Therefore, excluding events with electrons is expected to remove a significant part of the reducible background.

In order to estimate how would S^{95}_{obs} change given our new selection, we calculate the expected Z-value, which is the number of standard deviations from the background-only hypothesis given a signal yield and background uncertainty, using the `BinomialExpZ` function by `RooFit` [230]. We scan over different values of the signal yield. Once we get similar

Z-value to the ones from $\mathrm{SR2}^{\mathrm{loose}}_{\mathrm{bveto}}$ and $\mathrm{SR2}^{\mathrm{tight}}_{\mathrm{bveto}}$ in Ref. [212], we set S^{95}_{obs} of $\mathrm{SR2}^{\mathrm{loose}}_{\mathrm{bveto}}$-$\mu\mu$ and $\mathrm{SR2}^{\mathrm{tight}}_{\mathrm{bveto}}$-$\mu\mu$. We do the same procedure for two values of the total integrated luminosity: 139.0 fb^{-1}, as in Ref. [212], which corresponds to the total integrated luminosity recorded during Run-2 of the LHC, and 3000.0 fb^{-1}, which corresponds to the expected integrated luminosity from the HL-LHC.

3.4 Results

We consider three benchmark cases of our scenario where the mass of the lightest neutralino $m_{\widetilde{\chi}^0_1}$ is (a) much smaller than $m_{\tilde{\nu}_\tau}$, (b) equal to a fixed value of 100 GeV, and (c) much larger than $m_{\tilde{\nu}_\tau}$. In Fig. 3.4, the red solid contours show our 95% CL bounds derived in each case in the $(m_{\tilde{\nu}_\tau}, \lambda_{233})$ parameter space from the current 13 TeV LHC Run-2 data with 139 fb^{-1} in the $\tau^+\tau^-\ell^+\ell^-$ channel with $\mathrm{SR2}^{\mathrm{loose}}_{\mathrm{bveto}}$ selection, as given in Tab. 3.1. The orange dashed contours, on the other hand, show the expected improved bounds derived from the same LHC dataset in the $\tau^+\tau^-\mu^+\mu^-$ channel with $\mathrm{SR2}^{\mathrm{loose}}_{\mathrm{bveto}}$-$\mu\mu$ selection, i.e. excluding the electron final states from the selection. The blue and purple dashed contours are the expected improved bounds from the HL-LHC with 3000 fb^{-1} luminosity in the $\tau^+\tau^-\mu^+\mu^-$ channel with $\mathrm{SR2}^{\mathrm{loose}}_{\mathrm{bveto}}$-$\mu\mu$ and with $\mathrm{SR2}^{\mathrm{tight}}_{\mathrm{bveto}}$-$\mu\mu$ selections, respectively. The green, yellow and cyan-shaded regions explain the muon $(g-2)$-anomaly at 1σ, 2σ and 3σ, respectively, while the black solid curve at the middle of the green region gives the best-fit value. The gray-shaded region on the top left corner is the 5σ-exclusion region from muon $(g-2)$. The brown-shaded region in case (b) is excluded by an 8 TeV LHC multi-lepton search [163] [not applicable to cases (a) and (c)]. The horizontal black dot-dashed line shows the perturbativity limit.

We do not show the $\mathrm{SR2}^{\mathrm{tight}}_{\mathrm{bveto}}$ selection results for the 139 fb^{-1} case, because they are found to be weaker than the corresponding $\mathrm{SR2}^{\mathrm{loose}}_{\mathrm{bveto}}$ results. However, as shown in Fig. 3.4, this is not the case for the 3000 fb^{-1} luminosity, where the tight selection gives better results than the loose selection in the large coupling region.

Our analysis for the existing 139 fb^{-1} LHC data uses the selection of $m_{\text{eff}} > 600$ GeV ("loose") while our HL-LHC analysis also uses $m_{\text{eff}} > 1000$ GeV ("tight"). It turns out that when the mass of sneutrino is relatively small, the leptons in the final state are too soft to pass the tight selection of $m_{\text{eff}} > 1000$ GeV. This feature makes the bounds of HL-LHC ($\text{SR2}^{\text{tight}}_{\text{bveto}}$-$\mu\mu$) weaker than the 139 fb^{-1} LHC ($\text{SR2}^{\text{loose}}_{\text{bveto}}$) in the small sneutrino mass region, as can be seen from Fig. 3.4 (a) and (b).

Some of the features in Fig. 3.4 are the same as those found in the four-muon channel [61]. In particular, the LHC bounds are nearly vertical, with a lower limit on the sneutrino mass of $m_{\tilde{\nu}_\tau} \gtrsim 400$ GeV, when λ_{233} is large or when $m_{\tilde{\nu}_\tau} \ll m_{\tilde{\chi}^0_1}$ because the dilepton branching ratio of the sneutrino $\text{BR}(\tilde{\nu}_\tau \to \tau^- \mu^+)$ is dominant in these regions. In Fig. 3.4 (a) and (b), the bounds slowly bend toward the horizontal direction as we decrease the coupling λ_{233} because the $\text{BR}(\tilde{\nu}_\tau \to \tilde{\chi}^0_1 \nu_\tau)$ governed solely by the R-parity conserving gauge coupling (and hence, independent of the λ_{233} coupling) becomes more and more important. Finally, as the mass of the sneutrino gets close to the mass of the neutralino, the bounds asymptotically approach the line $m_{\tilde{\nu}_\tau} = m_{\tilde{\chi}^0_1}$ because the $\tilde{\nu}_\tau \to \tilde{\chi}^0_1 \nu_\tau$ decay becomes kinematically suppressed in this region and $\text{BR}(\tilde{\nu}_\tau \to \tau^- \mu^+)$ is dominant again. This asymptotic feature is out of the range in Fig. 3.4 (a) as the $m_{\tilde{\nu}_\tau}$ value starts from the model-independent lower limit of 41 GeV, derived from the LEP data on the invisible Z decay width [211].

The vertical brown-shaded region in Fig. 3.4 (b) (where $m_{\tilde{\chi}^0_1} = 100$ GeV) is excluded by an old 8 TeV LHC multi-lepton search [163]. But for the cases (a) $m_{\tilde{\chi}^0_1} \ll m_{\tilde{\nu}_\tau}$ and (c) $m_{\tilde{\chi}^0_1} \gg m_{\tilde{\nu}_\tau}$, this search does not apply because the mass of the lightest neutralino is outside the range of their assumption.

The green, yellow and cyan-shaded regions in Fig. 3.4 explain the muon $(g-2)$-anomaly at 1σ, 2σ and 3σ CL, respectively, while the black dashed curve gives the best-fit value. The gray-shaded region on the top left corner gives a Δa_μ discrepancy of more than 5σ, and hence, is disfavored. From Fig. 3.4, we see that the new LHC limits derived here preclude most of the muon $(g-2)$-preferred region in our RPV3 scenario, except for large λ_{233} coupling values close to the perturbative limit (shown by the horizontal black dot-dashed line). The future HL-LHC projected sensitivities shown here could completely cover the remaining 2σ-preferred regions. It should be noted here that the lower boundaries of the yellow and cyan-shaded regions correspond to corrections of the muon $(g-2)$ at 2σ (with $\Delta a_\mu = 133 \times 10^{-11}$) and 3σ (with $\Delta a_\mu = 74 \times 10^{-11}$), respectively. If the new lattice results for the SM prediction come closer to the BMW-reported one, the new central value for Δa_μ is expected to lie somewhere between these two lower boundaries, which in fact opens up a larger allowed parameter space below the perturbativity limit that can be probed at the HL-LHC.

For completeness, we also considered other possible experimental limits for the case (a) $m_{\widetilde{\chi}_1^0} \ll m_{\tilde{\nu}_\tau}$ that could potentially be relevant to the parameter space considered here. In particular, we analyzed the LHC mono-jet [231] and the LEP Z-pair [232] and mono-photon [233] constraints to derive a lower bound on sneutrino mass. First, let us recast the LEP Z-pair data, letting the Z-pair decay into $\tau^+\tau^-\mu^+\mu^-$ final state, which is the same as our signal from sneutrino pair, and allows us to derive a lower bound on the sneutrino mass, since the measured cross-section at LEP was found to be close to the SM expectation. However, we find that the resulting lower bound on the sneutrino mass is about 100 GeV, which is entirely within the current 13 TeV LHC exclusion (inside the red-shaded region in Fig. 3.4). This seems reasonable because the center-of-mass energy of LEP is only 209 GeV and sneutrino pair-production via the Z-boson (similar to Fig. 3.2, but replacing the $q\bar{q}$ with e^+e^-) is kinematically suppressed for sneutrino masses beyond $\sim$ 100 GeV. Similarly, we find that the recast mono-photon bound from LEP for the channel $e^+e^- \to \tilde{\nu}_\tau \tilde{\nu}_\tau^* \to \widetilde{\chi}_1^0 \overline{\widetilde{\chi}}_1^0 \nu\bar{\nu}$

with an initial-state-radiation of photon is always weaker than the model-independent limit on sneutrino mass of 41 GeV because the experimental uncertainty of the measured cross section [233] is relatively large. Similarly, the mono-jet bound from LHC for the channel $pp \to \tilde{\nu}_\tau \tilde{\nu}_\tau^* \to \tilde{\chi}_1^0 \overline{\tilde{\chi}}_1^0 \nu \bar{\nu}$ with an initial-state-radiation of gluon is also weaker than the model-independent LEP limit used here due to small signal cross-section (in the absence of any λ' couplings). For these reasons, the collider constraints we derived in Fig. 3.4 are the strongest so far.

We also note that Ref. [212] considered the cascade decay of sleptons via the neutralino and derived stringent bounds on the sneutrino mass up to 850 GeV, depending on the neutralino mass. Naively, it looks like our scenario (b) is within their exclusion curve. However, we would like to stress that in the ATLAS analysis [212], a mass-degeneracy of charged sleptons and sneutrinos of all three generations is assumed. This assumption introduces many more production and decay channels and makes the cross-section much larger. In our scenario, only the third-generation sneutrino is light (sub-TeV scale), while the others are decoupled. Therefore, the exclusion limits of Ref. [212] cannot be directly compared to our results. Moreover, their results do not cover our scenarios (a) and (c).

3.5 Neutralino Decay

In the above discussion, the lightest supersymmetric particle (LSP) is assumed to be either the lightest neutralino $\tilde{\chi}_1^0$ or the tau sneutrino $\tilde{\nu}_\tau$. For $m_{\tilde{\chi}_1^0} > m_{\tilde{\nu}_\tau}$, the neutralino undergoes prompt decay into $\nu_\tau \tilde{\nu}_\tau$ via its gauge coupling. On the other hand, for $m_{\tilde{\chi}_1^0} < m_{\tilde{\nu}_\tau}$, it undergoes a three-body decay into $\mu^- \tau^+ \nu_\tau$ via an off-shell $\tilde{\nu}_\tau$, with the corresponding decay width given by

$$\Gamma(\tilde{\chi}_1^0 \to \mu^- \tau^+ \nu_\tau) \simeq \frac{g^2 |\lambda_{233}|^2}{512\pi^3} \frac{m_{\tilde{\chi}_1^0}^5}{m_{\tilde{\nu}_\tau}^4}. \tag{3.17}$$

This leads to a typical decay length of

$$\tau(\tilde{\chi}_1^0 \to \mu^- \tau^+ \nu_\tau) \simeq \frac{20\ \text{cm}}{|\lambda_{233}|^2} \left(\frac{1\ \text{GeV}}{m_{\tilde{\chi}_1^0}}\right)^5 \left(\frac{m_{\tilde{\nu}_\tau}}{400\ \text{GeV}}\right)^4 , \tag{3.18}$$

which means that the decay can be either prompt or displaced, depending on the mass and coupling values.

For $m_{\tilde{\chi}_1^0} < m_\tau + m_\mu$, we have the loop-induced decay $\tilde{\chi}_1^0 \to \gamma + \nu(\bar{\nu})$, with the decay width given by [190, 234, 235]

$$\Gamma(\tilde{\chi}_1^0 \to \gamma\nu) \simeq \frac{|\lambda_{233}|^2 \alpha^2 m_{\tilde{\chi}_1^0}^3}{512\pi^3 \cos^2\theta_w} \left[\frac{3m_\tau}{m_{\tilde{\tau}}^2} \left(1 + \log\frac{m_\tau^2}{m_{\tilde{\tau}}^2}\right)\right]^2 \tag{3.19}$$

where α is the fine-structure constant and θ_w is the weak mixing angle. This decay mode is suppressed by the heavy stau mass (which is required to be heavier than 5.8 TeV in our case), with the corresponding decay length given by

$$\tau(\tilde{\chi}_1^0 \to \gamma\nu + \gamma\bar{\nu}) \simeq \frac{10^6\ \text{cm}}{|\lambda_{233}|^2} \left(\frac{1\ \text{GeV}}{m_{\tilde{\chi}_1^0}}\right)^3 \left(\frac{m_{\tilde{\tau}}}{6\ \text{TeV}}\right)^4 , \tag{3.20}$$

which necessarily makes it long-lived.

If gravitino is the LSP (and a potential dark matter candidate), then there is another possible decay mode for the neutralino into gravitino and photon [236]:

$$\Gamma(\tilde{\chi}_1^0 \to \gamma\widetilde{G}) \simeq \frac{\cos^2\theta_w}{48\pi M_{\text{Pl}}^2} \frac{m_{\tilde{\chi}_1^0}^3}{x_{3/2}^2} \left(1 - x_{3/2}^2\right)^3 \left(1 + 3x_{3/2}^2\right) , \tag{3.21}$$

where $x_{3/2} \equiv m_{\widetilde{G}}/m_{\tilde{\chi}_1^0}$. However, this decay mode is suppressed by the square of the Planck mass M_{Pl}, and again, makes the neutralino very long-lived.

3.6 Conclusions

In this chapter, we proposed a new RPV3 scenario for the solution of the muon $(g-2)$ anomaly, which leads to an interesting LHC signal of $\mu^+\mu^-\tau^+\tau^-$ final state. We analyzed the

Run-2 LHC multilepton data to derive stringent constraints on the sneutrino mass and the relevant RPV coupling in this scenario. We then proposed dedicated selection strategies to improve the bound even with the existing dataset. We also showed that the high-luminosity LHC will completely cover the remaining muon $(g-2)$-preferred parameter space, thus providing a robust, independent test of the muon $(g-2)$ anomaly.

The RPV3 framework provides a compelling solution to the persistent hints of lepton flavor universality violation. In this chapter, we have proposed a new RPV3 solution to the muon $(g-2)$-anomaly using the λ_{233} coupling. This is consistent with the low-energy flavor constraints and existing collider bounds. The scenario is also compatible with the $R_{K^{(*)}}$ and $R_{D^{(*)}}$ anomalies whether or not they survive in the end.[7]

For the scenario under consideration, we have constructed new LHC bounds, following an existing ATLAS multi-lepton analysis with the Run-2 data. We have also shown how the bounds would improve with a dedicated selection of only two muons as the light leptons. The HL-LHC prospects were also discussed in this context.

We found that under the current LHC data, the muon $(g-2)$-favored region survives only for $m_{\tilde{\nu}_\tau} \gtrsim 400$ GeV and $\lambda_{233} \gtrsim 2$. Unlike our previous results for the $\lambda_{232} \neq 0$ [61], where $m_{\tilde{\nu}_\tau}$ was required to be larger than $\gtrsim 650$ GeV, our new scenario allows lighter sneutrinos. This is because the $\tilde{\nu}_\tau$ decays into a $\mu\tau$-pair for $\lambda_{233} \neq 0$ rather than a $\mu\mu$ pair for $\lambda_{232} \neq 0$, and taus are more difficult than muons to identify experimentally.

The collider signal of $\mu^+\mu^-\tau^+\tau^-$ that we analyzed here is a generic prediction of any BSM scenario trying to explain the muon $(g-2)$ via a tau-loop, either with or without chirality enhancement. Therefore, the analysis presented here can be extended to all such models, although the specific details, such as the signal cross section or the $(g-2)$-preferred range of model parameters, might be somewhat different.

---

[7] The latest LHCb results [30, 31] seem to indicate that the $R_{K^{(*)}}$ anomaly does not exist anymore.

We expect new results forthcoming from the Fermilab Muon $(g-2)$ experiment, as a lot more data has been accumulated since the first results were announced in 2021. Another muon $(g-2)$ experiment with similar sensitivity but using a different technique is currently under construction at J-PARC [237]. On the theory front, more refined SM calculations for a_μ are currently underway [238]. An independent measurement of the leading order hadronic contribution to a_μ has also been proposed from the MuonE experiment at CERN [239], which is immune to any possible BSM contamination [240, 241]. All in all, it is very likely that the fate of the muon $(g-2)$ anomaly will be sealed beyond a reasonable doubt in the not-so-distant future. Our proposed collider signal will independently test the BSM interpretation of the muon $(g-2)$ anomaly in any model with lepton flavor violating $\mu\tau$ couplings. This may also have implications for lepton flavor universality tests in the B-meson decays.

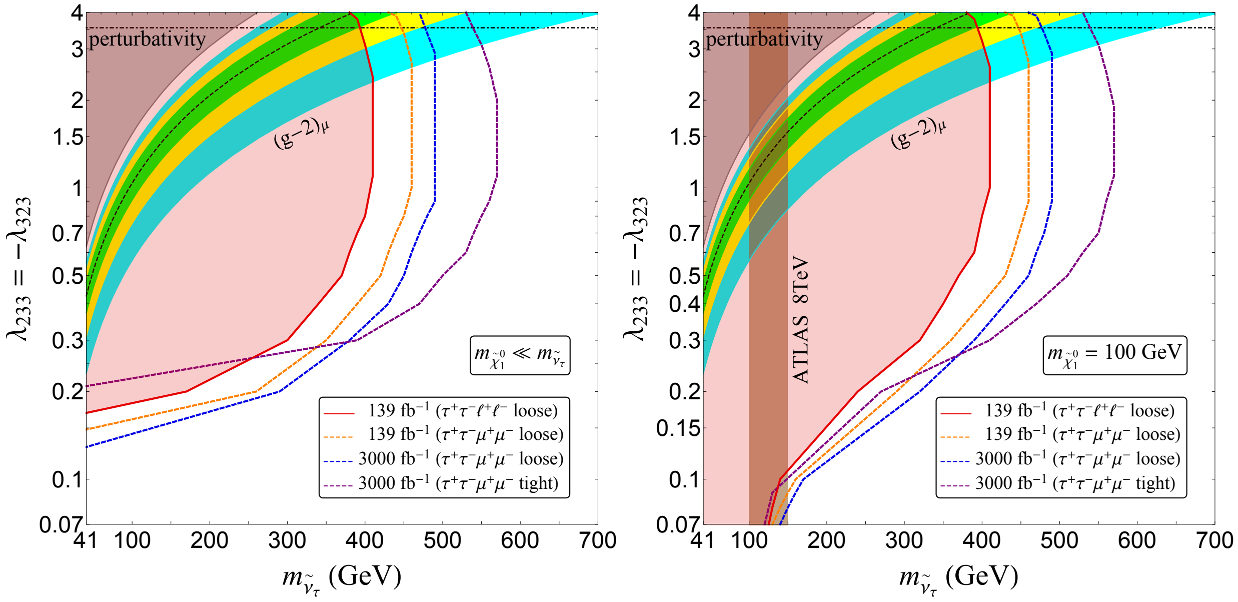

(a) $m_{\widetilde{\chi}_1^0} \ll m_{\tilde{\nu}_\tau}$

(b) $m_{\widetilde{\chi}_1^0} = 100$ GeV

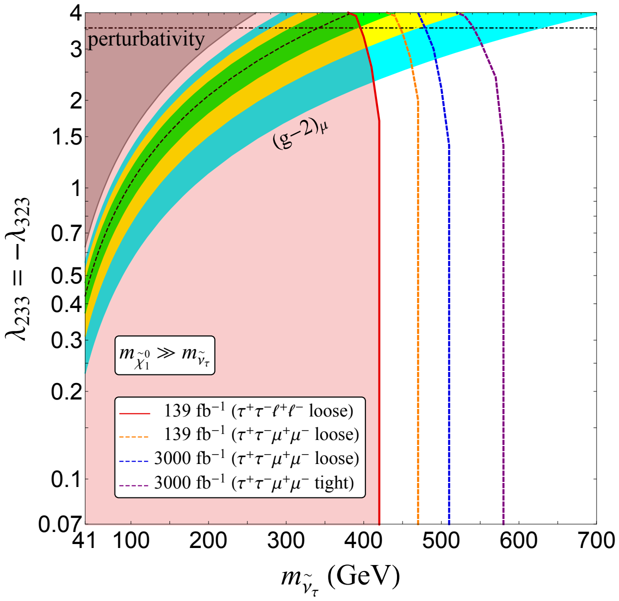

(c) $m_{\widetilde{\chi}_1^0} \gg m_{\tilde{\nu}_\tau}$

Figure 3.4: Three benchmark cases of our RPV3 scenario with $m_{\widetilde{\chi}_1^0}$ (a) much smaller than $m_{\tilde{\nu}_\tau}$, (b) 100 GeV, and (c) much larger than $m_{\tilde{\nu}_\tau}$) in the $(m_{\tilde{\nu}_\tau}, \lambda_{233})$ parameter space. The red (solid) and orange (dashed) contours, respectively, show the 95% CL current bounds derived from the 139 fb^{-1} LHC data in the $\tau^+\tau^-\ell^+\ell^-$ SR2$^{\text{loose}}_{\text{bveto}}$ channel, and the expected improved bounds with the same dataset in the $\tau^+\tau^-\mu^+\mu^-$ SR2$^{\text{loose}}_{\text{bveto}}$-$\mu\mu$ channel, whereas the blue and purple (dashed) contours show the 95% CL sensitivities at HL-LHC with 3000 fb^{-1} luminosity in the $\tau^+\tau^-\mu^+\mu^-$ SR2$^{\text{loose}}_{\text{bveto}}$-$\mu\mu$ and SR2$^{\text{tight}}_{\text{bveto}}$-$\mu\mu$ channels, respectively.

Chapter 4: R-Parity Violating Supersymmetry and Neutrino Non-Standard Interactions

This chapter is based on my work with P. S. Bhupal Dev and Amarjit Soni [63].

4.1 Introduction

In this chapter, we revisit the RPV SUSY (R-parity violating supersymmetry) model and focus on the LLE interaction parts. By considering different λ couplings that introduce non-standard interactions (NSI) for neutrinos, we will investigate how the constraints from lepton flavor violation apply to different models and to the NSI parameters.

In the influential papers [242, 243, 244], that unveiled the matter effect in neutrino oscillations within the framework of the Standard Model, an intriguing possibility was also put forth regarding the presence of additional interactions beyond the known ones. These interactions, known as neutrino non-standard interactions (NSI), were proposed as a potential explanation for the observed matter effect. Since then, there has been a remarkable surge of interest and research aimed at exploring and understanding these novel interactions.

The concept of NSI introduces the notion that neutrinos can interact with matter in ways that go beyond the standard weak interactions predicted by the Standard Model. These interactions can manifest as modifications to the neutrino flavor oscillation probabilities in the presence of matter, leading to deviations from the expected oscillation patterns. NSI parameters, which quantify the strength and nature of these additional interactions, have become a subject of intense investigation.

NSI can be described by introducing an effective Lagrangian that incorporates these additional interactions. This Lagrangian extends the standard electroweak Lagrangian to include terms that account for the non-standard interactions between neutrinos and matter

$$\mathcal{L}_{\text{NSI}}^{\text{NC}} = -2\sqrt{2}G_F \sum_{f,X,\alpha,\beta} \varepsilon_{\alpha\beta}^{fX} \left(\bar{\nu}_\alpha \gamma^\mu P_L \nu_\beta\right) \left(\bar{f}\gamma_\mu P_X f\right), \tag{4.1}$$

$$\mathcal{L}_{\text{NSI}}^{\text{CC}} = -2\sqrt{2}G_F \sum_{f,f',X,\alpha,\beta} \varepsilon_{\alpha\beta}^{ff'X} \left(\bar{\nu}_\alpha \gamma^\mu P_L \ell_\beta\right) \left(\bar{f}'\gamma_\mu P_X f\right), \tag{4.2}$$

where $X = L, R$ and $f, f' \in \{e, u, d\}$.

The vector component of neutrino non-standard interactions refers to the part of the NSI that affects the vector current of the neutrino interaction with matter. In the context of NSI, the vector component is characterized by a set of parameters that quantify the strength and nature of the deviation from the standard weak interactions. These parameters determine the extent to which the neutrino's interaction with matter is modified and can potentially introduce new physics effects.

$$\varepsilon_{\alpha\beta}^{fV} = \varepsilon_{\alpha\beta}^{fL} + \varepsilon_{\alpha\beta}^{fR}. \tag{4.3}$$

The NSI parameters are defined as dimensionless quantities that parameterize the deviations from the standard weak interactions. They quantify the strength and nature of the non-standard interactions and provide a way to characterize the potential new physics effects

$$
\begin{aligned}
\varepsilon_{\alpha\beta} &= \sum_{f\in\{e,u,d\}} \left\langle \frac{N_f(x)}{N_e(x)} \right\rangle \varepsilon_{\alpha\beta}^{fV} \\
&= \varepsilon_{\alpha\beta}^{eV} + \left\langle \frac{N_p(x)}{N_e(x)} \right\rangle \left(2\varepsilon_{\alpha\beta}^{uV} + \varepsilon_{\alpha\beta}^{dV}\right) + \left\langle \frac{N_n(x)}{N_e(x)} \right\rangle \left(\varepsilon_{\alpha\beta}^{uV} + 2\varepsilon_{\alpha\beta}^{dV}\right) \\
&= \varepsilon_{\alpha\beta}^{eV} + \left[2 + Y_n(x)\right] \varepsilon_{\alpha\beta}^{uV} + \left[1 + 2Y_n(x)\right] \varepsilon_{\alpha\beta}^{dV},
\end{aligned}
\tag{4.4}
$$

where $N_f(x)$ is the number density of fermion f at position x. $\big\langle N_p(x)/N_e(x)\big\rangle = 1$ (Assume electric charge neutrality of the medium), $Y_n(x) \equiv \langle N_n(x)/N_e(x)\rangle$ (Define)

The NSI parameters capture the effects of new physics beyond the Standard Model, such as interactions mediated by new particles or interactions involving lepton flavor violation. They provide a phenomenological framework to study the implications of such new physics scenarios in the context of neutrino experiments.

Experimental efforts aimed at detecting and characterizing NSI are underway in various neutrino experiments worldwide. These endeavors involve the precise measurement of neutrino oscillation parameters, the study of neutrino interactions in matter, and the search for signatures of non-standard effects. By probing NSI, researchers hope to unravel the mysteries surrounding neutrinos and shed light on the fundamental properties of these elusive particles.

In this chapter, our focus shifts to exploring the contribution of RPV3 (R-parity violating supersymmetry with the third-generation superpartners much lighter than the first two) to NSI parameters. While NSI can arise from various new physics scenarios, we investigate the specific impact of RPV3 on these parameters.

4.2 RPV3 Framework

In this context, we only consider the *LLE* part of the RPV interactions. This arises from the fact that, under such an assumption, we can assess the maximum neutrino NSI contribution originating from the LLE interactions. Upon introducing additional PRV interactions, further constraints are imposed, resulting in a reduction of the contribution to NSI. Therefore, the primary objective of this study is to evaluate the most favorable NSI contribution stemming from the LLE interaction terms. And the actual NSI contribution from LLE interactions cannot surpass the values in the corresponding cases we have considered in this chapter. The RPV superpotential gives the following relevant LLE Yukawa interactions:

$$\mathcal{L}_{LLE} = \frac{1}{2}\lambda_{ijk}[\tilde{\nu}_{iL}\bar{e}_{kR}e_{jL} + \tilde{e}_{jL}\bar{e}_{kR}\nu_{iL} + \tilde{e}^*_{kR}\bar{\nu}^c_{iL}e_{jL} - (i \leftrightarrow j)] + \text{H.c.}, \tag{4.5}$$

where the LLE couplings are anti-symmetric in the first two indices, i.e. $\lambda_{ijk} = -\lambda_{jik}$. The above Lagrangian has $3^2 = 9$ independent λ_{ijk} couplings. However, in the RPV3 framework with the first two generations of sfermions decoupled, the total number of relevant LLE couplings reduces to 7. Among the 7 LLE couplings, we present in Table 4.1 the possible λ_{ijk} couplings in the RPV3 framework that can lead to neutrino NSI. To account for NSI effects, it is necessary for one index to be 1, while in the context of the RPV3 framework, another index should be 3. The red terms in the table indicate the interactions that can induce NSI, while the other terms may introduce additional constraints that cannot be avoided in each case.

Table 4.1: Possible LLE couplings for neutrino NSI in RPV3 Framework. In order to account for NSI effects, it is necessary for one index to be 1. Additionally, in the context of the RPV3 framework, another index should be 3. The red terms in the table represent the couplings that can induce NSI, while the other terms may also introduce some unavoidable constraints.

λ_{123}	λ_{131}	λ_{132}	λ_{133}	λ_{231}
$\tilde{\tau}^*_R\bar{\nu}^c_{eL}\mu_L$	$\tilde{\tau}_L\bar{e}_R\nu_{eL}$	$\tilde{\tau}_L\bar{\mu}_R\nu_{eL}$	$\tilde{\tau}_L\bar{\tau}_R\nu_{eL}$	$\tilde{\tau}_L\bar{e}_R\nu_{\mu L}$
$-\tilde{\tau}^*_R\bar{\nu}^c_{\mu L}e_L$	$-\tilde{\nu}_{\tau L}\bar{e}_R e_L$	$-\tilde{\nu}_{\tau L}\bar{\mu}_R e_L$	$\tilde{\tau}^*_R\bar{\nu}^c_{eL}\tau_L$	$-\tilde{\nu}_{\tau L}\bar{e}_R\mu_L$
			$-\tilde{\nu}_{\tau L}\bar{\tau}_R e_L$	
			$-\tilde{\tau}^*_R\bar{\nu}^c_{\tau L}e_L$	

From the information provided in Table 4.1, it is evident that the λ_{132} terms cannot contribute to the NSI. Within the scope of this study, we have identified six distinct cases that can cause neutrino NSI: (a) $\lambda_{123} \neq 0$, (b) $\lambda_{131} \neq 0$, (c) $\lambda_{133} \neq 0$, (d) $\lambda_{231} \neq 0$, (e) $\lambda_{123}, \lambda_{133} \neq 0$, and (f) $\lambda_{131}, \lambda_{231} \neq 0$. In each case, only the red interaction terms contribute to the NSI parameters. It is noteworthy that in case (f), the combination of λ_{131} and λ_{231} cannot give a valuable off-diagonal NSI parameter $\varepsilon_{e\mu}$ due to the particularly strong constraint of $\mu \to ee\bar{e}$, where this process receives a BSM contribution at tree level from the LLE interactions in Table 4.1 through the exchange of the tau-sneutrino ($\tilde{\nu}_\tau$). The model-independent lower limit of $m_{\tilde{\nu}_\tau}$ is 41 GeV, derived from the LEP data on the invisible Z decay width [211]. However, the typical limit derived from the multi-lepton search of the $\tilde{\nu}_\tau$ pair production sets values of $\mathcal{O}(\text{TeV})$ on the mass of $\tilde{\nu}_\tau$ [245, 246, 62]. For a $\tilde{\nu}_\tau$ with mass $m_{\tilde{\nu}_\tau} = 1$ TeV, the limit for the production of λ_{131} and λ_{231} is $\lambda_{131}\lambda_{231} < 6.6 \times 10^{-5}$ [247] which lead to the off-diagonal NSI $\varepsilon_{e\mu} < \mathcal{O}(10^{-6})$ for $m_{\tilde{\tau}_L} \sim \mathcal{O}(\text{TeV})$. Hence, in this study, we will not delve further into the analysis of case (f). From now on, we will use a convention in this chapter that the letters (a), (b), (c), (d), and (e) appearing in the equations, figures, and tables below respectively correspond to the four cases (a), (b), (c), (d), and (e) presented here.

4.3 NSI Parameters

In case (a) $\sim$ (d), we only have the diagonal NSI: $\varepsilon^{eL}_{\mu\mu}$, ε^{eR}_{ee}, $\varepsilon^{eL}_{\tau\tau}$, and $\varepsilon^{eR}_{\mu\mu}$ separately. Case (e) is a combination of case (a) and case (c). It will have diagonal NSI $\varepsilon^{eL}_{\mu\mu}$ from coupling λ_{123} and $\varepsilon^{eL}_{\tau\tau}$ from coupling λ_{133}, and the combination of λ_{123} and λ_{133} will also give an off-diagonal NSI $\varepsilon^{eL}_{\mu\tau}$. Given that the diagonal NSI parameters in case (e) are identical to those in case (a) or case (c), we can only focus on the newly introduced off-diagonal NSI parameter for case (e).

Fig. 4.1 demonstrates the contributions of neutrino NSI in different cases considered in

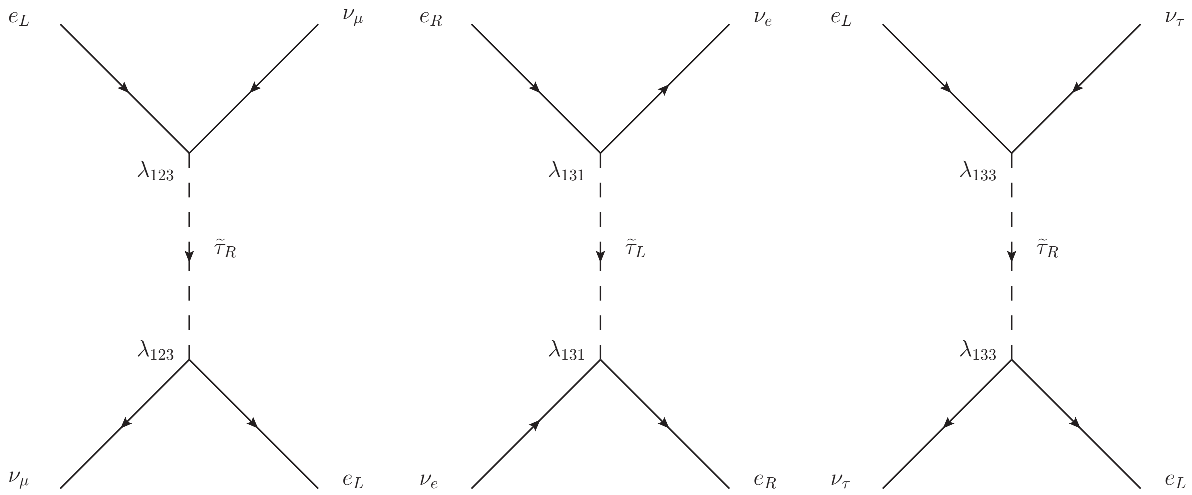

(a) $\lambda_{123} \neq 0$ (b) $\lambda_{131} \neq 0$ (c) $\lambda_{133} \neq 0$

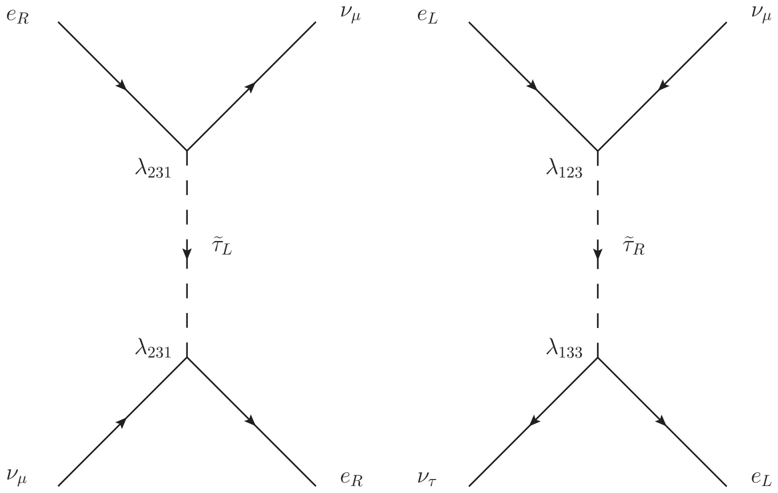

(d) $\lambda_{231} \neq 0$ (e) $\lambda_{123}, \lambda_{133} \neq 0$

Figure 4.1: Tree-level NSI induced by the exchange of charged slepton in the RPV3 framework with the assumption that only the relevant LLE couplings are non-zero.

this article. The effective four-fermion Lagrangians and the NSI parameters are:

$$\mathcal{L}_{\text{eff}}^{\lambda_{123}} = \frac{|\lambda_{123}|^2}{m^2_{\tilde{\tau}_R}}(\overline{e}_L\nu^c_{\mu L})(\overline{\nu}^c_{\mu L}e_L) = \frac{1}{2}\frac{|\lambda_{123}|^2}{m^2_{\tilde{\tau}_R}}(\overline{e}_L\gamma^\mu e_L)(\overline{\nu}_{\mu L}\gamma_\mu\nu_{\mu L}), \tag{4.6a}$$

$$\mathcal{L}_{\text{eff}}^{\lambda_{131}} = \frac{|\lambda_{131}|^2}{m^2_{\tilde{\tau}_L}}(\overline{e}_R\nu_{eL})(\overline{\nu}_{eL}e_R) = -\frac{1}{2}\frac{|\lambda_{131}|^2}{m^2_{\tilde{\tau}_L}}(\overline{e}_R\gamma^\mu e_R)(\overline{\nu}_{eL}\gamma_\mu\nu_{eL}), \tag{4.6b}$$

$$\mathcal{L}_{\text{eff}}^{\lambda_{133}} = \frac{|\lambda_{133}|^2}{m^2_{\tilde{\tau}_R}}(\overline{e}_L\nu^c_{\tau L})(\overline{\nu}^c_{\tau L}e_L) = \frac{1}{2}\frac{|\lambda_{133}|^2}{m^2_{\tilde{\tau}_R}}(\overline{e}_L\gamma^\mu e_L)(\overline{\nu}_{\tau L}\gamma_\mu\nu_{\tau L}), \tag{4.6c}$$

$$\mathcal{L}_{\text{eff}}^{\lambda_{231}} = \frac{|\lambda_{231}|^2}{m^2_{\tilde{\tau}_L}}(\overline{e}_R\nu_{\mu L})(\overline{\nu}_{\mu L}e_R) = -\frac{1}{2}\frac{|\lambda_{231}|^2}{m^2_{\tilde{\tau}_L}}(\overline{e}_R\gamma^\mu e_R)(\overline{\nu}_{\mu L}\gamma_\mu\nu_{\mu L}), \tag{4.6d}$$

$$\mathcal{L}_{\text{eff}}^{\lambda_{123},\lambda_{133}} = \frac{|\lambda_{123}\lambda_{133}|}{m^2_{\tilde{\tau}_R}}(\overline{e}_L\nu^c_{\tau L})(\overline{\nu}^c_{\mu L}e_L) = \frac{1}{2}\frac{|\lambda_{123}\lambda_{133}|}{m^2_{\tilde{\tau}_R}}(\overline{e}_L\gamma^\mu e_L)(\overline{\nu}_{\tau L}\gamma_\mu\nu_{\mu L}), \tag{4.6e}$$

and

$$\varepsilon_{\mu\mu}^{\lambda_{123}} = \varepsilon_{\mu\mu}^{eL,\lambda_{123}} = -\frac{1}{4\sqrt{2}G_F}\frac{|\lambda_{123}|^2}{m^2_{\tilde{\tau}_R}}, \tag{4.7a}$$

$$\varepsilon_{ee}^{\lambda_{131}} = \varepsilon_{ee}^{eR,\lambda_{131}} = \frac{1}{4\sqrt{2}G_F}\frac{|\lambda_{131}|^2}{m^2_{\tilde{\tau}_L}}, \tag{4.7b}$$

$$\varepsilon_{\tau\tau}^{\lambda_{133}} = \varepsilon_{\tau\tau}^{eL,\lambda_{133}} = -\frac{1}{4\sqrt{2}G_F}\frac{|\lambda_{133}|^2}{m^2_{\tilde{\tau}_R}}, \tag{4.7c}$$

$$\varepsilon_{\mu\mu}^{\lambda_{231}} = \varepsilon_{\mu\mu}^{eR,\lambda_{231}} = \frac{1}{4\sqrt{2}G_F}\frac{|\lambda_{231}|^2}{m^2_{\tilde{\tau}_L}}, \tag{4.7d}$$

$$\varepsilon_{\mu\tau}^{\lambda_{123},\lambda_{133}} = \varepsilon_{\mu\tau}^{eL,\lambda_{123},\lambda_{133}} = -\frac{1}{4\sqrt{2}G_F}\frac{|\lambda_{123}\lambda_{133}|}{m^2_{\tilde{\tau}_R}}. \tag{4.7e}$$

Here, it is evident that within the RPV3 framework, the $\tilde{\tau}_R$ with coupling(s) $\lambda_{1\alpha 3}$ will give rise to a negative NSI ε^{eL}, while $\tilde{\tau}_L$ with coupling(s) $\lambda_{\alpha 31}$ will give rise to a positive NSI ε^{eR}. Given the fact that $2|\lambda_{123}\lambda_{133}| \leq |\lambda_{123}|^2 + |\lambda_{133}|^2$, we can infer that for case (e),

$$|\varepsilon_{\mu\tau}^{\lambda_{123},\lambda_{133}}| \ \leq \ \frac{1}{2}\left(|\varepsilon_{\mu\mu}^{\lambda_{123}}| + |\varepsilon_{\tau\tau}^{\lambda_{133}}|\right). \tag{4.8e}$$

This implies that in case (e), the maximum value of the off-diagonal NSI cannot surpass the average value of the diagonal NSIs in case (a) and case (c). Taking into account the additional constraints in case (e) (which are not present in case (a) and case (c)) like $\tau \to \mu\gamma$ and $\tau \to \mu\nu\nu$, the upper limit of $\varepsilon_{\mu\tau}$ in case (e) might be even smaller (to be discussed in subsequent sections of this study).

4.4 Constraints

Since case (e) is a combination of case (a) and case (c), the constraints that are applicable to case (a) or case (c) also hold true for case (e). In the subsequent discussions, unless specifically stated otherwise, the constraints pertaining to case (a) or case (c) also apply to case (e).

4.4.1 LHC Constraints

The searches on sleptons derived from $2\ell +$ missing energy at LHC [248, 249], which are based on the pair production of sleptons, provide direct constraints on the mass of $m_{\tilde{\tau}}$. However, it is important to note that these constraints are model-dependent. In our study, we recast the 95% CL limits obtained from the "SR-SF-0J" region (the signal region with same-flavor lepton pair events and zero non-b-tagged jets) of Ref. [248] for our cases. Under the assumption of $m_{\tilde{\tau}_R}, m_{\tilde{\tau}_L} \ll m_{\tilde{\chi}_1^0}$, we find a lower limit of $m_{\tilde{\tau}} \gtrsim 350 - 550$ GeV at 95% CL at the 13 TeV LHC with a luminosity of 139 fb^{-1}, contingent upon various cases. This limit is smaller than the ones (600 $\sim$ 700 GeV) derived in Ref. [248, 249] because, in our RPV3 scenario, the first two generations are decoupled and do not contribute to the signals. However, in our considered cases, the lower limit on the stau mass is still on the order of sub-TeV. The LHC constraints are depicted by the encompassing black-shaded regions in Fig. 4.8.

4.4.2 LEP Contact Interaction

When the center-of-mass energy larger than the the Z-boson mass in lepton colliders, there are some stringent constraints on contact interactions involving e^+e^- and a pair of fermions [250]. The effective Lagrangian that parametrize the contact interaction for the process $e^+e^- \to f\bar{f}$ can be written as [251]

$$\mathcal{L}_{\text{eff}} = \frac{g^2}{\Lambda^2\left(1+\delta_{ef}\right)} \sum_{i,j=L,R} \eta^f_{ij} \left(\bar{e}_i \gamma^\mu e_i\right)\left(\bar{f}_j \gamma_\mu f_j\right), \tag{4.9}$$

where δ_{ef} is the Kronecker delta function, g is the coupling strength, Λ is the new physics scale and $\eta^f_{ij} = \pm 1$ or 0 depending on the chirality structure. LEP has put 95% confidence level (CL) lower limits on the scale of the contact interaction Λ assuming the coupling $g = \sqrt{4\pi}$ [250]. In RPV3 model, the exchange of the third generation sfermions: $\tilde{\nu}_\tau$ or $\tilde{t}_L$ will affect the process $e^+e^- \to f\bar{f}'$, where $f\bar{f}'$ could be $d_i\bar{d}_j$ or $\ell_i\bar{\ell}_j$ (with $i,j = 1,2,3$). Particularly, we have processes $e^+e^- \to e^+e^-$, $e^+e^- \to \tau^+\tau^-$ and $e^+e^- \to \mu^+\mu^-$ for our case (b), (c) and (d) separately (see Fig. 4.2). We do not have process of this type in case (a) due to the lack of $\tilde{\nu}_\tau$ interaction term.

Applying the Fierz transformation, the effective Lagrangian in case (b), (c) and (d) can be written as

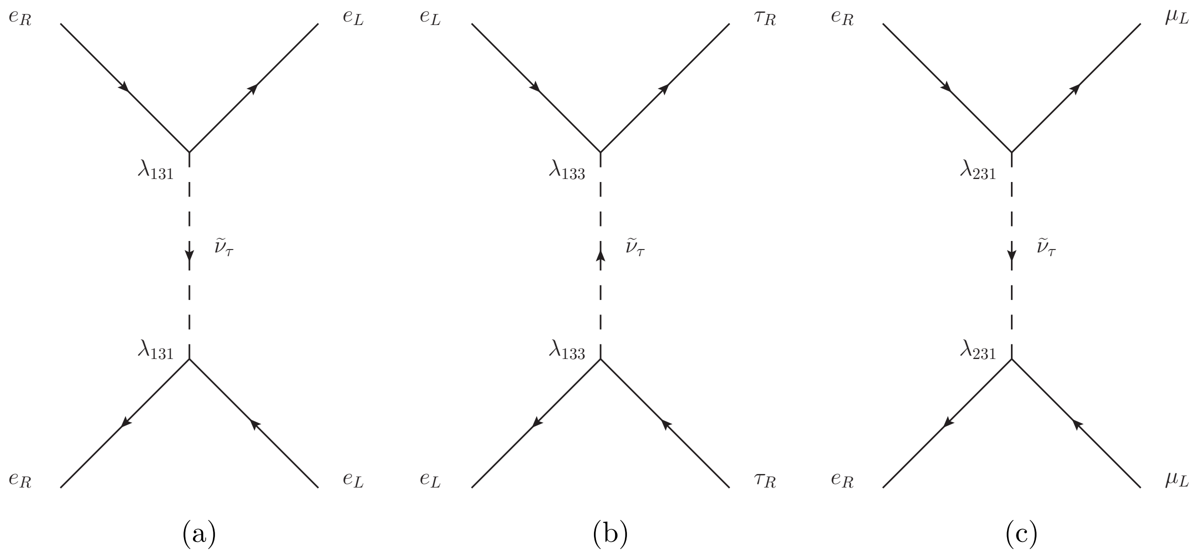

Figure 4.2: Feynman diagrams for $e^+e^- \to f\bar{f}'$ at LEP in the RPV3 framework with the assumption that only the relevant LLE couplings are non-zero.

$$\mathcal{L}^{\lambda_{131}}_{e^+e^-\to e^+e^-} = -\frac{|\lambda_{131}|^2}{2m^2_{\tilde{\nu}_\tau}}(\bar{e}_L\gamma^\mu e_L)(\bar{e}_R\gamma_\mu e_R), \tag{4.10b}$$

$$\mathcal{L}^{\lambda_{133}}_{e^+e^-\to \tau^+\tau^-} = -\frac{|\lambda_{133}|^2}{2m^2_{\tilde{\nu}_\tau}}(\bar{e}_L\gamma^\mu e_L)(\bar{\tau}_R\gamma_\mu \tau_R), \tag{4.10c}$$

$$\mathcal{L}^{\lambda_{231}}_{e^+e^-\to \mu^+\mu^-} = -\frac{|\lambda_{231}|^2}{2m^2_{\tilde{\nu}_\tau}}(\bar{e}_R\gamma^\mu e_R)(\bar{\mu}_L\gamma_\mu \mu_L). \tag{4.10d}$$

Comparing with Eq. (4.9), we obtain

$$\frac{m_{\tilde{\nu}_\tau}}{|\lambda_{131}|} = \frac{\Lambda^-_{LR/RL}(e^+e^- \to e^+e^-)}{\sqrt{2}g}, \tag{4.11b}$$

$$\frac{m_{\tilde{\nu}_\tau}}{|\lambda_{133}|} = \frac{\Lambda^-_{LR/RL}(e^+e^- \to \tau^+\tau^-)}{\sqrt{2}g}, \tag{4.11c}$$

$$\frac{m_{\tilde{\nu}_\tau}}{|\lambda_{231}|} = \frac{\Lambda^-_{LR/RL}(e^+e^- \to \mu^+\mu^-)}{\sqrt{2}g}, \tag{4.11d}$$

where Λ^- corresponds to Λ with $\eta^\ell_{LR} = \eta^\ell_{RL} = -1$. The LEP constraints on Λ with $g = \sqrt{4\pi}$ have been given in [250]. Comparing with Eq. (4.11), we translate those constraints into the lower bounds on $m_{\tilde{\nu}_\tau}/|\lambda|$ in our case (b), (c) and (d) as shown in Table 4.2.

Table 4.2: Bounds on the ratio of $m_{\tilde{\nu}_\tau}$ and corresponding λ couplings from the LEP contact interaction constraints.

	Process	LEP bound [250]	Bound
Case (b)	$e^+e^- \to e^+e^-$	$\Lambda^-_{LR/RL} > 10$ TeV	$\frac{m_{\tilde{\nu}_\tau}}{\lvert\lambda_{131}\rvert} > 1.99$ TeV
Case (c)	$e^+e^- \to \tau^+\tau^-$	$\Lambda^-_{LR/RL} > 2.2$ TeV	$\frac{m_{\tilde{\nu}_\tau}}{\lvert\lambda_{133}\rvert} > 0.44$ TeV
Case (d)	$e^+e^- \to \mu^+\mu^-$	$\Lambda^-_{LR/RL} > 7.9$ TeV	$\frac{m_{\tilde{\nu}_\tau}}{\lvert\lambda_{231}\rvert} > 1.58$ TeV

It should be noted that within the RPV3 framework, the values of the NSI parameters are influenced by the mass of $\tilde{\tau}_R$ or $\tilde{\tau}_L$. However, the constraints imposed by LEP contact interactions establish limits on the mass of $\tilde{\nu}_\tau$. In Fig. 4.8, we have employed various illustrative values of the $m_{\tilde{\nu}_\tau}$ in different cases to elucidate its impact on NSI parameters across different sneutrino masses. The blue dashed lines represent the LEP constraints, which are presented without a shaded region because these constraints in Fig. 4.8 are contingent upon the sneutrino mass and can be circumvented by assuming a sufficiently large value for $m_{\tilde{\nu}_\tau}$.

4.4.3 $\ell_\alpha \to \ell_\beta \nu\bar{\nu}$

Considering only the *LLE* interactions in RPV3, it is still possible to have extra decay modes for τ and μ, where the mediator is right stau. These new decay modes can affect the τ and μ lifetime as well as the universality in τ decays, and will finally give constraints on the neutrino NSI. As shown in Fig. 4.3, in our case (a), case (c), and case (e), there are three extra contributions for $\mu \to e\nu\bar{\nu}$, $\tau \to e\nu\bar{\nu}$ and $\tau \to \mu\nu\bar{\nu}$.

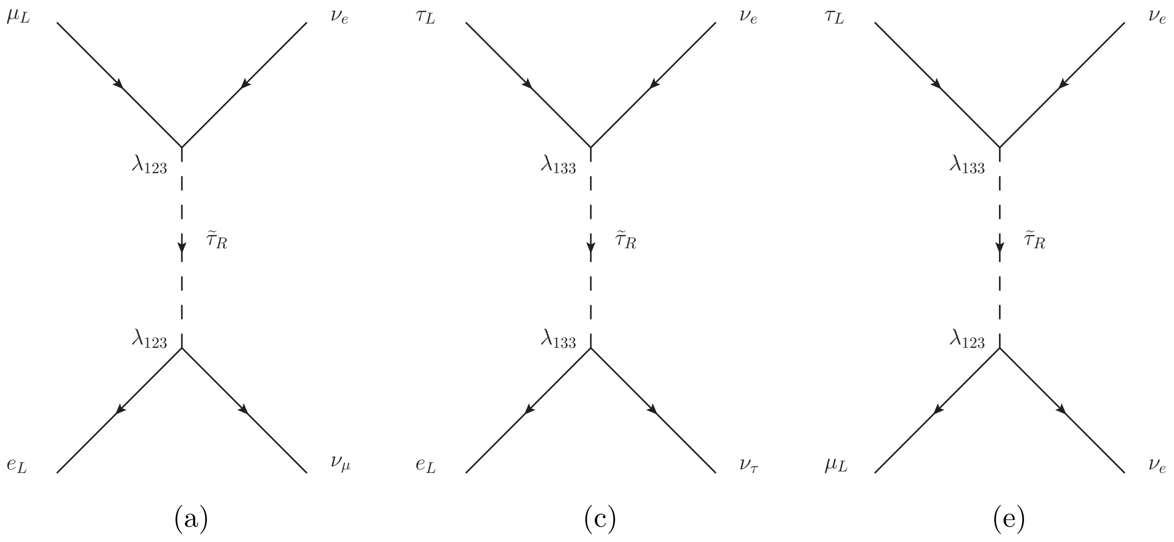

Figure 4.3: Feynman diagrams for the decay modes of $\mu \to e\nu\bar{\nu}$, $\tau \to e\nu\bar{\nu}$, and $\tau \to \mu\nu\bar{\nu}$ mediated by $\tilde{\tau}_R$ in RPV3 framework.

The effective μ and τ decay four-fermion Lagrangians in our case (a), case (c), and case (e) are given by

$$\mathcal{L}^{\lambda_{123}}_{\mu\to e\nu\bar{\nu}} = -\frac{|\lambda_{123}|^2}{m^2_{\tilde{\tau}_R}}(\overline{\nu}^c_{eL}\mu_L)(\overline{e}_L\nu^c_{\mu L}) = -\frac{|\lambda_{123}|^2}{2m^2_{\tilde{\tau}_R}}(\overline{e}_L\gamma^\mu\nu_{eL})(\overline{\nu}_{\mu L}\gamma_\mu\mu_L), \tag{4.12a}$$

$$\mathcal{L}^{\lambda_{133}}_{\tau\to e\nu\bar{\nu}} = -\frac{|\lambda_{133}|^2}{m^2_{\tilde{\tau}_R}}(\overline{\nu}^c_{eL}\tau_L)(\overline{e}_L\nu^c_{\tau L}) = -\frac{|\lambda_{133}|^2}{2m^2_{\tilde{\tau}_R}}(\overline{e}_L\gamma^\mu\nu_{eL})(\overline{\nu}_{\tau L}\gamma_\mu\tau_L), \tag{4.12c}$$

$$\mathcal{L}^{\lambda_{123},\lambda_{133}}_{\tau\to \mu\nu\bar{\nu}} = -\frac{|\lambda_{123}\lambda_{133}|}{m^2_{\tilde{\tau}_R}}(\overline{\nu}^c_{eL}\tau_L)(\overline{\mu}_L\nu^c_{eL}) = -\frac{|\lambda_{123}\lambda_{133}|}{2m^2_{\tilde{\tau}_R}}(\overline{\mu}_L\gamma^\mu\nu_{eL})(\overline{\nu}_{eL}\gamma_\mu\tau_L), \tag{4.12e}$$

where we have used the Fierz transformation in the second steps.

Comparing with the SM μ and τ decay Lagrangians

$$\mathcal{L}^{\rm SM}_{\mu\to e\nu\bar{\nu}} = -2\sqrt{2}G_F(\overline{e}_L\gamma^\mu\nu_{eL})(\overline{\nu}_{\mu L}\gamma_\mu\mu_L), \tag{4.13a}$$

$$\mathcal{L}^{\rm SM}_{\tau\to e\nu\bar{\nu}} = -2\sqrt{2}G_F(\overline{e}_L\gamma^\mu\nu_{eL})(\overline{\nu}_{\tau L}\gamma_\mu\tau_L), \tag{4.13c}$$

$$\mathcal{L}^{\rm SM}_{\tau\to \mu\nu\bar{\nu}} = -2\sqrt{2}G_F(\overline{\mu}_L\gamma^\mu\nu_{\mu L})(\overline{\nu}_{\tau L}\gamma_\mu\tau_L), \tag{4.13e}$$

for case (a), case (c), and case (e), the coupling g^V_{LL} in the general four-fermion Lagrangian form [216, 53] gets additional contribution δg^V_{LL}:

$$\delta g^V_{LL}(\mu \to e\nu\bar{\nu}) = \frac{1}{4\sqrt{2}G_F}\frac{|\lambda_{123}|^2}{m^2_{\tilde{\tau}_R}} = -\varepsilon^{\lambda_{123}}_{\mu\mu}, \tag{4.14a}$$

$$\delta g^V_{LL}(\tau \to e\nu\bar{\nu}) = \frac{1}{4\sqrt{2}G_F}\frac{|\lambda_{133}|^2}{m^2_{\tilde{\tau}_R}} = -\varepsilon^{\lambda_{133}}_{\tau\tau}, \tag{4.14c}$$

$$\delta g^V_{LL}(\tau \to \mu\nu\bar{\nu}) = \frac{1}{4\sqrt{2}G_F}\frac{|\lambda_{123}\lambda_{133}|}{m^2_{\tilde{\tau}_R}} = -\varepsilon^{\lambda_{123},\lambda_{133}}_{\mu\tau}. \tag{4.14e}$$

However, this change can only affect the g^V_{LL}-type coupling, and because of the normalization condition of the couplings [216, 53], our scenarios do not influence the Michel parameters. But case (c) still has a strong constraint from $e-\mu$ universality in τ decays. The SM prediction including mass effects gives $\Gamma(\tau \to \mu\nu\bar{\nu})/\Gamma(\tau \to e\nu\bar{\nu}) = 97.26\%$ [252] while the experiment prefers a slightly larger central value $\Gamma(\tau \to \mu\nu\bar{\nu})/\Gamma(\tau \to e\nu\bar{\nu}) = (97.62 \pm 0.28)\%$ [252]. In our case (c) the width $\Gamma(\tau \to e\nu\bar{\nu})$ is modified to $(1 + \delta g^V_{LL}(\tau \to e\nu\bar{\nu}))^2\ \Gamma^{\rm SM}(\tau \to e\nu\bar{\nu})$. Allowing for 3σ error, the $e-\mu$ universality in τ decays gives

$$|\varepsilon^{\lambda_{133}}_{\tau\tau}| \leq 0.25\%. \tag{4.15c}$$

Similarly, case (a) would get a strong constraint from the comparison of the decays $\tau \to \mu\nu\bar{\nu}$ and $\mu \to e\nu\bar{\nu}$ [217], which is described by the observable

$$R_{\tau/\mu} \equiv \frac{{\rm BR}(\tau \to \mu\nu\bar{\nu})_{\rm exp}/{\rm BR}(\tau \to \mu\nu\bar{\nu})_{\rm SM}}{{\rm BR}(\mu \to e\nu\bar{\nu})_{\rm exp}/{\rm BR}(\mu \to e\nu\bar{\nu})_{\rm SM}}. \tag{4.16}$$

The current measurement yields a value of $R_{\tau/\mu} = 1.0022 \pm 0.0030$ [131]. Following a similar derivation as that of Eq. (4.15), and taking 3σ uncertainties in the measured value, it converts to

$$|\varepsilon_{\mu\mu}^{\lambda_{123}}| \;\leq\; 0.56\%. \tag{4.17a}$$

Here, it is important to note that, different from the Zee model where there is no interference with the SM [253] due to the chirality of the charged leptons in the decay process, the change of the widths of μ and τ is of order δg_{LL}^{V} not $|\delta g_{LL}^{V}|^2$ in our RPV3 case (a) and case (c). For case (e), there is also no interference with the SM in the decay process $\tau \to \mu\nu\bar{\nu}$ due to the type of neutrinos involved.

Furthermore, it should be emphasized that the constraints described in Eq. (4.15) for case (c) and in Eq. (4.17) for case (a) do not apply to case (e), unlike the constraints in the other subsections. For case (e), not only the widths $\Gamma(\tau \to e\nu\bar{\nu})$ and $\Gamma(\mu \to e\nu\bar{\nu})$ are changed, but also the width $\Gamma(\tau \to \mu\nu\bar{\nu})$ is changed to $(1 + \delta g_{LL}^{V}(\tau \to \mu\nu\bar{\nu})^2)\ \Gamma^{\mathrm{SM}}(\tau \to \mu\nu\bar{\nu})$. Allowing for 3σ error, for case (e), the $e - \mu$ universality in τ decays gives

$$|\varepsilon_{\mu\tau}^{\lambda_{123},\lambda_{133}}| \;\leq\; \sqrt{1.0123 \times (1 - \varepsilon_{\tau\tau}^{\lambda_{133}})^2 - 1}, \tag{4.18e}$$

and $R_{\tau/\mu}$ gives

$$|\varepsilon_{\mu\tau}^{\lambda_{123},\lambda_{133}}| \;\leq\; \sqrt{1.0112 \times (1 - \varepsilon_{\mu\mu}^{\lambda_{123}})^2 - 1}. \tag{4.19e}$$

Based on our assumptions in this chapter, $\varepsilon_{\tau\tau}^{\lambda_{133}}$ and $\varepsilon_{\mu\mu}^{\lambda_{123}}$ are both non-positive definite; see Eq. (4.7a) and Eq. (4.7c). Thus, Eq. (4.18) and Eq. (4.19) result in two relatively lax constraints on $\varepsilon_{\mu\tau}^{\lambda_{123},\lambda_{133}}$:

$$|\varepsilon_{\mu\tau}^{\lambda_{123},\lambda_{133}}| \;\leq\; 11.1\%, \tag{4.20e}$$

from $e-\mu$ universality, and

$$|\varepsilon_{\mu\tau}^{\lambda_{123},\lambda_{133}}| \;\leq\; 10.6\%, \tag{4.21e}$$

from $R_{\tau/\mu}$. These relatively loose constraints are not surprising, as they arise from the ratio of two decay processes, and case (e) happens to enhance both of them, although the enhancement is not of the same order of magnitude for the two processes. In Fig. 4.8, the constraints imposed by $R_{\tau/\mu}$ are visually represented by the regions shaded in orange, while the constraints stemming from $e-\mu$ universality are illustrated by the yellow-shaded regions.

4.4.4 $\tau \to \mu\gamma$

Fig. 4.3(e) of case (e) is closely related to the LFV loop decays of $\tau \to \mu\gamma$, whereas this situation does not apply to case (a) and case (c) because the flavors of the neutrinos are different in Figs. 4.3(a) and (c).

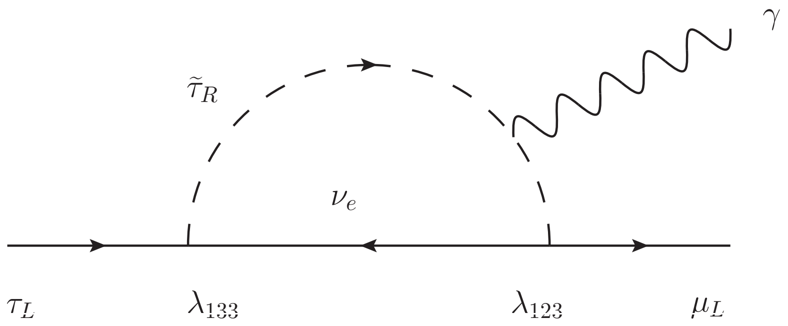

(a)

Figure 4.4: Relevant Feynman diagram for the LFV process $\tau \to \mu\gamma$ in RPV3.

The general contribution of RPV3 to $\tau \to \mu\gamma$ is provided in Ref. [80]. Specifically for our case (e),

$$\Gamma(\tau \to \mu\gamma) \simeq \frac{\alpha m_\tau^5 G_F^2}{256\pi^4}\frac{m_W^4}{g^4}\left|\frac{\lambda_{123}\lambda_{133}}{3m_{\tilde{\tau}_R}^2}\right|^2 = \frac{\alpha m_\tau^5 G_F^4}{72\pi^4}\frac{m_W^4}{g^4}\varepsilon_{\mu\tau}^2, \tag{4.22e}$$

where α and g are the electromagnetic and weak coupling constants separately. Applying the current experimental data from Belle collaboration where $\mathrm{BR}(\tau \to \mu\gamma) < 4.2 \times 10^{-8}$ [57], Eq. (4.22) converts to a constraint of

$$|\varepsilon_{\mu\tau}^{\lambda_{123},\lambda_{133}}| \;\leq\; 3.57\%. \tag{4.23e}$$

The constraint imposed by $\tau \to \mu\gamma$ is visually demonstrated as a region shaded in red in Fig. 4.8.

4.4.5 Neutrino Mass

The trilinear *LLE* couplings in Eq. (4.5) can contribute to neutrino masses in RPV3 framework at one-loop level through the lepton-slepton loops as shown in Fig. 4.5. From general expression [190, 191, 117] and focusing on the third generation sfermions [80], the neutrino mass matrix can be simplified as

$$M_{ij}^\nu \simeq \frac{1}{8\pi^2}\left(\frac{A^\tau - \mu\tan\beta}{\overline{m}_{\tilde{\tau}}^2}\right)\sum_k \lambda_{ik3}\lambda_{j3k} m_{e_k} m_\tau, \tag{4.24}$$

where $\overline{m}_{\tilde{\tau}}$ is the average stau mass and we have assumed that the A-terms [117] are proportional to the Yukawa couplings in the basis where the charged lepton masses are diagonal.

Within the framework of our analysis, only λ_{133} contributes to Eq. (4.24). Applying the cosmological bound $\sum_i m_{\nu_i} \lesssim 0.1$ eV [192], we find that only for case (c) and case (e),

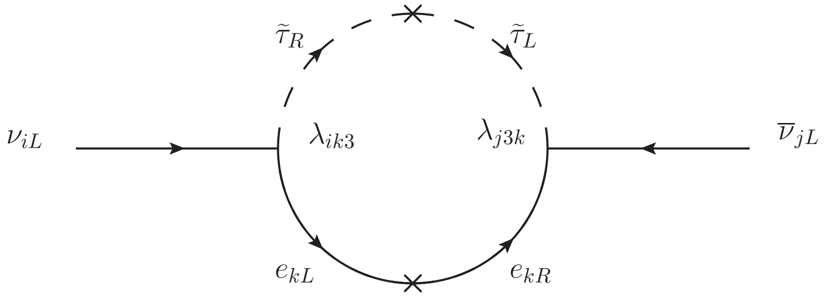

Figure 4.5: Contribution to neutrino mass from RPV3 at one-loop level.

$$A^\tau - \mu \tan\beta \lesssim \mathcal{O}(2.5 \text{ MeV}), \tag{4.25c}$$

where we have assumed a typical value of $\lambda_{133}/\overline{m}_{\tilde{\tau}} \simeq 1/(1000 \text{ GeV})$. Here, it is important to mention that the other three cases do not contribute to Eq. (4.24) and thus do not have constraints from neutrino mass.

4.4.6 Monophoton Process

In RPV3, neutrino NSI with electrons are directly related to new contributions of the monophoton process $e^+e^- \to \nu\bar{\nu}\gamma$. The diagrams resemble Fig. 4.1, where a photon is emitted from either an electron leg or the intermediate charged slepton. The SM monophoton process occurs via s-channel Z-boson exchange or t-channel W-boson exchange with a photon emitted from an electron (positron) leg or the intermediate W-boson. And thus, a constraint from LEP data can be derived [254].

In our case (a), case (c), case (d), and case (e), the final-state neutrinos changed flavors; in our case (b) and case (d), the initial electrons are right-handed. These characteristics ensure that the new RPV3 contributions do not interfere with the SM W-mediated process. Moreover, since the Z-mediated process is an s-channel process with the distribution of the recoil mass to the photon system peak around the Z mass, the interference contribution is also negligible.

The total cross-section for the monophoton process can be written as $\sigma = \sigma_{\text{SM}} + \sigma_{\text{NS}}$, where σ_{SM} is the SM cross section and σ_{NS} stands for the pure non-standard contribution and its possible interference with the SM contribution. The total cross section should satisfy the constraint $|\sigma - \sigma_{\text{exp}}| \leq \delta\sigma_{\text{exp}}$, where $\sigma_{\text{exp}} \pm \delta\sigma_{\text{exp}}$ is the experimental result.

Different from the Zee model [253] where the mass of the light charged scalar is assumed around $100 \sim 500$ GeV and the mass of the heavy charged scalar is bounded by the LEP contact interaction, the mediators of the monophoton process in our scenarios are the charged sleptons with a mass typically $\gtrsim \mathcal{O}(1\text{ TeV})$. With such a heavy mass, assuming the coupling to be $\sim \mathcal{O}(1)$, we have found that the RPV3 contributions are about 2 order of magnitude smaller than the L3 experimental error [255, 256]. To be specific, when the center of mass energy $\sqrt{s} = 200$ GeV, the mass of the charged slepton $m_{\tilde{\tau}} = 1$ TeV and the corresponding coupling $\lambda = 1$, the σ_{NS} is only $2\% \sim 6\%$ of the $\delta\sigma_{\text{exp}}$ in our four cases which means that the monophoton process is too weak to set a bound on the mass of the charged slepton and the corresponding couplings in our cases and cannot be shown in the range of our Fig. 4.8.

4.4.7 Direct Experimental Searches

There are some current model independent experimental constraints from neutrino experiments such as IceCube [257], CHARM II [258], TEXONO [259], BOREXINO [260], MINOS [261], and KamLAND [262, 263, 243] as well as the global-fit [264]. In the global fit analysis, the constraint $-2\% \leq \varepsilon^e_{\mu\tau} \leq 1.2\%$ applies to case (e); the constraint $-1.5\% \leq \varepsilon^e_{\tau\tau} - \varepsilon^e_{\mu\mu} \leq 4.8\%$ becomes $\varepsilon^e_{\mu\mu} \geq -4.8\%$ for case (a), $\varepsilon^e_{\tau\tau} \geq -1.5\%$ for case (c), and $\varepsilon^e_{\mu\mu} \leq 1.5\%$ for case (d). However, for case (e), the constraint from $\varepsilon^e_{\tau\tau} - \varepsilon^e_{\mu\mu}$ could be completely circumvented from the cancellation of $\varepsilon^e_{\mu\mu}$ and $\varepsilon^e_{\tau\tau}$ as long as $|\lambda_{123}| = |\lambda_{133}|$. But the simultaneous non-zero values of λ_{123} and λ_{133} are still constrained by the processes $\tau \to \mu\nu\bar{\nu}$ and $\tau \to \mu\gamma$ in case (e), and prevent $\varepsilon^e_{\mu\tau}$ to be large. Different from the Zee model [253] where the cancellation cannot be realized, because the large $\varepsilon_{\mu\mu}$ and $\varepsilon_{\tau\tau}$ means a large $\varepsilon_{\mu\tau}$ which is severely constrained by $\tau \to ee\mu$, this cancellation could be realized in general RPV3 scenarios because of the diversity of the RPV parameters. In our Fig. 4.8, we have also included the future 2σ sensitivity at DUNE with an exposure of 336 kt.MW.yr [265, 266]. In case (a) and case (c), $\varepsilon^{eL}_{\alpha\beta}$ gives the total NSI; in case (b) and case (d), $\varepsilon^{eR}_{\alpha\beta}$ gives the total NSI, so for the neutrino experiments, we only take the most relevant constraint for each case. For the constraint of $\varepsilon^{eR}_{\mu\mu}$ in CHARM II [258], we have used the updated value $-1.7\% < \varepsilon^{eR}_{\mu\mu} < 3.8\%$ [253] where the latest value of s^2_w is used to obtain the constraint.

In Fig. 4.8, the constraints derived from IceCube are portrayed by a region shaded in brown. The constraints obtained from CHARM II are represented by magenta-shaded regions. The constraints inferred from TEXONO are showcased by purple-shaded regions. The constraints deduced from BOREXINO are illustrated through green-shaded regions. The constraints derived from MINOS are presented by pink-shaded regions. The constraints arising from KamLAND are depicted by cyan-shaded regions. The global fit constraints are visualized by violet-shaded regions. Additionally, the future sensitivities at DUNE are indicated by gray dashed lines.

4.4.8 Anomalous Magnetic Moment of the Electron and Muon

The contributions to $(g-2)_e$ and $(g-2)_\mu$ from the RPV3 framework can originate from both λ and λ' couplings [140]. As shown in Fig. 4.6, in our specific RPV3 cases, the contributions to $(g-2)_e$ can be described as follows:

$$\Delta a_e^{\lambda_{123}} = \frac{m_e^2}{96\pi^2}\left(-\frac{|\lambda_{123}|^2}{m_{\tilde{\tau}_R}^2}\right), \tag{4.26a}$$

$$\Delta a_e^{\lambda_{131}} = \frac{m_e^2}{96\pi^2}\left(-\frac{|\lambda_{131}|^2}{m_{\tilde{\tau}_L}^2} + \frac{4|\lambda_{131}|^2}{m_{\tilde{\nu}_\tau}^2}\right), \tag{4.26b}$$

$$\Delta a_e^{\lambda_{133}} = \frac{m_e^2}{96\pi^2}\left(-\frac{|\lambda_{133}|^2}{m_{\tilde{\tau}_R}^2} + \frac{2|\lambda_{133}|^2}{m_{\tilde{\nu}_\tau}^2}\right), \tag{4.26c}$$

$$\Delta a_e^{\lambda_{231}} = \frac{m_e^2}{96\pi^2}\left(-\frac{|\lambda_{231}|^2}{m_{\tilde{\tau}_L}^2} + \frac{2|\lambda_{231}|^2}{m_{\tilde{\nu}_\tau}^2}\right). \tag{4.26d}$$

Similarly, as shown in Fig. 4.7, in our specific RPV3 cases, the contributions to $(g-2)_\mu$ can be described as follows:

$$\Delta a_\mu^{\lambda_{123}} = \frac{m_\mu^2}{96\pi^2}\left(-\frac{|\lambda_{123}|^2}{m_{\tilde{\tau}_R}^2}\right), \tag{4.27a}$$

$$\Delta a_\mu^{\lambda_{231}} = \frac{m_\mu^2}{96\pi^2}\left(\frac{2|\lambda_{231}|^2}{m_{\tilde{\nu}_\tau}^2}\right). \tag{4.27d}$$

It should be noted that only λ_{123} (corresponding to case (a) and thus, case (e)) and λ_{231} (corresponding to case (d)) can yield contributions to $(g-2)_\mu$ in this context.

Based on the discussions in the previous subsections, it is evident that the typical limits on the neutrino NSI parameters are, at most, a few percentage points. Even though the $m_{\tilde{\nu}_\tau}$, which is irrelevant to NSI, can contribute to the electron and muon $(g-2)$ in certain cases, we can still directly evaluate the contribution of $(g-2)$ from staus, which is essentially equivalent to considering the contribution from NSI parameters in this context. Specifically, the first terms in Eq. (4.26) and Eq. (4.27a) indicate that

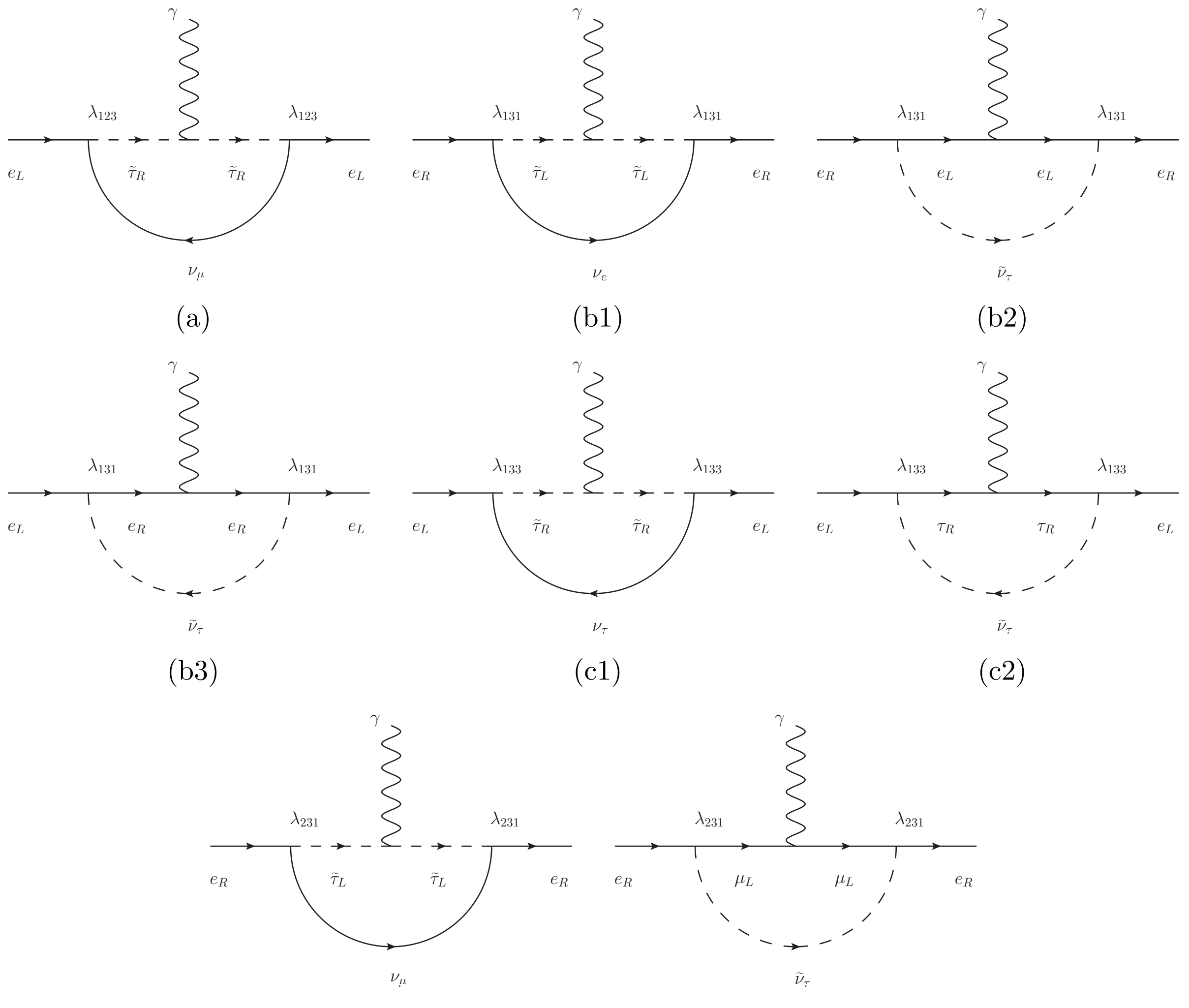

(a) (b1) (b2)

(b3) (c1) (c2)

(d1) (d2)

Figure 4.6: Relevant contribution to the $(g-2)_e$ from λ couplings in RPV3.

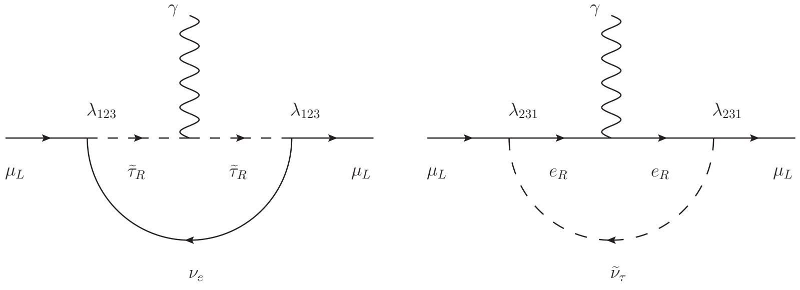

(a) (d)

Figure 4.7: Relevant contribution to the $(g-2)_\mu$ from λ couplings in RPV3.

$$\Delta a_e \;=\; -\frac{m_e^2 G_F}{12\sqrt{2}\pi^2}|\varepsilon|, \tag{4.28}$$

$$\Delta a_\mu \;=\; -\frac{m_\mu^2 G_F}{12\sqrt{2}\pi^2}|\varepsilon|, \tag{4.29}$$

where the ε stands for the NSI parameter in each relevant case. To begin with, Eq. (4.28) and Eq. (4.29) indicate that the contributions of staus (and thus, NSI parameters in this context) to electron and muon $(g-2)$ are negative. Additionally, assuming a sizable value of the NSI parameter $|\varepsilon| = 5\%$, and substituting typical values for m_e, m_μ, and Fermi constant, we obtain $\Delta a_e \approx -1 \times 10^{-15}$ and $\Delta a_\mu \approx -4 \times 10^{-11}$. These values are considerably small in comparison to the current experimental measurements: $\Delta a_e^{\mathrm{Cs}} = (-8.7 \pm 3.6) \times 10^{-13}$ [267] based on Cs measurement, $\Delta a_e^{\mathrm{Rb}} = (4.8 \pm 3.0) \times 10^{-13}$ [268] based on Rb measurement, and $\Delta a_\mu = (251 \pm 59) \times 10^{-11}$ from the Fermilab muon $(g-2)$ experiment [33]. Specifically, the contribution from Eq. (4.28) is at most $\sim 0.2\%$ of the central value of Δa_e and $\sim 0.3\%$ of the 1σ error of Δa_e. The contribution from Eq. (4.29) is at most $\sim 1.6\%$ of the central value[1] of Δa_μ and $\sim 6.7\%$ of the 1σ error of Δa_μ.

On the other hand, the sneutrino contributions in Eq. (4.26) and Eq. (4.27) are also subject to constraints from the LEP contact interaction experiment as shown in Table 4.2. Specifically, in case (b), the $\tilde{\nu}_\tau$ contribution to Δa_e is less than 2.8×10^{-16}; in case (c), the $\tilde{\nu}_\tau$ contribution to Δa_e is less than 2.8×10^{-15}; in case (d), the $\tilde{\nu}_\tau$ contribution is less than 2.2×10^{-16} for Δa_e and less than 9.4×10^{-12} for Δa_μ. These values are only at the order of $0.01\% \sim 0.1\%$ of the corresponding central values of Δa_e and Δa_μ.

As a result, the scale of the $(g-2)_e$ and $(g-2)_\mu$ sensitive regions in the $(m_{\tilde{\tau}}, \lambda)$ parameter space are significantly larger in scale compared to the NSI sensitive regions in the RPV3

---

[1] The lattice simulation result from the BMW collaboration [34] increases the leading hadronic contribution of a_μ^{SM} with a relatively larger uncertainty. This would result in a smaller central value of $\Delta a_\mu = 107 \times 10^{-11}$, but the magnitude is of the same order as the central value of $\Delta a_\mu = 251 \times 10^{-11}$ provided by Ref. [33].

framework. Hence, the constraints from $(g-2)_e$ and $(g-2)_\mu$ are not depicted in Fig. 4.8. Besides, this feature reinforces the notion [246, 62] that the primary source of the significant deviation in $(g-2)_\mu$ does not originate from the stau contribution, but rather from the sneutrino contribution within the framework of RPV3. In Ref. [246, 62], the constraints from the LEP contact interaction do not apply, as these scenarios are specifically focused on the $\mu\tau$ sector of the λ couplings. Therefore, the future muon collider holds the potential to offer definitive insights into the validity of the muon $(g-2)$ solutions within the RPV3 framework.

4.5 Result

In Fig. 4.8, we showcase the constraints and permissible regions for cases (a), (b), (c), (d), and (e) within the corresponding $(m_{\tilde{\tau}}, \lambda)$ parameter space. The illustrative values of the allowed NSI parameters are represented by black dotted curves. The limitations imposed by the LHC are depicted by encompassing black-shaded regions. The blue dashed lines symbolize the constraints originating from LEP. The limitations derived from $R_{\tau/\mu}$ are visually represented by orange-shaded regions, while the constraints arising from $e-\mu$ universality are illustrated by yellow-shaded regions. The limitations inferred from IceCube are portrayed through a brown-shaded region. The constraints obtained from CHARM II are represented by magenta-shaded regions. The limitations deduced from TEXONO are showcased by purple-shaded regions. The constraints derived from BOREXINO are illustrated by green-shaded regions. The limitations arising from MINOS are presented by pink-shaded regions. The constraints stemming from KamLAND are depicted by cyan-shaded regions. The global fit constraints are visualized through violet-shaded regions. Furthermore, the future sensitivities at DUNE are indicated by gray dashed lines. The horizontal black dashed line represents the perturbativity limit of $\sqrt{4\pi}$.

In RPV3 scenarios, specifically considering only the LLE interactions, our findings indicate that the largest permissible NSI parameters are as follows:

- In case (a) where $\lambda_{123} \neq 0$, the largest allowed NSI parameter is $\varepsilon_{\mu\mu} = -0.56\%$, constrained by the ratio of the processes $\tau \to \mu\nu\nu$ and $\mu \to e\nu\nu$.
- In case (b) where $\lambda_{131} \neq 0$, the largest allowed NSI parameter is $\varepsilon_{ee} = 8\%$, constrained by the TEXONO experiment.
- In case (c) where $\lambda_{133} \neq 0$, the largest allowed NSI parameter is $\varepsilon_{\tau\tau} = -0.25\%$, constrained by the $e - \mu$ universality.
- In case (d) where $\lambda_{231} \neq 0$, the largest allowed NSI parameter is $\varepsilon_{\mu\mu} = 3.8\%$, constrained by global-fit analyses.
- In case (e) where $\lambda_{123}\lambda_{133} \neq 0$, the largest allowed NSI parameter is $\varepsilon_{\mu\tau} = -0.29\%$, constrained by the IceCube experiment.

4.6 Discussions

In our RPV3 scenarios, in case (b) where $\lambda_{131} \neq 0$, and case (d) where $\lambda_{231} \neq 0$, it is the left-handed stau ($\tilde{\tau}_L$) that contributes to a positive ε^{eR}. However, in case (a) where $\lambda 123 \neq 0$, case (c) where $\lambda_{133} \neq 0$, and case (e) where both λ_{123} and $\lambda_{133} \neq 0$, it is the right-handed stau ($\tilde{\tau}_R$) that contributes to a negative ε^{eL}. In case (b) and case (d), the permissible NSI parameters are relatively larger compared to those in case (a), case (c), and case (e). This discrepancy arises due to the presence of various constraints from lepton decays, which restrict the magnitude of the NSI parameters in case (a), case (c), and case (e), preventing them from attaining larger values.

In our case (b) and case (d), where the $\tilde{\tau}_L$ contributes to neutrino NSI, we observe similar results to those obtained in the Zee model [253]. In both cases, ε_{ee} can reach values as high as 8%, and $\varepsilon_{\mu\mu}$ can reach values as high as 3.8%. However, in RPV3 scenarios, we encounter

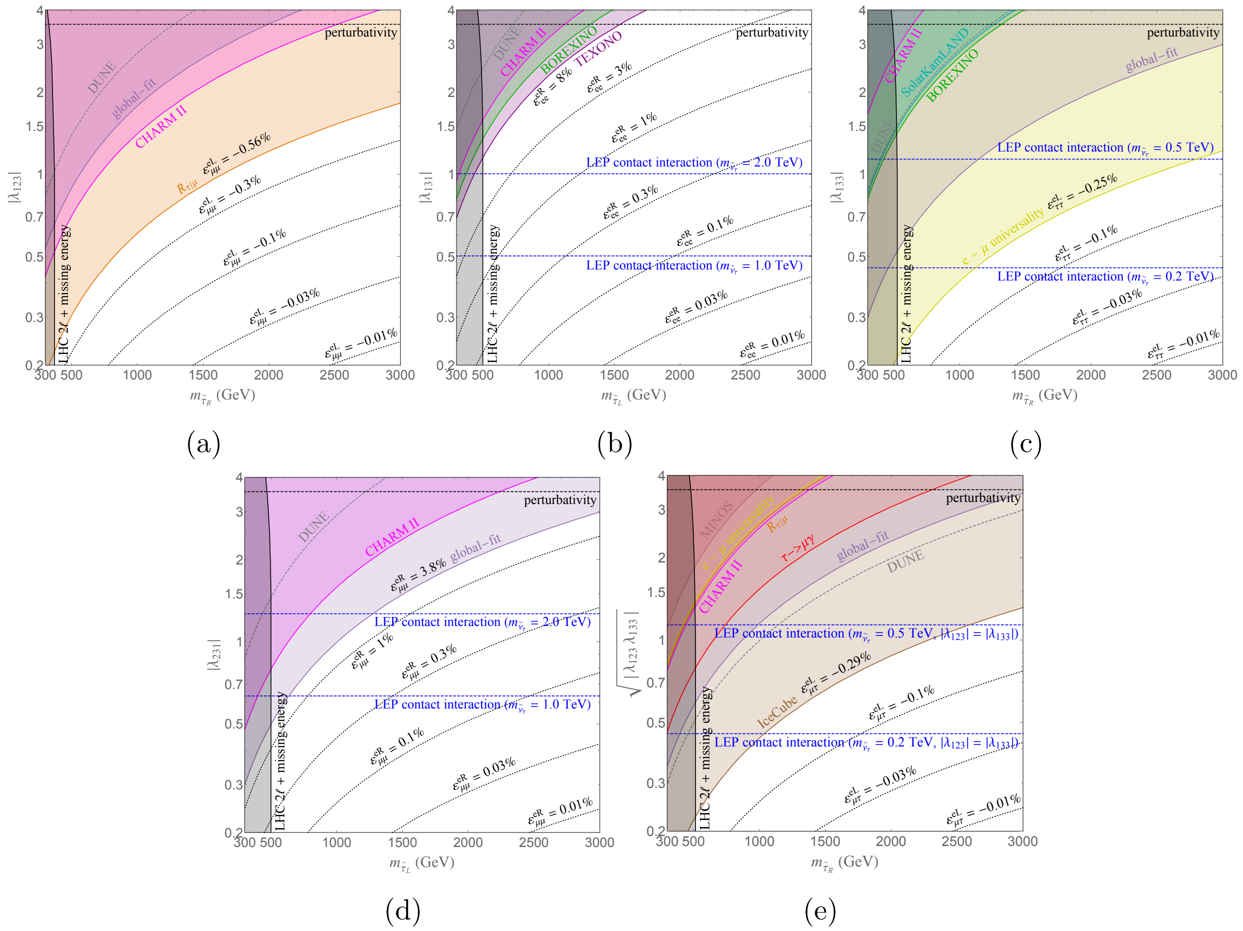

(a) (b) (c)

(d) (e)

Figure 4.8: The constraints and permissible regions for cases (a), (b), (c), (d), and (e) within the corresponding $(m_{\tilde{\tau}}, \lambda)$ parameter space. The allowed NSI parameters are exemplified by black dotted curves. The restrictions imposed by the LHC are depicted by enclosing regions shaded in black. The blue dashed lines symbolize the constraints originating from LEP. The limitations derived from $R_{\tau/\mu}$ are visually represented by regions shaded in orange, while the constraints arising from $e - \mu$ universality are illustrated by regions shaded in yellow. The limitations inferred from IceCube are portrayed by a region shaded in brown. The constraints obtained from CHARM II are represented by regions shaded in magenta. The limitations deduced from TEXONO are showcased by regions shaded in purple. The constraints derived from BOREXINO are illustrated by regions shaded in green. The limitations arising from MINOS are presented by regions shaded in pink. The constraints stemming from KamLAND are depicted by regions shaded in cyan. The global fit constraints are visualized through regions shaded in violet. Furthermore, the future sensitivities at DUNE are indicated by gray dashed lines. The horizontal black dashed line represents the perturbativity limit of $\sqrt{4\pi}$.

limitations when it comes to $\varepsilon_{\tau\tau}$. Although we have $\varepsilon_{\tau\tau}$ contribution from $\tilde{\tau}_R$ in case (c), the value of $\varepsilon_{\tau\tau}$ is strongly constrained by the $e-\mu$ universality and cannot reach the levels of $\varepsilon_{\tau\tau} = 9.3\%$ allowed in the Zee model [253]. This limitation stems from the fact that we cannot utilize $\tilde{\tau}_L$ to contribute to $\varepsilon_{\tau\tau}$ due to the antisymmetric property of the λ_{ijk} couplings, which renders the λ_{331} coupling to be zero.

The difference between the RPV3 LLE interaction terms and the Zee model reveals intriguing differences in their predictions. Both models allow for significant values of ε_{ee} and $\varepsilon_{\mu\mu}$, reaching up to 8% and 3.8%, respectively. However, the scenario concerning $\varepsilon_{\tau\tau}$ in RPV3, is not allowed to be large, due to the constraint of $e-\mu$ universality which limits the contribution from $\tilde{\tau}_R$ or antisymmetric property of the λ_{ijk} couplings which prevent $\varepsilon_{\tau\tau}$ gets contribution from $\tilde{\tau}_L$.

Chapter 5: Neutral and Doubly-Charged Higgs at Future Lepton Colliders

This chapter is based on my work [64].

5.1 Introduction

As we have seen in Chapter 3, the presence of a lepton flavor-violating coupling does not guarantee the occurrence of an LFV signal at colliders. In this chapter, our focus shifts to the neutral and doubly-charged Higgs bosons. We consider both LFV (lepton flavor-changing) and LFC (lepton flavor-conserving) cases and investigate their potential for discovery at future lepton colliders in a model-independent way.

Many new physics scenarios beyond the Standard Model (BSM) necessitate the existence of new neutral and/or charged scalar fields, which might couple to the SM charged leptons (but not hadrons), and thus, can give rise to BSM signals while evading strong constraints mostly coming from the hadronic sector. In this chapter, I will show that future lepton colliders provide a clean environment to probe these leptophilic new scalars via multi-lepton final states, including some interesting lepton flavor-violating channels. I will also show the kinematic distributions of the final state leptons to distinguish the BSM contributions from neutral and doubly-charged scalars giving rise to the same final state, as well as from the irreducible SM background.

The Standard Model of particle physics has been tremendously successful in explaining a wide variety of experimental results and characterizing the fundamental particles and their interactions. However, there are still many unresolved issues that need to extend the SM by introducing new particles and interactions, such as the Higgs sector extension models, which introduce additional scalar fields [269, 270, 271, 272].

The neutral and doubly charged Higgs bosons are hypothetical particles predicted by certain extensions of the SM, such as the Left-Right Symmetric Model (LRSM) [273, 274, 275, 276, 277], Two Higgs Doublet Model (2HDM) [278, 269, 279, 280, 281, 282] and Higgs Triplet Model (HTM) [283, 284, 285, 286, 287]. The new neutral (dubbed as 'H_3') and doubly-charged (dubbed as '$H^{\pm\pm}$') scalar fields might couple to the SM charged leptons through Yukawa interactions:

$$\mathcal{L}_{H_3} \supset Y_{\alpha\beta}\overline{\ell_\alpha}H_3\ell_\beta + \text{H.c.}, \tag{5.1}$$

$$\mathcal{L}_{H^{++}} \supset Y_{\alpha\beta}\overline{\ell^C_\alpha}H^{++}\ell_\beta + \text{H.c.}. \tag{5.2}$$

For example, in LRSM, the physical fields H_3 and $H^{\pm\pm}$ come from the triplet Higgs fields $\Delta_{\rm L,R}$: $H_3 \equiv \text{Re}(\Delta^0)$ and $H^{\pm\pm}_{\rm L,R} \equiv \Delta^{\pm\pm}_{\rm L,R}$, where

$$\Delta_{\rm L,R} = \begin{pmatrix} \Delta^+_{\rm L,R}/\sqrt{2} & \Delta^{++}_{\rm L,R} \\ \Delta^0_{\rm L,R} & -\Delta^+_{\rm L,R}/\sqrt{2} \end{pmatrix}, \tag{5.3}$$

and the triplet $\Delta_{\rm L,R}$ couples to the lepton doublets $L_{{\rm L},\alpha} = (\nu_{\rm L}, e_{\rm L})^T_\alpha$ and $L_{{\rm R},\alpha} = (\nu_{\rm R}, e_{\rm R})^T_\alpha$ through Yukawa interactions

$$\mathcal{L}_{\rm Y} \supset Y_{{\rm L},\alpha\beta}L^T_{{\rm L},\alpha}C^{-1}\sigma_2\Delta_{\rm L}L_{{\rm L},\beta} + Y_{{\rm R},\alpha\beta}L^T_{{\rm R},\alpha}C^{-1}\sigma_2\Delta_{\rm R}L_{{\rm R},\beta} + \text{H.c.}, \tag{5.4}$$

where α and β denote the lepton flavor e, μ or τ and C is the charge conjugation matrix.

These Yukawa interactions are important in addressing the (smallness) of the neutrino masses, the baryon asymmetry of the universe and are responsible for the origin of the electroweak symmetry breaking. The observation of the Yukawa couplings could have important implications for different BSM models, such as theories of neutrino mass and baryogenesis.

If the mass scale of the scalars is less than a few TeV, the lepton colliders (with the $\sqrt{s} \sim$ TeV scale) are especially well-suited for the detections of the scalar fields as well as the study of the corresponding BSM scenarios because they provide clean backgrounds and signals compared to hadron colliders. Lepton colliders can also be run at a fixed center-of-mass energy, which allows for precise control of the collision energy and provides a spectacular chance for the study of the new particles at high precision, such as their masses, couplings, and decay modes.

In this chapter, ignoring the actual detailed form of the Yukawa interactions, I simply treat the overall Yukawa couplings as the model-independent observables and study their discovery prospect at future lepton colliders such as International Linear Collider (ILC) [288, 289] with a center of mass energy of 1.0 TeV and Compact Linear Collider (CLIC) [290, 291] with center of mass energies of 1.5 TeV and 3 TeV. The final states in the collider searches will be fairly similar as both neutral and doubly-charged scalars couple to SM charged leptons. In this chapter, I also make a detailed investigation, outlining the differences between their final states under various cases, along with their distinctive di-lepton invariant mass distributions.

5.2 Theoretical Analysis

At lepton colliders, the interaction terms presented in Eq. (5.1) and Eq. (5.2) will produce highly comparable final states consisting of multiple charged leptons. To demonstrate the differences and for simplicity, I only consider the e, μ sector of the Yukawa matrices and further assume the diagonal and off-diagonal couplings are equal separately: $|Y_{ee}| = |Y_{\mu\mu}|$ and $|Y_{e\mu}| = |Y_{\mu e}|$.

Because of the extremely strong constraints of $\mu \to ee\bar{e}$ ($< 1.0 \times 10^{-12}$ at 90% CL) [58] and $\mu \to e\gamma$ ($< 4.2 \times 10^{-13}$ at 90% CL) [55], the diagonal and off-diagonal terms cannot be large at the same time. Otherwise, these LFV rare lepton decay processes can happen at the tree level (for $\mu \to ee\bar{e}$) and one-loop level (for $\mu \to e\gamma$) with a neutral or doubly-charged mediator in the diagrams.

Thus, to describe the differences between neutral and doubly-charged scalars and the differences between diagonal and off-diagonal Yukawa couplings in each scalar interaction terms, I consider four characteristic cases in this chapter:

(a) Neutral scalar H_3 with non-zero diagonal Yukawa couplings $|Y_{ee}| = |Y_{\mu\mu}|$.
(b) Neutral scalar H_3 with non-zero off-diagonal Yukawa couplings $|Y_{e\mu}| = |Y_{\mu e}|$.
(c) Doubly-charged scalar $H^{\pm\pm}$ with non-zero diagonal Yukawa couplings $|Y_{ee}| = |Y_{\mu\mu}|$.
(d) Doubly-charged scalar $H^{\pm\pm}$ with non-zero off-diagonal Yukawa couplings $|Y_{e\mu}| = |Y_{\mu e}|$.

From now on, in this chapter, we will use a convention in this chapter that the letters (a), (b), (c), and (d) appearing in the equations, figures, and tables below respectively correspond to the four cases (a), (b), (c), and (d) presented here.

For the possible experimental constraints in the four cases, I use the data from the rare LFV decays $\ell_\alpha \to \ell_\beta \ell_\gamma \ell_\delta$, $\ell_\alpha \to \ell_\beta \gamma$ [194, 292], the muonium oscillation [293], the LEP $e^+e^- \to \ell^+\ell^-$ [294], and the LHC multi-lepton [162, 295].

As for the electron [267, 268] and muon [33] anomalous magnetic moments, I have checked and agree with the previous theoretical expressions [296, 196] for the Δa_e and Δa_μ

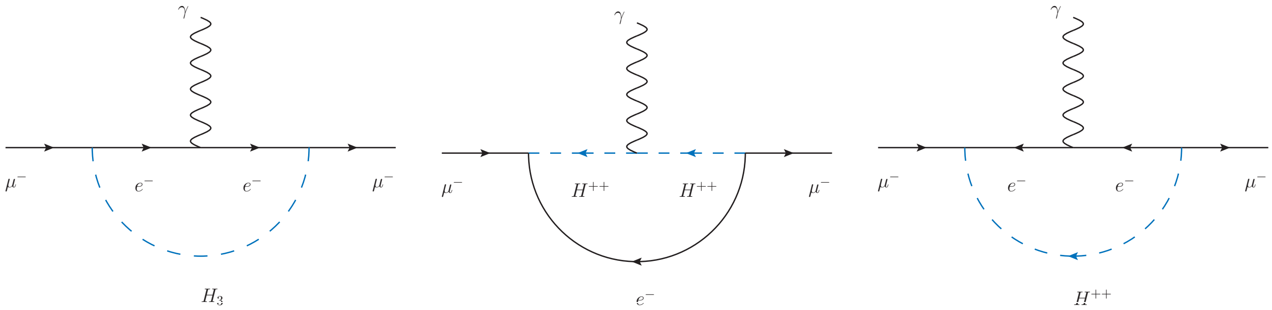

(b) H_3, $|Y_{e\mu}| \neq 0$ (d1) $H^{\pm\pm}$, $|Y_{e\mu}| \neq 0$ (d2) $H^{\pm\pm}$, $|Y_{e\mu}| \neq 0$

Figure 5.1: Feynman diagrams for the $(g-2)_\mu$ in case (b): H_3, $|Y_{e\mu}| \neq 0$ and case (d): $H^{\pm\pm}$, $|Y_{e\mu}| \neq 0$. Feynman diagrams for the $(g-2)_\mu$ in case (a): H_3, $|Y_{ee}| = |Y_{\mu\mu}| \neq 0$ and case (c): $H^{\pm\pm}$, $|Y_{ee}| = |Y_{\mu\mu}| \neq 0$ can be obtained simply by changing all the e indices to μ in the figures. Feynman diagrams for the $(g-2)_e$ can be obtained simply by exchanging all the e and μ indices in the corresponding $(g-2)_\mu$ diagrams.

contributions induced by neutral and doubly-charged scalar fields. Specifically, the $(g-2)_\mu$ contributions in case (b) and case (d) are:

$$\Delta a_\mu^{(\mathrm{b})} = \frac{1}{8\pi^2}\frac{m_\mu^2}{m_{H_3}^2}\int_0^1 \mathrm{d}x \frac{|Y_{e\mu}|^2 x^2 (1 - x + \frac{m_e}{m_\mu})}{(1-x)(1 - \frac{m_\mu^2}{m_{H_3}^2}x) + \frac{m_e^2}{m_{H_3}^2}x}, \tag{5.5b}$$

$$\begin{aligned} \Delta a_\mu^{(\mathrm{d})} = &-\frac{1}{\pi^2}\frac{m_\mu^2}{m_{H^{\pm\pm}}^2}\int_0^1 \mathrm{d}x \frac{|Y_{e\mu}|^2 x(1-x)(x + \frac{m_e}{m_\mu})}{\frac{m_e^2}{m_{H^{\pm\pm}}^2}(1-x)(1 - \frac{m_\mu^2}{m_e^2}x) + x} \\ &- \frac{1}{2\pi^2}\frac{m_\mu^2}{m_{H^{\pm\pm}}^2}\int_0^1 \mathrm{d}x \frac{|Y_{e\mu}|^2 x^2 (1 - x + \frac{m_e}{m_\mu})}{(1-x)(1 - \frac{m_\mu^2}{m_{H^{\pm\pm}}^2}x) + \frac{m_e^2}{m_{H^{\pm\pm}}^2}x}. \end{aligned} \tag{5.5d}$$

The corresponding Feynman diagrams are shown in Fig. 5.1. The Feynman diagrams and the expressions of the $(g-2)_\mu$ contribution in case (a) and case (c) can be easily obtained by changing all the e indices to μ in Fig. 5.1 and Eq. (5.5). The Feynman diagrams and the expressions of the $(g-2)_e$ can be easily obtained by exchanging all the e and μ indices in the corresponding $(g-2)_\mu$ figures and expressions.

5.3 Signal and Background Analysis

I focus on the ILC [289] and CLIC [291] as two benchmark machines for future lepton colliders and present in Table 5.1 their planned final center-of-mass energy $\sqrt{s}$ and the expected integrated luminosity $\mathcal{L}_{\text{int}}$.

Table 5.1: The planned center-of-mass energy and expected integrated luminosity for the International Linear Collider (ILC) and two stages of Compact Linear Collider (CLIC)

Collider	$\sqrt{s}$ (TeV)	$\mathcal{L}_{\text{int}}$ (ab^{-1})
ILC	1.0	4.0
CLIC	1.5	2.5
	3.0	5.0

Based on the four cases mentioned above, I propose two collider signals that can be used to test the $(m_{\text{scalar}}, Y_{\alpha\beta})$ parameter space: $e^+e^- \to e^+e^-\mu^+\mu^-$ and $e^+e^- \to e^+e^+\mu^-\mu^-/e^-e^-\mu^+\mu^+$. The second signal that has two same-sign dilepton pairs violates the lepton flavor and the SM background mainly comes from the misidentification of the lepton flavor in the final states. For lepton colliders, the mis-ID rate for electron and muon is less than 0.5% [297]. This makes $e^\pm e^\pm\mu^\mp\mu^\mp$ almost background free and I find that the background would not have substantial effects on the estimates of the signal sensitivities. For simplicity, I neglect the $e^\pm e^\pm\mu^\mp\mu^\mp$ SM background for all the prospects below. In this chapter, I only consider the $ee\mu\mu$ type of the final state. The $eee\mu$ or $e\mu\mu\mu$ type is closely related to the process $\mu \to e\gamma$ and $\mu \to eee$ which is not possible in the cases considered in this chapter. The $eeee$ and $\mu\mu\mu\mu$ types are possible in the non-zero diagonal coupling case (a) and (c), and will give a similar cross-section compared to their corresponding $ee\mu\mu$ channel.

In this chapter, I perform a simulation for the signal and background processes using MadGraph5_aMC@NLO [169], requiring all leptons in the final states to satisfy the minimal trigger cuts $p_{\text{T}} > 10$ GeV, $|\eta| < 2.5$, and $\Delta R > 0.4$.

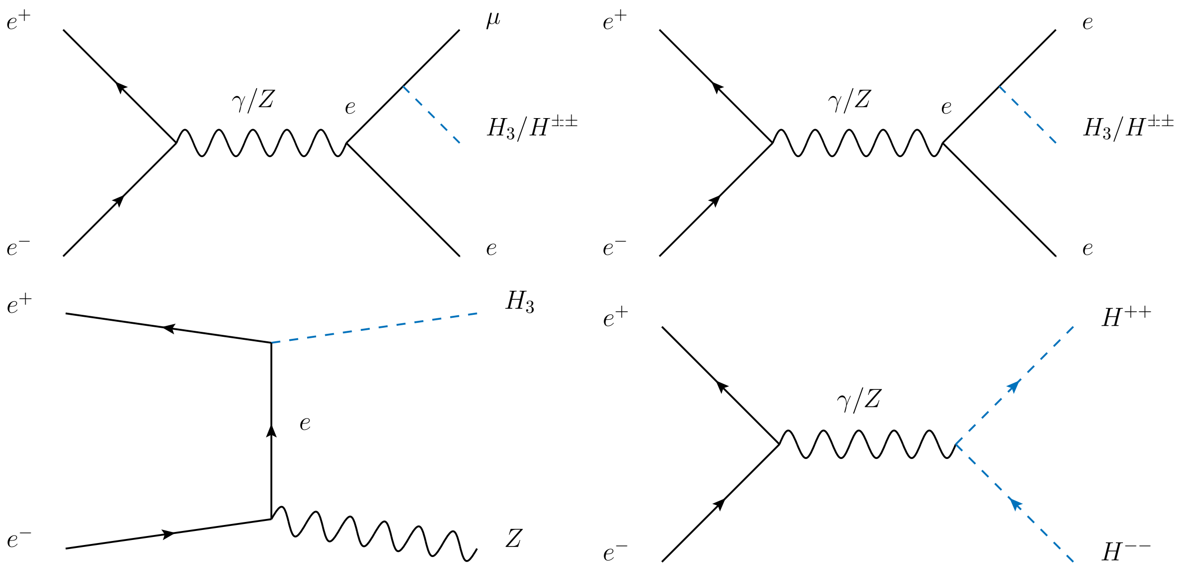

Figure 5.2: Representative Feynman diagrams for the single production of H_3, $H^{\pm\pm}$ and pair production of $H^{\pm\pm}$.

The multi-lepton channels discussed here at future lepton colliders are very clean because we can reconstruct the scalar mass from the dilepton invariant mass. Nevertheless, there are irreducible SM backgrounds, as shown in Fig. 5.4, which make it difficult to disentangle the signal for smaller Yukawa couplings. This has been taken into account while deriving the sensitivity contours.

In this chapter, I only present the cross-sections at the leading order. But since these are electroweak processes, the NLO corrections are expected to be small, and hence, the k-factors should be close to the identity.

The $e^+e^-\mu^+\mu^-$ and $e^\pm e^\pm \mu^\mp \mu^\mp$ signals come from the single production of H_3 or $H^{\pm\pm}$, while there are also contributions from the Drell–Yan pair production of $H^{\pm\pm}$ which are dominant when $m_{H^{\pm\pm}} \lesssim \sqrt{s}/2$ as shown in Fig. 5.2.

I present in Table 5.2 the potential signal(s) for each case along with their corresponding invariant mass distributions. The emergence of a resonance peak in these distributions would signify the existence of a new neutral or doubly-charged Higgs, thereby aiding in the further distinction of the signal from the background. From Table 5.2, we can see that only case (b) can give both signals while the other cases only have one possible signal. As a demonstration, Fig. 5.4 shows the relevant signal and background invariant mass distributions in the $e^+e^-\mu^+\mu^-$ channel. The parameter values used in Fig. 5.4 correspond to the values at the * marks in Fig. 5.3. The clean red peaks in Fig. 5.4 mainly come from the prompt decay of neutral or doubly-charged scalar. The invariant mass distributions in the $e^\pm e^\pm\mu^\mp\mu^\mp$ channel are not shown, since they are almost background free, and the signal distributions are very similar to the ones I present in Fig. 5.4 except for the charge of the electron or muon. In Fig. 5.4(b1) or (d1), the signal events that mainly range from $0 \sim 500$ GeV correspond to the events in the peak of Fig. 5.4(b2) or (d2) and vice versa. For example, in Fig. 5.4(d1), the signal events that ranging from $0 \sim 500$ GeV mainly come from the process $e^+e^- \to e^+\mu^+(H_{\rm L}^{--} \to e^-\mu^-)$ and should peak around 950 GeV in Fig. 5.4(d2), because in Fig. 5.4(d2), it shows the invariant mass distribution of $e^-\mu^-$. This is the feature of the single production channel and would be useful to enhance the signal sensitivity as one can choose a selection like $M_{e^+\mu^-}||M_{e^-\mu^+} > 450$ GeV in Fig. 5.4(b) or $M_{e^+\mu^+}||M_{e^-\mu^-} > 900$ GeV in Fig. 5.4(d).

Table 5.2: Possible signal(s) for each case and the corresponding invariant mass distributions that could be used to distinguish the signal from the background. “-” means the signal is not possible (except for the mis-ID) in the corresponding case.

	$e^+e^- \to e^+e^-\mu^+\mu^-$	$e^+e^- \to e^\pm e^\pm\mu^\mp\mu^\mp$
(a) $H_3, \lvert Y_{ee}\rvert = \lvert Y_{\mu\mu}\rvert$	$M_{e^+e^-}\&M_{\mu^+\mu^-}$	–
(b) $H_3, \lvert Y_{e\mu}\rvert$	$M_{e^+\mu^-}\&M_{e^-\mu^+}$	$M_{e^+\mu^-}\&M_{e^-\mu^+}$
(c) $H^{\pm\pm}, \lvert Y_{ee}\rvert = \lvert Y_{\mu\mu}\rvert$	–	$M_{e^+e^+}\&M_{\mu^+\mu^+}$
(d) $H^{\pm\pm}, \lvert Y_{e\mu}\rvert$	$M_{e^+\mu^+}\&M_{e^-\mu^-}$	–

Except for the basic cuts mentioned above, I also apply some specific cuts to enhance the sensitivity based on the characteristic signatures in each case:

(a) H_3 with diagonal couplings: Only $e^+e^-\mu^+\mu^-$ final state is possible in this case, where $e^+e^- \rightarrow e^+e^-(H_3 \rightarrow \mu^+\mu^-)$ or $e^+e^- \rightarrow \mu^+\mu^-(H_3 \rightarrow e^+e^-)$. Another important channel comes from $e^+e^- \rightarrow ZH_3 \rightarrow e^+e^-\mu^+\mu^-$. We expect the dielectron and dimuon invariant mass $M_{e^+e^-}$ and $M_{\mu^+\mu^-}$ to peak at Z and H_3 mass; see Figs. 5.4(a1) and (a2). However, the SM background has similar $M_{e^+e^-}$ and $M_{\mu^+\mu^-}$ distributions around the Z peak. I find that applying cut on $M_{\mu^+\mu^-}$ or $M_{e^+e^-}$ cannot improve the sensitivities much, and make the sensitivities worse in the region where $m_{H_3} \approx m_Z$. So, I first do not apply any further cut for this case. As a comparison, I also show sensitivities with the cut $M_{\mu^+\mu^-} > 120$ GeV in Fig. 5.3(a). The red, yellow, and blue solid (dashed) contours show the 3σ sensitivities of the signal without (with) applying the cut $M_{\mu^+\mu^-} > 120$ GeV in Fig. 5.3(a). As we can see, the red, yellow, and blue dashed contours cannot improve the sensitivities much and are not valid when $m_{H_3} \lesssim 120$ GeV.

(b) H_3 with off-diagonal couplings: Both $e^+e^-\mu^+\mu^-$ and $e^\pm e^\pm\mu^\mp\mu^\mp$ final states are possible in this case. For the $e^+e^-\mu^+\mu^-$ final state, I further apply the cut $M_{e^+e^-}, M_{\mu^+\mu^-} > 120$ GeV to reduce the events with a Z boson decaying to a pair of leptons. We also expect the invariant mass $M_{e^\pm\mu^\mp}$ to peak at the H_3 mass; see Figs. 5.4(b1) and (b2). Since we do not know the mass of H_3 and cannot tell where the peak should be around, I do not apply cut on $M_{e^\pm\mu^\mp}$ for this case. Because $e^\pm e^\pm\mu^\mp\mu^\mp$ is almost background free, I do not apply any further cut in this channel. In Fig. 5.3(b), the red, yellow, and blue solid (dashed) contours now show the 3σ sensitivities in $e^+e^-\mu^+\mu^-$ ($e^\pm e^\pm\mu^\mp\mu^\mp$) channel. Because the background is small in the $e^\pm e^\pm\mu^\mp\mu^\mp$ channel (assumed to be zero in this chapter), it is not surprising that the red, yellow, and blue dashed contours behave better than the solid contours.

(c) $H^{\pm\pm}$ with diagonal couplings: Only $e^\pm e^\pm\mu^\mp\mu^\mp$ final state is possible in this case. Because $e^\pm e^\pm\mu^\mp\mu^\mp$ is almost background free, I do not apply any further cut for this case.

(d) $H^{\pm\pm}$ with off-diagonal couplings: Only $e^+e^-\mu^+\mu^-$ final state is possible in this case, where $e^+e^- \to e^\mp\mu^\mp(H^{\pm\pm} \to e^\pm\mu^\pm)$. We expect the $e^\pm\mu^\pm$ invariant mass $M_{e^\pm\mu^\pm}$ to peak around the $H^{\pm\pm}$ mass; see Figs. 5.4(d1) and (d2). Because the pair production channel that is independent of the Yukawa coupling is dominant when $m_{H^{\pm\pm}} \lesssim \sqrt{s}/2$, the sensitivity in the $(m_{H^{\pm\pm}}, Y_{e\mu})$ parameter space is only valid in the region where $m_{H^{\pm\pm}} \gtrsim \sqrt{s}/2$. Based on this feature, I further apply the cut $M_{e^\pm\mu^\pm} \gtrsim \sqrt{s}/2$ to maximize the sensitivity. To be specific, I require $M_{e^\pm\mu^\pm} > 500$ GeV at ILC 1.0 TeV stage, $M_{e^\pm\mu^\pm} > 750$ GeV at CLIC 1.5 TeV stage, and $M_{e^\pm\mu^\pm} > 1400$ GeV at CLIC 3.0 TeV stage.

I summarize the further selections used in my analysis in Table 5.3 in the $e^+e^-\mu^+\mu^-$ channel.

Table 5.3: Further selections for the analysis for each case in the $e^+e^-\mu^+\mu^-$ channel

$e^+e^-\mu^+\mu^-$	Selection
case (a)	– or $M_{\mu^+\mu^-} > 120$ GeV
case (b)	$M_{e^+e^-}, M_{\mu^+\mu^-} > 120$ GeV
case (d)	$M_{e^+\mu^+}, M_{e^-\mu^-} \gtrsim \sqrt{s}/2$

5.4 Results

In the Left-Right Symmetric Model [273, 274, 275, 276, 298, 277, 299], the triplet Higgs fields Δ_L and Δ_R transform as triplets under $SU(2)_L$ and $SU(2)_R$ gauge symmetries respectively. Both of them give rise to a doubly-charged Higgs. They are named as $H_\mathrm{L}^{\pm\pm}$ and $H_\mathrm{R}^{\pm\pm}$. Besides, the doubly-charged Higgs in the canonical type-II seesaw model [300, 301, 302] is the same as $H_\mathrm{L}^{\pm\pm}$ and the doubly-charged scalar in the Zee–Babu neutrino mass model [303, 304, 305] has the same quantum numbers as $H_\mathrm{R}^{\pm\pm}$[1]. In case (c) and case (d) of this chapter, I consider both

---

[1] I assume the Z' is much heavier, then the electroweak production of the doubly-charged scalar in the Zee–Babu model is the same as $H_\mathrm{R}^{\pm\pm}$.

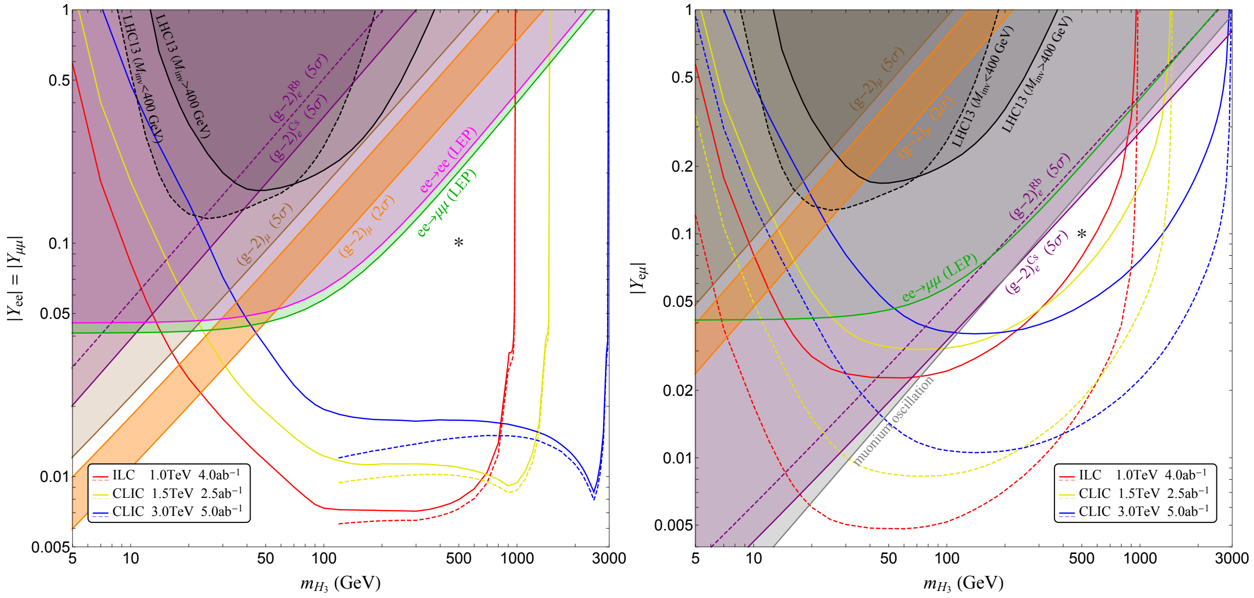

(a) m_{H_3}, $|Y_{ee}| = |Y_{\mu\mu}| \neq 0$

(b) m_{H_3}, $|Y_{e\mu}| \neq 0$

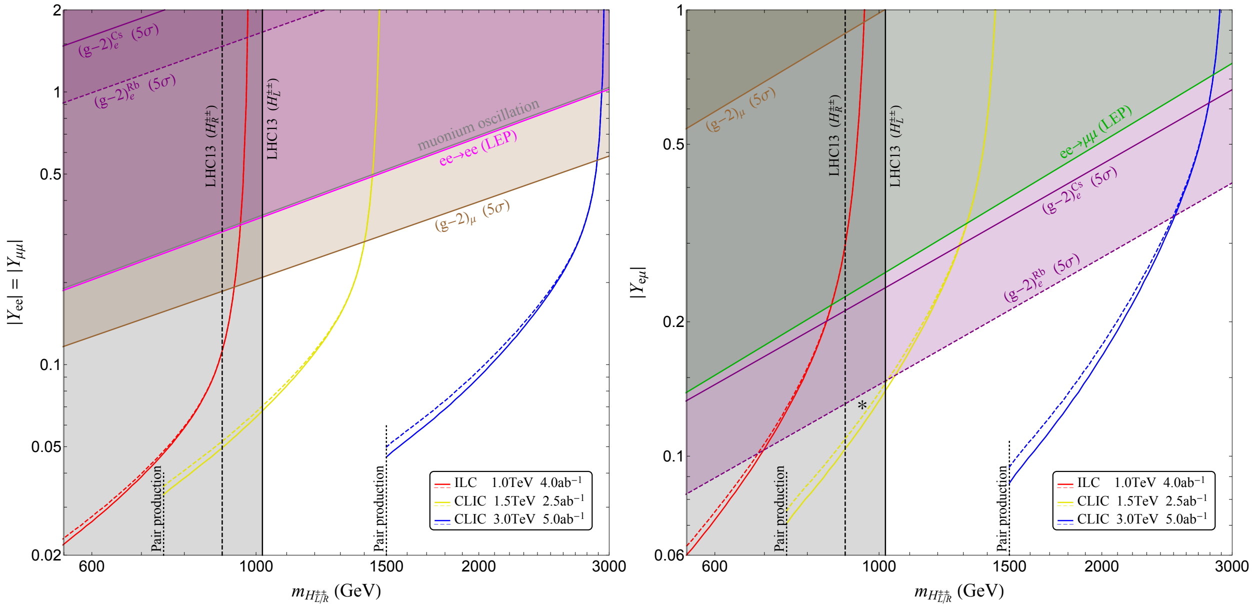

(c) $m_{H^{\pm\pm}_{\rm L,R}}$, $|Y_{ee}| = |Y_{\mu\mu}| \neq 0$

(d) $m_{H^{\pm\pm}_{\rm L,R}}$, $|Y_{e\mu}| \neq 0$

Figure 5.3: Four cases in the H_3 or $H^{\pm\pm}_{\rm L,R}$ parameter space. The red, yellow, and blue contours respectively show the 3σ sensitivities of the 1.0 TeV ILC, 1.5 TeV CLIC, and 3.0 TeV CLIC in the (a) $e^+e^-\mu^+\mu^-$ channel without (solid contours) or with (dashed contours) $M_{\mu^+\mu^-} > 120$ GeV; (b) $e^+e^-\mu^+\mu^-$ channel (solid contours) and $e^\pm e^\pm\mu^\mp\mu^\mp$ channel (dashed contours); (c) $e^\pm e^\pm\mu^\mp\mu^\mp$ channel (solid contours for $H^{\pm\pm}_{\rm L}$ and dashed contours for $H^{\pm\pm}_{\rm R}$); (d) $e^+e^-\mu^+\mu^-$ channel (solid contours for $H^{\pm\pm}_{\rm L}$ and dashed contours for $H^{\pm\pm}_{\rm R}$). The * marks in the figures give the representative values of the corresponding parameters used in Fig. 5.4.

$H_{\mathrm{L}}^{\pm\pm}$ and $H_{\mathrm{R}}^{\pm\pm}$. Because they have different couplings to the Z boson [306], their sensitivities (the red, yellow, and blue solid or dashed contours in Figs. 5.3(c) and (d)) are a little bit different but the LHC constraints derived from the Drell–Yan pair production process (the black solid or dashed contours in Figs. 5.3(c) and (d)) have a sizable difference[2].

I consider all the four cases where H_3 or $H_{\mathrm{L,R}}^{\pm\pm}$ has non-zero diagonal or off-diagonal Yukawa couplings in the e, μ sector. In Fig. 5.3, the orange-shaded regions explain the $(g-2)_\mu$ anomaly [33] at 2σ CL, while the brown-shaded regions display the 5σ disfavored regions of Δa_μ. As shown in Eq. (5.5), the doubly-charged scalar has an opposite contribution to Δa_μ, so there is no 2σ favored region in Figs. 5.3(c) and (d). The purple-shaded regions in Fig. 5.3 with solid (dashed) boundaries are the 5σ disfavored regions of Δa_e using Cs [267] (Rb [268]) measurements. Again, because the doubly-charged scalar has an opposite contribution to Δa_e compared with the neutral scalar, the $(g-2)_e^{\mathrm{Cs}}$ constraint is stronger in the H_3 parameter space (Figs. 5.3(a) and (b)), while the $(g-2)_e^{\mathrm{Rb}}$ constraint is stronger in the $H_{\mathrm{L,R}}^{\pm\pm}$ parameter space (Figs. 5.3(c) and (d)). I recast the ATLAS multilepton analysis [162] using the Signal Region 4ℓ Off-Z with $M_{\mathrm{inv}} > (<) 400$ GeV and set new bounds on the neutral scalar H_3 shown as the black solid (dashed) contours in Figs. 5.3(a) and (b). The black solid (dashed) contours in Figs. 5.3(c) and (d) are the 95% CL limits on $m_{H_{\mathrm{L}}^{\pm\pm}}$ ($m_{H_{\mathrm{R}}^{\pm\pm}}$) from the LHC multi-lepton search [295], assuming $\Sigma_{\ell\ell'}\mathrm{BR}(H^{\pm\pm} \to \ell^{\pm}\ell'^{\pm}) = 100\%$. Other shaded regions in Fig. 5.3 show the relevant constraints on the parameter space from muonium oscillation [293] (gray), LEP $ee \to ee$ [294] (magenta), and LEP $ee \to \mu\mu$ [294] (green).

The red, yellow, and blue contours in Fig. 5.3 show the 3σ sensitivities of the 1.0 TeV ILC, 1.5 TeV CLIC, and 3.0 TeV CLIC in the $ee\mu\mu$ channels respectively. To be specific, in Fig. 5.3(a), H_3 with non-zero diagonal Yukawa couplings, the red, yellow, and blue solid (dashed) contours show the 3σ sensitivities in the $e^+e^-\mu^+\mu^-$ channel without (with) cut

---

[2] The cross-section for the pair production of $H_{\mathrm{L}}^{\pm\pm}$ is roughly two times larger than the $H_{\mathrm{R}}^{\pm\pm}$ [295], which makes the constraints of $H_{\mathrm{L}}^{\pm\pm}$ stronger than $H_{\mathrm{R}}^{\pm\pm}$ in Figs. 5.3(c) and (d).

$M_{\mu^+\mu^-} > 120$ GeV; in Fig. 5.3(b), H_3 with non-zero off-diagonal Yukawa couplings, the red, yellow, and blue solid (dashed) contours show the 3σ sensitivities in the $e^+e^-\mu^+\mu^-$ ($e^\pm e^\pm \mu^\mp \mu^\mp$) channel; in Fig. 5.3(c), $H_{\mathrm{L}}^{\pm\pm}$ ($H_{\mathrm{R}}^{\pm\pm}$) with non-zero diagonal Yukawa couplings, the red, yellow, and blue solid (dashed) contours show the 3σ sensitivities in the $e^\pm e^\pm \mu^\mp \mu^\mp$ channel; in Fig. 5.3(d), $H_{\mathrm{L}}^{\pm\pm}$ ($H_{\mathrm{R}}^{\pm\pm}$) with non-zero off-diagonal Yukawa couplings, the red, yellow, and blue solid (dashed) contours show the 3σ sensitivities in the $e^+e^-\mu^+\mu^-$ channel.

In Fig. 5.3, all the red, yellow, and blue contours asymptotically approach the line $m_{H_3, H_{\mathrm{L,R}}^{\pm\pm}} = \sqrt{s}$ because this is the search of the single production channels of the H_3 and $H_{\mathrm{L,R}}^{\pm\pm}$. In case (a), because there is another important channel for the H_3 single production: $e^+e^- \to ZH_3 \to e^+e^-\mu^+\mu^-$, the red, yellow, and blue contours in Fig. 5.3(a) have a kink at $m_{H_3} \approx \sqrt{s} - 90$ GeV which displays the feature that an on-shell Z boson turning into an off-shell Z boson as we increase the mass of H_3.

The red, yellow, blue, and black curves in Figs. 5.3(a) and (b) are increasing fast as the mass of H_3 decrease in the low-mass region because the leptons in the final state are soft and cannot pass the selection of the corresponding p_{T} cutoff. This feature means that, although the on-shell production of H_3 could be very large, the ability to detect the on-shell, low-mass H_3 at colliders is still not promising. However, although the on-shell searches are not sensitive in the low-mass range because of soft leptons, the LEP constraints in Figs. 5.3(a) and (b) give a flat (this is because the EFT approach for the LEP $ee \to \ell\ell$ data is only sensitive to the couplings) and stronger limit when $m_{H_3} \lesssim 10$ GeV.

5.5 Kinematic Distributions

As a demonstration, in Fig. 5.4, I show the signal and background invariant mass distributions in the $e^+e^-\mu^+\mu^-$ channel using the parameter values at the * marks in Fig. 5.3. One can see the red signal resonance peak around the mass of the assumed neutral or doubly-charged scalar. But it is not always useful to put a cut on these distributions because the position of the peak is not known at first. However, the signal peaks in Fig. 5.4 would provide direct evidence of the new particle with its mass and charge.

5.6 Discussions

- **Other possible bounds:** For the neutral Higgs cases, I cannot find any LHCb limit beyond 5 GeV. The future lepton collider constraints I proposed depend on the overall Yukawa couplings while the current constraints mostly come from low-energy data, such as B and K meson mixing [307]. These constraints on the mass of H_3 depend on the specific model-dependent parameters. The future lepton collider constraints derived here are complementary to the low-energy constraints and extend to higher H_3 masses. There also exist astrophysical and cosmological constraints at lower masses ($m_{H_3} < \mathcal{O}(\mathrm{GeV})$) [308, 309]. For this chapter, additional astrophysical and cosmological constraints at lower masses might apply from dark matter direct detection experiments [310], but this requires the Higgs couples to dark matter.

As for the doubly-charged Higgs, there are also studies on the future lepton colliders [311, 312], HL-LHC [313, 311, 312, 314, 315], and FCC-hh [313, 312] that will work up to $\sqrt{s} =$ 100 TeV [316]. At HL-LHC, the Drell-Yan-like pair production channel can improve the limit of the doubly-charged Higgs to ∼1400 GeV at 95% CL [314].

In this chapter, I only show the constraints which depend on the relevant Yukawa couplings and masses. However, there might be additional constraints in a specific model like HTM or LRSM [312], which are stronger. For instance, the Møller scattering limit is stronger than the LEP limit in the parity-violating LRSM [317, 312]. Similarly, the ρ-parameter constraint applies to the HTM with large triplet VEV [312].

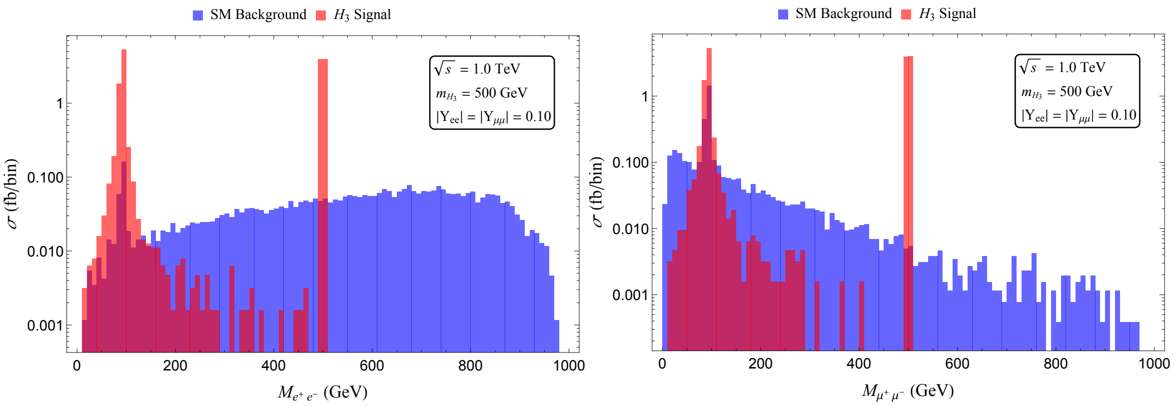

(a1) $m_{H_3} = 500$ GeV, $|Y_{ee}| = |Y_{\mu\mu}| = 0.1$ (a2) $m_{H_3} = 500$ GeV, $|Y_{ee}| = |Y_{\mu\mu}| = 0.1$

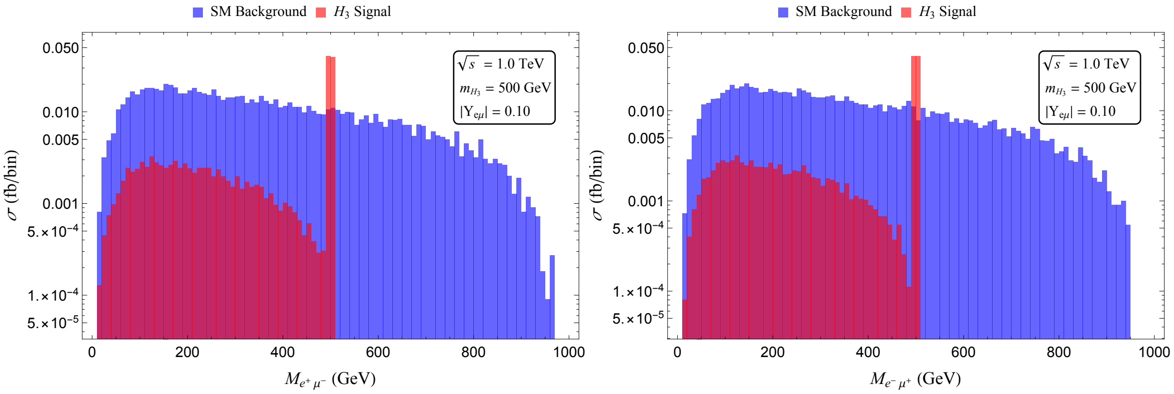

(b1) $m_{H_3} = 500$ GeV, $|Y_{e\mu}| = 0.1$ (b2) $m_{H_3} = 500$ GeV, $|Y_{e\mu}| = 0.1$

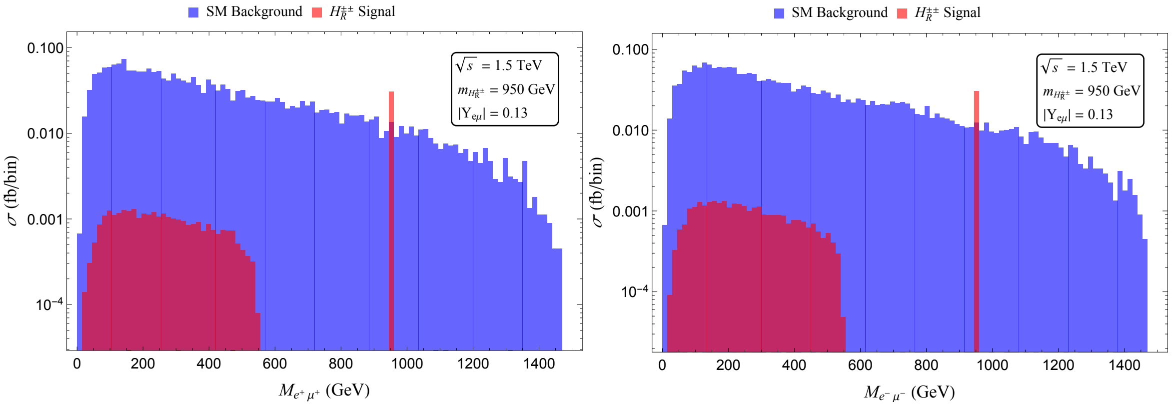

(d1) $m_{H_R^{\pm\pm}} = 950$ GeV, $|Y_{e\mu}| = 0.13$ (d2) $m_{H_R^{\pm\pm}} = 950$ GeV, $|Y_{e\mu}| = 0.13$

Figure 5.4: Invariant mass distributions for case (a) $m_{H_3} = 500$ GeV, $|Y_{ee}| = |Y_{\mu\mu}| = 0.1$ at $\sqrt{s} = 1.0$ TeV; (b) $m_{H_3} = 500$ GeV, $|Y_{e\mu}| = 0.1$ at $\sqrt{s} = 1.0$ TeV; (d) $m_{H_L^{\pm\pm}} = 950$ GeV, $|Y_{e\mu}| = 0.13$ at $\sqrt{s} = 1.5$ TeV signals (red) and SM background (blue) in the $e^+e^- \to e^+e^-\mu^+\mu^-$ channel. The parameter values used here correspond to the values at the * marks in Fig. 5.3.

- **Electron and muon (g-2):** Remarkably, we observe that in Figs. 5.3(a) and (c), the $(g-2)_\mu$ bounds are more stringent than the $(g-2)_e$ ones, whereas in Figs. 5.3(b) and (d), the $(g-2)_e$ bounds are stronger than the $(g-2)_\mu$ ones. Roughly speaking, for the off-diagonal Yukawa coupling case in Eq. (5.5), the dominant contribution to $(g-2)_\mu$ comes from

$$\Delta a_\mu^{\mathrm{off-diagonal}} \propto \frac{m_\mu^2}{m_H^2}\int_0^1 \mathrm{d}x\; x^2 = \frac{m_\mu^2}{3m_H^2}, \tag{5.6}$$

while the dominant contribution to $(g-2)_e$ should be

$$\Delta a_e^{\mathrm{off-diagonal}} \propto \frac{m_e^2}{m_H^2}\int_0^1 \mathrm{d}x\; \frac{x^2(m_\mu/m_e)}{1-x+m_\mu^2/m_H^2} \approx -\frac{m_e m_\mu}{m_H^2}\ln(\frac{m_\mu^2}{m_H^2}). \tag{5.7}$$

This gives $\left(\frac{\Delta a_e}{\Delta a_\mu}\right)_{\mathrm{off-diagonal}} \sim -3\frac{m_e}{m_\mu}\ln(\frac{m_\mu^2}{m_H^2}) \sim \mathcal{O}(0.01)$ to $\mathcal{O}(0.1)$. But for the diagonal Yukawa coupling case, the ratio is simply $\left(\frac{\Delta a_e}{\Delta a_\mu}\right)_{\mathrm{diagonal}} \sim \frac{m_e^2}{m_\mu^2} \sim \mathcal{O}(10^{-5})$. As a result, the $(g-2)_e$ gets a relatively larger contribution in the off-diagonal coupling case than the diagonal coupling case compared with the $(g-2)_\mu$. This means the constraints of the $(g-2)_e$ should be stronger in the off-diagonal case. And that is the reason in Figs. 5.3(b) and (d), the $(g-2)_e$ constraints are stronger than the $(g-2)_\mu$ ones, but in Figs. 5.3(a) and (c), the $(g-2)_\mu$ constraints are stronger.

- **New lattice results on muon (g-2):** In this chapter, my goal is not to address the $(g-2)_\mu$ anomaly but rather focus on the discovery prospect of the neutral and doubly-charged scalars at future lepton colliders. However, in Fig. 5.3(a), there does exist a parameter space of neutral scalar with its mass ranging from 5 $\sim$ 50 GeV that can explain $(g-2)_\mu$ and can be partly tested at CLIC in the $e^+e^-\mu^+\mu^-$ channel.

The discrepancy of Δa_μ used in this chapter comes from the result of the Fermilab Muon $(g-2)$ experiment [33], which is compared with the world-average of the SM prediction using the "R-ratio method" [84] and give a discrepancy of 4.2σ:

$$\Delta a_\mu \equiv a_\mu^{\rm exp} - a_\mu^{\rm SM} = (251 \pm 59) \times 10^{-11}\,. \tag{5.8}$$

But the lattice simulation result from the BMW collaboration [34] increases the leading hadronic contribution of $a_\mu^{\rm SM}$ with a relatively larger uncertainty. There are several new lattice results available now come from other collaborations [35, 36, 37, 38, 39, 40] seem to agree with the BMW result and would result in a discrepancy of $\sim 3.3\sigma$. Note that the center value of Δa_μ determines the position of the orange strip in Fig. 5.3(a) or (b), while the error of Δa_μ determines the width of the orange strip. If the center value of Δa_μ is reduced according to the lattice results and the error is not changed much, the $(g-2)_\mu$ 5σ constraints in Fig. 5.3 would become stronger while the survived $(g-2)_\mu$ 2σ favored region in Fig. 5.3(a) would shift downwards and become larger (in the direction of length) accordingly, because, for a same value of mass, a smaller coupling would be enough to generate the needed value of Δa_μ. As a comparison, the lower orange boundary of the $(g-2)_\mu$ 2σ favored region in Fig. 5.3(a) or (b) corresponds to $\Delta a_\mu = 133 \times 10^{-11}$, which is about 30% larger than the BMW center value $\Delta a_\mu = 107 \times 10^{-11}$.

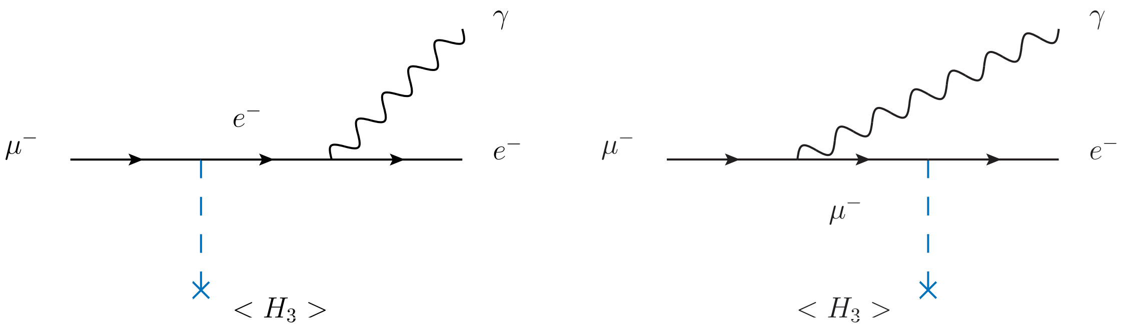

Figure 5.5: $\mu \to e\gamma$ contributions in case (b) H_3, $Y_{e\mu} \neq 0$. However, the total amplitude square is zero.

- **$\mu \to e\gamma$:** Assuming the diagonal and off-diagonal terms of the Yukawa couplings are not zero separately is crucial. It allows us not to worry about the strong constraint from $\mu \to e\gamma$. One would argue that in case (b), even if only the $Y_{e\mu}$ coupling of H_3 is not 0, there are still contributions from the VEV of H_3; see Fig. 5.5. Indeed, the spin averaged amplitude square of each diagram in Fig. 5.5 is

$$\langle |M_1|^2 \rangle \;=\; \langle |M_2|^2 \rangle \;=\; 4e^2|Y_{e\mu}|^2 v^2 \frac{p_e \cdot p_\mu - 2m_e m_\mu}{(m_e - m_\mu)^2}, \tag{5.9}$$

and could be large. But the interference terms will cancel this identically:

$$\langle M_1 M_2^* \rangle \;=\; \langle M_2 M_1^* \rangle \;=\; -4e^2|Y_{e\mu}|^2 v^2 \frac{p_e \cdot p_\mu - 2m_e m_\mu}{(m_e - m_\mu)^2}. \tag{5.10}$$

5.7 Conclusions

Lepton colliders allow for precise measurements of new physics beyond the SM. They produce cleaner collision events with less background noise compared with the hadron colliders.

Focusing on the e, μ sector of the Yukawa coupling matrix of the neutral and doubly-charged scalars, I proposed four characteristic cases and analyzed their discovery prospect in the $e^+e^-\mu^+\mu^-$ and $e^\pm e^\pm \mu^\mp \mu^\mp$ channels at future lepton colliders in a model-independent way. I recast the current ATLAS multilepton analysis [162] and set new bounds on the neutral scalar H_3. I also made a detailed investigation, outlining various di-lepton invariant mass distributions in discriminating signals in each of the cases from backgrounds and from each other. The corresponding Yukawa couplings can be detected ranging from $0.005 \sim 0.5$ at future lepton colliders depending on the cases, $\sqrt{s}$, luminosity, and the mass of the scalar.

I also checked the previous expressions of the electron and muon $(g-2)$ induced by neutral and doubly-charged scalar fields [296, 196]. I further showed that, for both neutral and doubly-charged scalar cases, the $(g-2)_e$ gets a relatively larger contribution in the off-diagonal Yukawa coupling cases while the $(g-2)_\mu$ gets a relatively larger contribution in the diagonal Yukawa coupling cases.

Chapter 6: Conclusions

Throughout this dissertation, we have explored various aspects of LFV and LFUV phenomena in different theoretical frameworks, including R-Parity Violating Supersymmetry (RPV SUSY) and the Left-Right Symmetric Model. We have investigated their implications in addressing anomalies in B-physics, muon $(g-2)$ measurements, and the behavior of new scalars at high-energy colliders.

By combining theoretical analyses, experimental constraints, and phenomenological studies, we have deepened our understanding of the interplay between LFV, LFUV, and other fundamental phenomena in particle physics. These investigations have paved the way for future research and experimental endeavors to further explore and elucidate the nature of BSM physics.

In Chapter 2, we established the RPV3 framework as a natural and well-motivated scenario that can simultaneously explain multiple flavor anomalies while satisfying various low-energy flavor constraints. We identified the distinct roles of the sbottom and sneutrino in addressing specific anomalies, with the sbottom primarily responsible for the $R_{D^{(*)}}$ and $R_{K^{(*)}}$ anomalies, and the sneutrino playing a dominant role in the muon $(g-2)$ anomaly. We proposed specific collider signatures for the sbottom and sneutrino, providing opportunities to test and explore the RPV3 parameter space.

In Chapter 3, building upon the insights gained from Chapter 2, we focused on addressing the muon $(g-2)$ anomaly within the RPV SUSY framework. We proposed an alternative solution to reconcile the discrepancy between theory and experiment in the muon $(g-2)$

measurement, emphasizing the orthogonality between the sbottom and sneutrino parameter spaces. We presented an RPV3 scenario specifically tailored to the muon $(g-2)$ anomaly and investigated its collider implications. We analyzed the Run-2 LHC multilepton data and proposed selection strategies to improve the bounds on the sneutrino mass and relevant RPV couplings. We highlighted the potential of the high-luminosity LHC to provide a robust and independent test of the muon $(g-2)$ anomaly.

In Chapter 4, within the framework of R-Parity Violating Supersymmetry, we focused on the LLE interactions and investigated scenarios with non-zero couplings, including both lepton flavor violating (LFV) and lepton flavor conserving (LFC) cases. We conducted a systematic analysis of the neutrino Non-Standard Interaction (NSI) parameters arising from the LLE interaction terms under different conditions. This analysis revealed interesting connections and correlations between LFV and NSI phenomena, shedding light on the interplay between these aspects within the context of RPV SUSY.

In Chapter 5, inspired by the Left-Right Symmetric Model, we focused on the phenomenology of leptophilic new scalars, particularly electrically neutral and doubly-charged scalars, at future lepton colliders. We explored both lepton flavor violating (LFV) and lepton flavor conserving (LFC) couplings of these scalars. We defined distinct configurations representing different combinations of lepton flavors in the final states and assessed the sensitivity of the International Linear Collider (ILC) and Compact Linear Collider (CLIC) experiments in the relevant mass and coupling parameter space. We introduced various di-lepton invariant mass distributions to effectively distinguish signal events from backgrounds and analyzed the discovery prospects of these scalars in model-independent ways.

In conclusion, the preceding chapters presented a comprehensive exploration of the RPV SUSY framework, addressing various flavor anomalies and exploring their collider implications. We established the RPV3 scenario as a viable and well-motivated framework for explaining the observed anomalies. The orthogonality between the sbottom and sneutrino parameter spaces was a key feature, allowing us to address specific anomalies without affecting others. The proposed collider signatures and experimental tests provided avenues for validating our scenarios and further probing the underlying physics. The connections between LFV and NSI phenomena within the RPV SUSY framework were also explored, shedding light on the interplay between these aspects. Overall, these chapters contribute to our understanding of the RPV SUSY framework and its implications for flavor physics and collider phenomenology.

We anticipate that future advancements in experimental techniques and theoretical developments will continue to shed light on these intriguing phenomena, ultimately leading us closer to a more comprehensive understanding of the fundamental laws of the universe.

References

[1] S. Weinberg, “A Model of Leptons,” *Phys. Rev. Lett.*, vol. 19, pp. 1264–1266, 1967.

[2] C.-N. Yang and R. L. Mills, “Conservation of Isotopic Spin and Isotopic Gauge Invariance,” *Phys. Rev.*, vol. 96, pp. 191–195, 1954.

[3] A. Salam, “Weak and Electromagnetic Interactions,” *Conf. Proc. C*, vol. 680519, pp. 367–377, 1968.

[4] T. D. Lee and C.-N. Yang, “Question of Parity Conservation in Weak Interactions,” *Phys. Rev.*, vol. 104, pp. 254–258, 1956.

[5] Y. Nambu, “Quasiparticles and Gauge Invariance in the Theory of Superconductivity,” *Phys. Rev.*, vol. 117, pp. 648–663, 1960.

[6] J. Goldstone, “Field Theories with Superconductor Solutions,” *Nuovo Cim.*, vol. 19, pp. 154–164, 1961.

[7] P. W. Higgs, “Broken symmetries, massless particles and gauge fields,” *Phys. Lett.*, vol. 12, pp. 132–133, 1964.

[8] F. Englert and R. Brout, “Broken Symmetry and the Mass of Gauge Vector Mesons,” *Phys. Rev. Lett.*, vol. 13, pp. 321–323, 1964.

[9] G. S. Guralnik, C. R. Hagen, and T. W. B. Kibble, "Global Conservation Laws and Massless Particles," *Phys. Rev. Lett.*, vol. 13, pp. 585–587, 1964.

[10] T. W. B. Kibble, "Symmetry breaking in nonAbelian gauge theories," *Phys. Rev.*, vol. 155, pp. 1554–1561, 1967.

[11] P. Stangl, "Clfv in heavy quark decays - interplay between lfv and lfuv," 07 2022. Seattle Snowmass Summer Meeting.

[12] J. P. Lees *et al.*, "Evidence for an excess of $\bar{B} \to D^{(*)}\tau^-\bar{\nu}_\tau$ decays," *Phys. Rev. Lett.*, vol. 109, p. 101802, 2012.

[13] J. P. Lees *et al.*, "Measurement of an Excess of $\bar{B} \to D^{(*)}\tau^-\bar{\nu}_\tau$ Decays and Implications for Charged Higgs Bosons," *Phys. Rev. D*, vol. 88, no. 7, p. 072012, 2013.

[14] R. Aaij *et al.*, "Measurement of the ratio of branching fractions $\mathcal{B}(\bar{B}^0 \to D^{*+}\tau^-\bar{\nu}_\tau)/\mathcal{B}(\bar{B}^0 \to D^{*+}\mu^-\bar{\nu}_\mu)$," *Phys. Rev. Lett.*, vol. 115, no. 11, p. 111803, 2015. [Erratum: Phys.Rev.Lett. 115, 159901 (2015)].

[15] R. Aaij *et al.*, "Measurement of the ratio of the $B^0 \to D^{*-}\tau^+\nu_\tau$ and $B^0 \to D^{*-}\mu^+\nu_\mu$ branching fractions using three-prong τ-lepton decays," *Phys. Rev. Lett.*, vol. 120, no. 17, p. 171802, 2018.

[16] M. Huschle *et al.*, "Measurement of the branching ratio of $\bar{B} \to D^{(*)}\tau^-\bar{\nu}_\tau$ relative to $\bar{B} \to D^{(*)}\ell^-\bar{\nu}_\ell$ decays with hadronic tagging at Belle," *Phys. Rev. D*, vol. 92, no. 7, p. 072014, 2015.

[17] Y. Sato *et al.*, "Measurement of the branching ratio of $\bar{B}^0 \to D^{*+}\tau^-\bar{\nu}_\tau$ relative to $\bar{B}^0 \to D^{*+}\ell^-\bar{\nu}_\ell$ decays with a semileptonic tagging method," *Phys. Rev. D*, vol. 94, no. 7, p. 072007, 2016.

[18] S. Hirose *et al.*, "Measurement of the τ lepton polarization and $R(D^*)$ in the decay $\bar{B} \to D^*\tau^-\bar{\nu}_\tau$," *Phys. Rev. Lett.*, vol. 118, no. 21, p. 211801, 2017.

[19] A. Abdesselam *et al.*, "Measurement of $\mathcal{R}(D)$ and $\mathcal{R}(D^*)$ with a semileptonic tagging method," 4 2019.

[20] R. Aaij *et al.*, "Measurement of CP-Averaged Observables in the $B^0 \to K^{*0}\mu^+\mu^-$ Decay," *Phys. Rev. Lett.*, vol. 125, no. 1, p. 011802, 2020.

[21] R. Aaij *et al.*, "Angular Analysis of the $B^+ \to K^{*+}\mu^+\mu^-$ Decay," *Phys. Rev. Lett.*, vol. 126, no. 16, p. 161802, 2021.

[22] R. Aaij *et al.*, "Differential branching fractions and isospin asymmetries of $B \to K^{(*)}\mu^+\mu^-$ decays," *JHEP*, vol. 06, p. 133, 2014.

[23] R. Aaij *et al.*, "Angular analysis and differential branching fraction of the decay $B_s^0 \to \phi\mu^+\mu^-$," *JHEP*, vol. 09, p. 179, 2015.

[24] R. Aaij *et al.*, "Measurements of the S-wave fraction in $B^0 \to K^+\pi^-\mu^+\mu^-$ decays and the $B^0 \to K^*(892)^0\mu^+\mu^-$ differential branching fraction," *JHEP*, vol. 11, p. 047, 2016. [Erratum: JHEP 04, 142 (2017)].

[25] R. Aaij *et al.*, "Branching Fraction Measurements of the Rare $B_s^0 \to \phi\mu^+\mu^-$ and $B_s^0 \to f_2'(1525)\mu^+\mu^-$- Decays," *Phys. Rev. Lett.*, vol. 127, no. 15, p. 151801, 2021.

[26] R. Aaij *et al.*, “Test of lepton universality with $B^0 \to K^{*0}\ell^+\ell^-$ decays,” *JHEP*, vol. 08, p. 055, 2017.

[27] R. Aaij *et al.*, “Test of lepton universality in beauty-quark decays,” *Nature Phys.*, vol. 18, no. 3, pp. 277–282, 2022.

[28] A. Abdesselam *et al.*, “Test of Lepton-Flavor Universality in $B \to K^*\ell^+\ell^-$ Decays at Belle,” *Phys. Rev. Lett.*, vol. 126, no. 16, p. 161801, 2021.

[29] S. Choudhury *et al.*, “Test of lepton flavor universality and search for lepton flavor violation in $B \to K\ell\ell$ decays,” *JHEP*, vol. 03, p. 105, 2021.

[30] “Test of lepton universality in $b \to s\ell^+\ell^-$ decays,” 12 2022.

[31] “Measurement of lepton universality parameters in $B^+ \to K^+\ell^+\ell^-$ and $B^0 \to K^{*0}\ell^+\ell^-$ decays,” 12 2022.

[32] G. W. Bennett *et al.*, “Final Report of the Muon E821 Anomalous Magnetic Moment Measurement at BNL,” *Phys. Rev. D*, vol. 73, p. 072003, 2006.

[33] B. Abi *et al.*, “Measurement of the Positive Muon Anomalous Magnetic Moment to 0.46 ppm,” *Phys. Rev. Lett.*, vol. 126, no. 14, p. 141801, 2021.

[34] S. Borsanyi *et al.*, “Leading hadronic contribution to the muon magnetic moment from lattice QCD,” *Nature*, vol. 593, no. 7857, pp. 51–55, 2021.

[35] M. Cè *et al.*, “Window observable for the hadronic vacuum polarization contribution to the muon g-2 from lattice QCD,” *Phys. Rev. D*, vol. 106, no. 11, p. 114502, 2022.

[36] C. Alexandrou *et al.*, “Lattice calculation of the short and intermediate time-distance hadronic vacuum polarization contributions to the muon magnetic moment using twisted-mass fermions,” 6 2022.

[37] G. Colangelo, A. X. El-Khadra, M. Hoferichter, A. Keshavarzi, C. Lehner, P. Stoffer, and T. Teubner, “Data-driven evaluations of Euclidean windows to scrutinize hadronic vacuum polarization,” *Phys. Lett. B*, vol. 833, p. 137313, 2022.

[38] C. Lehner, “The hadronic vacuum polarization.” https://indico.ph.ed.ac.uk/event/112/contributions/1660/attachments/1000/1391/talk-nobackup.pdf, 09 2022. Fifth Plenary Workshop of the Muon g-2 Theory Initiative, Edinburgh, UK.

[39] S. Gottlieb, “Hadronic vacuum polarization: An unblinded window on the g-2 mystery.” https://www.benasque.org/2022lattice_workshop/talks_contr/158_Gottlieb_gm2_LatticeNET.pdf, 09 2022. First LatticeNET Workshop on challenges in Lattice field theory, Benasque, Spain.

[40] G. Colangelo, “Dispersive calculation of hadronic contributions to $(g-2)_\mu$.” https://www.benasque.org/2022lattice_workshop/talks_contr/153_g-2_Benasque-2022.pdf, 09 2022. First LatticeNET Workshop on challenges in Lattice field theory, Benasque, Spain.

[41] P. Adamson *et al.*, “First Direct Observation of Muon Antineutrino Disappearance,” *Phys. Rev. Lett.*, vol. 107, p. 021801, 2011.

[42] P. Adamson *et al.*, “Search for the disappearance of muon antineutrinos in the NuMI neutrino beam,” *Phys. Rev. D*, vol. 84, p. 071103, 2011.

[43] P. Adamson *et al.*, “An improved measurement of muon antineutrino disappearance in MINOS,” *Phys. Rev. Lett.*, vol. 108, p. 191801, 2012.

[44] E. Aliu *et al.*, “Evidence for muon neutrino oscillation in an accelerator-based experiment,” *Phys. Rev. Lett.*, vol. 94, p. 081802, 2005.

[45] S. Yamamoto *et al.*, “An Improved search for nu(mu) —> nu(e) oscillation in a long-baseline accelerator experiment,” *Phys. Rev. Lett.*, vol. 96, p. 181801, 2006.

[46] M. H. Ahn *et al.*, “Measurement of Neutrino Oscillation by the K2K Experiment,” *Phys. Rev. D*, vol. 74, p. 072003, 2006.

[47] Y. Fukuda *et al.*, “Evidence for oscillation of atmospheric neutrinos,” *Phys. Rev. Lett.*, vol. 81, pp. 1562–1567, 1998.

[48] Y. Ashie *et al.*, “Evidence for an oscillatory signature in atmospheric neutrino oscillation,” *Phys. Rev. Lett.*, vol. 93, p. 101801, 2004.

[49] Y. Ashie *et al.*, “A Measurement of atmospheric neutrino oscillation parameters by SUPER-KAMIOKANDE I,” *Phys. Rev. D*, vol. 71, p. 112005, 2005.

[50] M. Guler *et al.*, “OPERA: An appearance experiment to search for nu/mu <–> nu/tau oscillations in the CNGS beam. Experimental proposal,” 7 2000.

[51] N. Agafonova *et al.*, “Observation of a first ν_τ candidate in the OPERA experiment in the CNGS beam,” *Phys. Lett. B*, vol. 691, pp. 138–145, 2010.

[52] N. Agafonova *et al.*, “Discovery of τ Neutrino Appearance in the CNGS Neutrino Beam with the OPERA Experiment,” *Phys. Rev. Lett.*, vol. 115, no. 12, p. 121802, 2015.

[53] Y. Kuno and Y. Okada, “Muon decay and physics beyond the standard model,” *Rev. Mod. Phys.*, vol. 73, pp. 151–202, 2001.

[54] A. de Gouvea and P. Vogel, “Lepton Flavor and Number Conservation, and Physics Beyond the Standard Model,” *Prog. Part. Nucl. Phys.*, vol. 71, pp. 75–92, 2013.

[55] A. M. Baldini *et al.*, “Search for the lepton flavour violating decay $\mu^+ \to \mathrm{e}^+\gamma$ with the full dataset of the MEG experiment,” *Eur. Phys. J. C*, vol. 76, no. 8, p. 434, 2016.

[56] B. Aubert *et al.*, “Searches for Lepton Flavor Violation in the Decays tau+- —> e+- gamma and tau+- —> mu+- gamma,” *Phys. Rev. Lett.*, vol. 104, p. 021802, 2010.

[57] A. Abdesselam *et al.*, “Search for lepton-flavor-violating tau-lepton decays to $\ell\gamma$ at Belle,” *JHEP*, vol. 10, p. 19, 2021.

[58] U. Bellgardt *et al.*, “Search for the Decay mu+ —> e+ e+ e-,” *Nucl. Phys. B*, vol. 299, pp. 1–6, 1988.

[59] K. Hayasaka *et al.*, “Search for Lepton Flavor Violating Tau Decays into Three Leptons with 719 Million Produced Tau+Tau- Pairs,” *Phys. Lett.*, vol. B687, pp. 139–143, 2010.

[60] Y. Miyazaki *et al.*, “Search for lepton flavor violating tau- decays into l- eta, l- eta-prime and l- pi0,” *Phys. Lett. B*, vol. 648, pp. 341–350, 2007.

[61] P. S. B. Dev, A. Soni, and F. Xu, “Hints of natural supersymmetry in flavor anomalies?,” *Phys. Rev. D*, vol. 106, no. 1, p. 015014, 2022.

[62] Y. Afik, P. S. B. Dev, A. Soni, and F. Xu, "Probing the muon (g − 2) anomaly at the LHC in final states with two muons and two taus," *Phys. Lett. B*, vol. 843, p. 138032, 2023.

[63] P. S. B. Dev, A. Soni, and F. Xu, "R-parity Violating Supersymmetry and Neutrino Non-Standard Interactions," no. 7, 2023.

[64] F. Xu, "Neutral and Doubly-Charged Scalars at Future Lepton Colliders," 2 2023.

[65] O. Fischer *et al.*, "Unveiling Hidden Physics at the LHC," 9 2021.

[66] J. P. Lees *et al.*, "Evidence for an excess of $\bar{B} \to D^{(*)}\tau^-\bar{\nu}_\tau$ decays," *Phys. Rev. Lett.*, vol. 109, p. 101802, 2012.

[67] M. Huschle *et al.*, "Measurement of the branching ratio of $\bar{B} \to D^{(*)}\tau^-\bar{\nu}_\tau$ relative to $\bar{B} \to D^{(*)}\ell^-\bar{\nu}_\ell$ decays with hadronic tagging at Belle," *Phys. Rev.*, vol. D92, no. 7, p. 072014, 2015.

[68] S. Hirose *et al.*, "Measurement of the τ lepton polarization and $R(D^*)$ in the decay $\bar{B} \to D^*\tau^-\bar{\nu}_\tau$," *Phys. Rev. Lett.*, vol. 118, no. 21, p. 211801, 2017.

[69] A. Abdesselam *et al.*, "Measurement of $\mathcal{R}(D)$ and $\mathcal{R}(D^*)$ with a semileptonic tagging method," 4 2019.

[70] A. Abdesselam *et al.*, "Test of Lepton-Flavor Universality in $B \to K^*\ell^+\ell^-$ Decays at Belle," *Phys. Rev. Lett.*, vol. 126, no. 16, p. 161801, 2021.

[71] S. Choudhury *et al.*, "Test of lepton flavor universality and search for lepton flavor violation in $B \to K\ell\ell$ decays," *JHEP*, vol. 03, p. 105, 2021.

[72] R. Aaij *et al.*, "Measurement of the ratio of branching fractions $\mathcal{B}(\bar{B}^0 \to D^{*+}\tau^-\bar{\nu}_\tau)/\mathcal{B}(\bar{B}^0 \to D^{*+}\mu^-\bar{\nu}_\mu)$," *Phys. Rev. Lett.*, vol. 115, no. 11, p. 111803, 2015. [Erratum: Phys. Rev. Lett.115,no.15,159901(2015)].

[73] R. Aaij *et al.*, "Measurement of the ratio of the $B^0 \to D^{*-}\tau^+\nu_\tau$ and $B^0 \to D^{*-}\mu^+\nu_\mu$ branching fractions using three-prong τ-lepton decays," *Phys. Rev. Lett.*, vol. 120, no. 17, p. 171802, 2018.

[74] R. Aaij *et al.*, "Test of lepton universality with $B^0 \to K^{*0}\ell^+\ell^-$ decays," *JHEP*, vol. 08, p. 055, 2017.

[75] R. Aaij *et al.*, "Search for lepton-universality violation in $B^+ \to K^+\ell^+\ell^-$ decays," *Phys. Rev. Lett.*, vol. 122, no. 19, p. 191801, 2019.

[76] R. Aaij *et al.*, "Test of lepton universality in beauty-quark decays," *Nature Phys.*, vol. 18, no. 3, pp. 277–282, 2022.

[77] Y. S. Amhis *et al.*, "Averages of b-hadron, c-hadron, and τ-lepton properties as of 2018," *Eur. Phys. J. C*, vol. 81, no. 3, p. 226, 2021.

[78] M. Bordone, G. Isidori, and A. Pattori, "On the Standard Model predictions for R_K and R_{K^*}," *Eur. Phys. J.*, vol. C76, no. 8, p. 440, 2016.

[79] F. U. Bernlochner, Z. Ligeti, M. Papucci, and D. J. Robinson, "Combined analysis of semileptonic B decays to D and D^*: $R(D^{(*)})$, $|V_{cb}|$, and new physics," *Phys. Rev.*, vol. D95, no. 11, p. 115008, 2017. [erratum: Phys. Rev.D97,no.5,059902(2018)].

[80] W. Altmannshofer, P. S. B. Dev, A. Soni, and Y. Sui, "Addressing $\mathrm{R}_{D^{(*)}}$, $\mathrm{R}_{K^{(*)}}$, muon $g-2$ and ANITA anomalies in a minimal R-parity violating supersymmetric framework," *Phys. Rev. D*, vol. 102, no. 1, p. 015031, 2020.

[81] F. Jegerlehner and A. Nyffeler, "The Muon g-2," *Phys. Rept.*, vol. 477, pp. 1–110, 2009.

[82] B. Abi *et al.*, "Measurement of the Positive Muon Anomalous Magnetic Moment to 0.46 ppm," *Phys. Rev. Lett.*, vol. 126, no. 14, p. 141801, 2021.

[83] G. W. Bennett *et al.*, "Final Report of the Muon E821 Anomalous Magnetic Moment Measurement at BNL," *Phys. Rev.*, vol. D73, p. 072003, 2006.

[84] T. Aoyama *et al.*, "The anomalous magnetic moment of the muon in the Standard Model," *Phys. Rept.*, vol. 887, pp. 1–166, 2020.

[85] G. Colangelo, M. Hoferichter, and P. Stoffer, "Two-pion contribution to hadronic vacuum polarization," *JHEP*, vol. 02, p. 006, 2019.

[86] M. Benayoun, L. Delbuono, and F. Jegerlehner, "BHLS_2, a New Breaking of the HLS Model and its Phenomenology," *Eur. Phys. J. C*, vol. 80, no. 2, p. 81, 2020. [Erratum: Eur.Phys.J.C 80, 244 (2020)].

[87] M. Hoferichter, B.-L. Hoid, and B. Kubis, "Three-pion contribution to hadronic vacuum polarization," *JHEP*, vol. 08, p. 137, 2019.

[88] M. Davier, A. Hoecker, B. Malaescu, and Z. Zhang, "A new evaluation of the hadronic vacuum polarisation contributions to the muon anomalous magnetic moment and to

$\alpha(\mathbf{m_Z^2})$," *Eur. Phys. J. C*, vol. 80, no. 3, p. 241, 2020. [Erratum: Eur.Phys.J.C 80, 410 (2020)].

[89] A. Keshavarzi, D. Nomura, and T. Teubner, "$g-2$ of charged leptons, $\alpha(M_Z^2)$, and the hyperfine splitting of muonium," *Phys. Rev.*, vol. D101, no. 1, p. 014029, 2020.

[90] B. E. Lautrup, A. Peterman, and E. de Rafael, "Recent developments in the comparison between theory and experiments in quantum electrodynamics," *Phys. Rept.*, vol. 3, pp. 193–259, 1972.

[91] A. Czarnecki, B. Krause, and W. J. Marciano, "Electroweak Fermion loop contributions to the muon anomalous magnetic moment," *Phys. Rev. D*, vol. 52, pp. R2619–R2623, 1995.

[92] A. Czarnecki, B. Krause, and W. J. Marciano, "Electroweak corrections to the muon anomalous magnetic moment," *Phys. Rev. Lett.*, vol. 76, pp. 3267–3270, 1996.

[93] T. Blum, "Lattice calculation of the lowest order hadronic contribution to the muon anomalous magnetic moment," *Phys. Rev. Lett.*, vol. 91, p. 052001, 2003.

[94] S. Borsanyi *et al.*, "Hadronic vacuum polarization contribution to the anomalous magnetic moments of leptons from first principles," *Phys. Rev. Lett.*, vol. 121, no. 2, p. 022002, 2018.

[95] T. Blum, P. A. Boyle, V. Guelpers, T. Izubuchi, L. Jin, C. Jung, A. Juettner, C. Lehner, A. Portelli, and J. T. Tsang, "Calculation of the hadronic vacuum polarization contribution to the muon anomalous magnetic moment," *Phys. Rev. Lett.*, vol. 121, no. 2, p. 022003, 2018.

[96] D. Giusti, V. Lubicz, G. Martinelli, F. Sanfilippo, and S. Simula, “Electromagnetic and strong isospin-breaking corrections to the muon $g-2$ from Lattice QCD+QED,” *Phys. Rev. D*, vol. 99, no. 11, p. 114502, 2019.

[97] E. Shintani and Y. Kuramashi, “Hadronic vacuum polarization contribution to the muon $g-2$ with 2+1 flavor lattice QCD on a larger than $(10\text{ fm})^4$ lattice at the physical point,” *Phys. Rev. D*, vol. 100, no. 3, p. 034517, 2019.

[98] C. T. H. Davies *et al.*, “Hadronic-vacuum-polarization contribution to the muon’s anomalous magnetic moment from four-flavor lattice QCD,” *Phys. Rev. D*, vol. 101, no. 3, p. 034512, 2020.

[99] A. Gérardin, M. Cè, G. von Hippel, B. Hörz, H. B. Meyer, D. Mohler, K. Ottnad, J. Wilhelm, and H. Wittig, “The leading hadronic contribution to $(g-2)_\mu$ from lattice QCD with $N_\mathrm{f} = 2+1$ flavours of $\mathrm{O}(a)$ improved Wilson quarks,” *Phys. Rev. D*, vol. 100, no. 1, p. 014510, 2019.

[100] C. Lehner and A. S. Meyer, “Consistency of hadronic vacuum polarization between lattice QCD and the R-ratio,” *Phys. Rev. D*, vol. 101, p. 074515, 2020.

[101] Y. Shamir, “The Euclidean spectrum of Kaplan’s lattice chiral fermions,” *Phys. Lett. B*, vol. 305, pp. 357–365, 1993.

[102] V. Furman and Y. Shamir, “Axial symmetries in lattice QCD with Kaplan fermions,” *Nucl. Phys. B*, vol. 439, pp. 54–78, 1995.

[103] T. Blum and A. Soni, “QCD with domain wall quarks,” *Phys. Rev. D*, vol. 56, pp. 174–178, 1997.

[104] T. Blum and A. Soni, “Domain wall quarks and kaon weak matrix elements,” *Phys. Rev. Lett.*, vol. 79, pp. 3595–3598, 1997.

[105] C. W. Bernard, T. Draper, A. Soni, H. D. Politzer, and M. B. Wise, “Application of Chiral Perturbation Theory to K —> 2 pi Decays,” *Phys. Rev. D*, vol. 32, pp. 2343–2347, 1985.

[106] W.-J. Lee and S. R. Sharpe, “Partial flavor symmetry restoration for chiral staggered fermions,” *Phys. Rev. D*, vol. 60, p. 114503, 1999.

[107] C. Aubin and C. Bernard, “Pion and kaon masses in staggered chiral perturbation theory,” *Phys. Rev. D*, vol. 68, p. 034014, 2003.

[108] C. Aubin and C. Bernard, “Pseudoscalar decay constants in staggered chiral perturbation theory,” *Phys. Rev. D*, vol. 68, p. 074011, 2003.

[109] A. Crivellin, M. Hoferichter, C. A. Manzari, and M. Montull, “Hadronic Vacuum Polarization: $(g-2)_\mu$ versus Global Electroweak Fits,” *Phys. Rev. Lett.*, vol. 125, no. 9, p. 091801, 2020.

[110] A. Keshavarzi, W. J. Marciano, M. Passera, and A. Sirlin, “Muon $g-2$ and $\Delta\alpha$ connection,” *Phys. Rev. D*, vol. 102, no. 3, p. 033002, 2020.

[111] E. de Rafael, “Constraints between $\Delta\alpha_{\mathrm{had}}(M_Z^2)$ and $(g_\mu - 2)_{\mathrm{HVP}}$,” *Phys. Rev. D*, vol. 102, no. 5, p. 056025, 2020.

[112] B. Malaescu and M. Schott, “Impact of correlations between a_μ and α_{QED} on the EW fit,” *Eur. Phys. J. C*, vol. 81, no. 1, p. 46, 2021.

[113] W. Altmannshofer, P. S. B. Dev, and A. Soni, “$R_{D^{(*)}}$ anomaly: A possible hint for natural supersymmetry with R-parity violation,” *Phys. Rev.*, vol. D96, no. 9, p. 095010, 2017.

[114] C. Brust, A. Katz, S. Lawrence, and R. Sundrum, “SUSY, the Third Generation and the LHC,” *JHEP*, vol. 03, p. 103, 2012.

[115] H. Baer, V. Barger, P. Huang, and X. Tata, “Natural Supersymmetry: LHC, dark matter and ILC searches,” *JHEP*, vol. 05, p. 109, 2012.

[116] M. Badziak, E. Dudas, M. Olechowski, and S. Pokorski, “Inverted Sfermion Mass Hierarchy and the Higgs Boson Mass in the MSSM,” *JHEP*, vol. 07, p. 155, 2012.

[117] R. Barbier *et al.*, “R-parity violating supersymmetry,” *Phys. Rept.*, vol. 420, pp. 1–202, 2005.

[118] L. E. Ibanez and G. G. Ross, “Discrete gauge symmetry anomalies,” *Phys. Lett. B*, vol. 260, pp. 291–295, 1991.

[119] L. E. Ibanez and G. G. Ross, “Discrete gauge symmetries and the origin of baryon and lepton number conservation in supersymmetric versions of the standard model,” *Nucl. Phys. B*, vol. 368, pp. 3–37, 1992.

[120] M. Ablikim *et al.*, “Measurement of the branching fraction for the semi-leptonic decay $D^{0(+)} \to \pi^{-(0)}\mu^+\nu_\mu$ and test of lepton universality,” *Phys. Rev. Lett.*, vol. 121, no. 17, p. 171803, 2018.

[121] M. Ablikim *et al.*, "Study of the $D^0 \to K^-\mu^+\nu_\mu$ dynamics and test of lepton flavor universality with $D^0 \to K^-\ell^+\nu_\ell$ decays," *Phys. Rev. Lett.*, vol. 122, no. 1, p. 011804, 2019.

[122] M. Ablikim, "Observation of the semimuonic decay $D^+ \to \omega\mu^+\nu_\mu$," *Phys. Rev. D*, vol. 101, no. 7, p. 072005, 2020.

[123] M. Ablikim, "First Observation of $D^+ \to \eta\mu^+\nu_\mu$ and Measurement of Its Decay Dynamics," *Phys. Rev. Lett.*, vol. 124, no. 23, p. 231801, 2020.

[124] M. Ablikim *et al.*, "Observation of the decay $D^0 \to \rho^-\mu^+\nu_\mu$," *Phys. Rev. D*, vol. 104, no. 9, p. L091103, 2021.

[125] F. Ambrosino *et al.*, "Precise measurement of $\Gamma(K \to e\nu(\gamma))/\Gamma(K \to \mu\nu(\gamma))$ and study of $K \to e\nu\gamma$," *Eur. Phys. J. C*, vol. 64, pp. 627–636, 2009. [Erratum: Eur.Phys.J. 65, 703 (2010)].

[126] C. Lazzeroni *et al.*, "Precision Measurement of the Ratio of the Charged Kaon Leptonic Decay Rates," *Phys. Lett. B*, vol. 719, pp. 326–336, 2013.

[127] M. Ablikim *et al.*, "First Measurement of the Absolute Branching Fraction of $\Lambda \to p\mu^-\bar{\nu}_\mu$," *Phys. Rev. Lett.*, vol. 127, no. 12, p. 121802, 2021.

[128] N. G. Deshpande and A. Menon, "Hints of R-parity violation in B decays into $\tau\nu$," *JHEP*, vol. 01, p. 025, 2013.

[129] J. Zhu, H.-M. Gan, R.-M. Wang, Y.-Y. Fan, Q. Chang, and Y.-G. Xu, "Probing the R-parity violating supersymmetric effects in the exclusive $b \to c\ell^-\bar{\nu}_\ell decays$," *Phys.*

Rev., vol. D93, no. 9, p. 094023, 2016.

[130] N. G. Deshpande and X.-G. He, "Consequences of R-parity violating interactions for anomalies in $\bar{B} \to D^{(*)}\tau\bar{\nu}$ and $b \to s\mu^+\mu^-$," *Eur. Phys. J. C*, vol. 77, no. 2, p. 134, 2017.

[131] S. Trifinopoulos, "Revisiting R-parity violating interactions as an explanation of the B-physics anomalies," *Eur. Phys. J.*, vol. C78, no. 10, p. 803, 2018.

[132] Q.-Y. Hu, X.-Q. Li, Y. Muramatsu, and Y.-D. Yang, "R-parity violating solutions to the $R_{D^{(*)}}$ anomaly and their GUT-scale unifications," *Phys. Rev.*, vol. D99, no. 1, p. 015008, 2019.

[133] S. Trifinopoulos, "B -physics anomalies: The bridge between R -parity violating supersymmetry and flavored dark matter," *Phys. Rev.*, vol. D100, no. 11, p. 115022, 2019.

[134] D.-Y. Wang, Y.-D. Yang, and X.-B. Yuan, "$b \to c\tau\bar{\nu}$ decays in supersymmetry with R-parity violation," *Chin. Phys.*, vol. C43, no. 8, p. 083103, 2019.

[135] S. Biswas, D. Chowdhury, S. Han, and S. J. Lee, "Explaining the lepton non-universality at the LHCb and CMS within a unified framework," *JHEP*, vol. 02, p. 142, 2015.

[136] D. Das, C. Hati, G. Kumar, and N. Mahajan, "Scrutinizing R-parity violating interactions in light of $R_{K^{(*)}}$ data," *Phys. Rev.*, vol. D96, no. 9, p. 095033, 2017.

[137] K. Earl and T. Grégoire, "Contributions to $b \to s\ell\ell$ Anomalies from R-Parity Violating Interactions," *JHEP*, vol. 08, p. 201, 2018.

[138] Q.-Y. Hu and L.-L. Huang, “Explaining $b \to s\ell^+\ell^-$ data by sneutrinos in the R-parity violating MSSM,” *Phys. Rev.*, vol. D101, no. 3, p. 035030, 2020.

[139] M.-D. Zheng and H.-H. Zhang, “Studying the $b \to s\ell^+\ell^-$ anomalies and $(g-2)_\mu$ in R-parity violating MSSM framework with the inverse seesaw mechanism,” *Phys. Rev. D*, vol. 104, no. 11, p. 115023, 2021.

[140] J. E. Kim, B. Kyae, and H. M. Lee, “Effective supersymmetric theory and (g-2)(muon with R-parity violation,” *Phys. Lett.*, vol. B520, pp. 298–306, 2001.

[141] C. Murgui, A. Peñuelas, M. Jung, and A. Pich, “Global fit to $b \to c\tau\nu$ transitions,” *JHEP*, vol. 09, p. 103, 2019.

[142] M. T. Prim, “Study of Lepton Universality at Belle,” in *54th Rencontres de Moriond on Electroweak Interactions and Unified Theories*, pp. 297–296, 2019.

[143] A. Greljo, J. Martin Camalich, and J. D. Ruiz-Alvarez, “Mono-τ Signatures at the LHC Constrain Explanations of B-decay Anomalies,” *Phys. Rev. Lett.*, vol. 122, no. 13, p. 131803, 2019.

[144] R. Alonso, B. Grinstein, and J. Martin Camalich, “Lifetime of B_c^- Constrains Explanations for Anomalies in $B \to D^{(*)}\tau\nu$,” *Phys. Rev. Lett.*, vol. 118, no. 8, p. 081802, 2017.

[145] A. G. Akeroyd and C.-H. Chen, “Constraint on the branching ratio of $B_c \to \tau\bar{\nu}$ from LEP1 and consequences for $R(D^{(*)})$ anomaly,” *Phys. Rev.*, vol. D96, no. 7, p. 075011, 2017.

[146] J. Aebischer and B. Grinstein, “Standard Model prediction of the B_c lifetime,” *JHEP*, vol. 07, p. 130, 2021.

[147] S. Iguro, “Revival of H- interpretation of RD(*) anomaly and closing low mass window,” *Phys. Rev. D*, vol. 105, no. 9, p. 095011, 2022.

[148] W. Altmannshofer and P. Stangl, “New physics in rare B decays after Moriond 2021,” *Eur. Phys. J. C*, vol. 81, no. 10, p. 952, 2021.

[149] W. Altmannshofer and D. M. Straub, “New Physics in $B \to K^* \mu\mu$?,” *Eur. Phys. J. C*, vol. 73, p. 2646, 2013.

[150] W. Altmannshofer and D. M. Straub, “New physics in $b \to s$ transitions after LHC run 1,” *Eur. Phys. J. C*, vol. 75, no. 8, p. 382, 2015.

[151] P. A. Zyla *et al.*, “Review of Particle Physics,” *PTEP*, vol. 2020, no. 8, p. 083C01, 2020.

[152] T. Moroi, “The Muon anomalous magnetic dipole moment in the minimal supersymmetric standard model,” *Phys. Rev. D*, vol. 53, pp. 6565–6575, 1996. [Erratum: Phys.Rev.D 56, 4424 (1997)].

[153] A. Czarnecki and W. J. Marciano, “The Muon anomalous magnetic moment: A Harbinger for ’new physics’,” *Phys. Rev. D*, vol. 64, p. 013014, 2001.

[154] S. Baum, M. Carena, N. R. Shah, and C. E. M. Wagner, “The tiny (g-2) muon wobble from small-μ supersymmetry,” *JHEP*, vol. 01, p. 025, 2022.

[155] B. C. Allanach, A. Dedes, and H. K. Dreiner, “Two loop supersymmetric renormalization group equations including R-parity violation and aspects of unification,” *Phys. Rev. D*, vol. 60, p. 056002, 1999. [Erratum: Phys.Rev.D 86, 039906 (2012)].

[156] A. M. Sirunyan *et al.*, “Search for the pair production of third-generation squarks with two-body decays to a bottom or charm quark and a neutralino in proton–proton collisions at $\sqrt{s} = 13$ TeV,” *Phys. Lett. B*, vol. 778, pp. 263–291, 2018.

[157] M. R. Buckley, D. Feld, S. Macaluso, A. Monteux, and D. Shih, “Cornering Natural SUSY at LHC Run II and Beyond,” *JHEP*, vol. 08, p. 115, 2017.

[158] D. Bečirević, S. Fajfer, and N. Košnik, “Lepton flavor nonuniversality in b→s$\ell^+\ell^-$ processes,” *Phys. Rev. D*, vol. 92, no. 1, p. 014016, 2015.

[159] “Combination of the ATLAS, CMS and LHCb results on the $B^0_{(s)} \to \mu^+\mu^-$ decays.,” *ATLAS-CONF-2020-049*, 8 2020.

[160] C. Bobeth, M. Gorbahn, T. Hermann, M. Misiak, E. Stamou, and M. Steinhauser, “$B_{s,d} \to l^+l^-$ in the Standard Model with Reduced Theoretical Uncertainty,” *Phys. Rev. Lett.*, vol. 112, p. 101801, 2014.

[161] G. Aad *et al.*, “Search for New Phenomena in Final States with Two Leptons and One or No b-Tagged Jets at $\sqrt{s} = 13$ TeV Using the ATLAS Detector,” *Phys. Rev. Lett.*, vol. 127, no. 14, p. 141801, 2021.

[162] “Search for new phenomena in three- or four-lepton events in *pp* collisions at $\sqrt{s} = 13$ TeV with the ATLAS detector,” *ATLAS-CONF-2021-011*, 3 2021.

[163] G. Aad *et al.*, "Search for supersymmetry in events with four or more leptons in $\sqrt{s} =$ 8 TeV pp collisions with the ATLAS detector," *Phys. Rev. D*, vol. 90, no. 5, p. 052001, 2014.

[164] D. A. Faroughy, A. Greljo, and J. F. Kamenik, "Confronting lepton flavor universality violation in B decays with high-p_T tau lepton searches at LHC," *Phys. Lett.*, vol. B764, pp. 126–134, 2017.

[165] A. Greljo and D. Marzocca, "High-p_T dilepton tails and flavor physics," *Eur. Phys. J.*, vol. C77, no. 8, p. 548, 2017.

[166] Y. Afik, J. Cohen, E. Gozani, E. Kajomovitz, and Y. Rozen, "Establishing a Search for $b \to s\ell^+\ell^-$ Anomalies at the LHC," *JHEP*, vol. 08, p. 056, 2018.

[167] Y. Afik, S. Bar-Shalom, J. Cohen, and Y. Rozen, "Searching for New Physics with $b\bar{b}\ell^+\ell^-$ contact interactions," *Phys. Lett. B*, vol. 807, p. 135541, 2020.

[168] A. M. Sirunyan *et al.*, "Search for resonant and nonresonant new phenomena in high-mass dilepton final states at $\sqrt{s} = 13$ TeV," *JHEP*, vol. 07, p. 208, 2021.

[169] J. Alwall, R. Frederix, S. Frixione, V. Hirschi, F. Maltoni, O. Mattelaer, H. S. Shao, T. Stelzer, P. Torrielli, and M. Zaro, "The automated computation of tree-level and next-to-leading order differential cross sections, and their matching to parton shower simulations," *JHEP*, vol. 07, p. 079, 2014.

[170] A. Chakraborty and S. Chakraborty, "Probing $(g-2)_\mu$ at the LHC in the paradigm of R-parity violating MSSM," *Phys. Rev. D*, vol. 93, no. 7, p. 075035, 2016.

[171] A. Angelescu, D. Bečirević, D. A. Faroughy, F. Jaffredo, and O. Sumensari, “Single leptoquark solutions to the B-physics anomalies,” *Phys. Rev. D*, vol. 104, no. 5, p. 055017, 2021.

[172] L. Calibbi, A. Crivellin, and T. Ota, “Effective Field Theory Approach to $b \to s\ell\ell^{(\prime)}$, $B \to K^{(*)}\nu\bar{\nu}$ and $B \to D^{(*)}\tau\nu$ with Third Generation Couplings,” *Phys. Rev. Lett.*, vol. 115, p. 181801, 2015.

[173] A. Bhaskar, D. Das, T. Mandal, S. Mitra, and C. Neeraj, “Precise limits on the charge-2/3 U1 vector leptoquark,” *Phys. Rev. D*, vol. 104, no. 3, p. 035016, 2021.

[174] K. Ban, Y. Jho, Y. Kwon, S. C. Park, S. Park, and P.-Y. Tseng, “A comprehensive study of vector leptoquark on the B-meson and Muon g-2 anomalies,” 4 2021.

[175] L. Calibbi, A. Crivellin, and T. Li, “Model of vector leptoquarks in view of the B-physics anomalies,” *Phys. Rev. D*, vol. 98, no. 11, p. 115002, 2018.

[176] R. Barbieri and A. Tesi, “B-decay anomalies in Pati-Salam SU(4),” *Eur. Phys. J. C*, vol. 78, no. 3, p. 193, 2018.

[177] M. Blanke and A. Crivellin, “B Meson Anomalies in a Pati-Salam Model within the Randall-Sundrum Background,” *Phys. Rev. Lett.*, vol. 121, no. 1, p. 011801, 2018.

[178] C.-H. Chen, T. Nomura, and H. Okada, “Excesses of muon $g-2$, $R_{D^{(*)}}$, and R_K in a leptoquark model,” *Phys. Lett.*, vol. B774, pp. 456–464, 2017.

[179] A. Crivellin, D. Müller, and T. Ota, “Simultaneous explanation of R(D$^{(*)}$) and b→s $^{+}$ $^{-}$: the last scalar leptoquarks standing,” *JHEP*, vol. 09, p. 040, 2017.

[180] I. Bigaran, J. Gargalionis, and R. R. Volkas, “A near-minimal leptoquark model for reconciling flavour anomalies and generating radiative neutrino masses,” *JHEP*, vol. 10, p. 106, 2019.

[181] A. Crivellin, D. Müller, and F. Saturnino, “Flavor Phenomenology of the Leptoquark Singlet-Triplet Model,” *JHEP*, vol. 06, p. 020, 2020.

[182] S. Saad, “Combined explanations of $(g-2)_\mu$, $R_{D^{(*)}}$, $R_{K^{(*)}}$ anomalies in a two-loop radiative neutrino mass model,” *Phys. Rev. D*, vol. 102, no. 1, p. 015019, 2020.

[183] K. S. Babu, P. S. B. Dev, S. Jana, and A. Thapa, “Unified framework for B-anomalies, muon $g-2$ and neutrino masses,” *JHEP*, vol. 03, p. 179, 2021.

[184] M. Bauer and M. Neubert, “Minimal Leptoquark Explanation for the $\mathrm{R}_{D^{(*)}}$, R_K , and $(g-2)_g$ Anomalies,” *Phys. Rev. Lett.*, vol. 116, no. 14, p. 141802, 2016.

[185] A. Carvunis, A. Crivellin, D. Guadagnoli, and S. Gangal, “The Forward-Backward Asymmetry in $B \to D^* \ell \nu$: One more hint for Scalar Leptoquarks?,” *Phys. Rev. D*, vol. 105, no. 3, p. L031701, 2022.

[186] A. Angelescu, D. Becirevic, D. A. Faroughy, and O. Sumensari, “Closing the window on single leptoquark solutions to the B-physics anomalies,” *JHEP*, vol. 10, p. 183, 2018.

[187] J. Grygier *et al.*, “Search for $B \to h\nu\bar{\nu}$ decays with semileptonic tagging at Belle,” *Phys. Rev. D*, vol. 96, no. 9, p. 091101, 2017. [Addendum: Phys.Rev.D 97, 099902 (2018)].

[188] A. J. Buras, J. Girrbach-Noe, C. Niehoff, and D. M. Straub, “$B \to K^{(*)}\nu\bar{\nu}$ decays in the Standard Model and beyond,” *JHEP*, vol. 02, p. 184, 2015.

[189] W. Altmannshofer *et al.*, “The Belle II Physics Book,” *PTEP*, vol. 2019, no. 12, p. 123C01, 2019. [Erratum: PTEP 2020, 029201 (2020)].

[190] L. J. Hall and M. Suzuki, “Explicit R-Parity Breaking in Supersymmetric Models,” *Nucl. Phys.*, vol. B231, pp. 419–444, 1984.

[191] K. S. Babu and R. N. Mohapatra, “Supersymmetry and Large Transition Magnetic Moment of the Neutrino,” *Phys. Rev. Lett.*, vol. 64, p. 1705, 1990.

[192] N. Aghanim *et al.*, “Planck 2018 results. VI. Cosmological parameters,” *Astron. Astrophys.*, vol. 641, p. A6, 2020. [Erratum: Astron.Astrophys. 652, C4 (2021)].

[193] G. Moreau and M. Chemtob, “R-parity violation and the cosmological gravitino problem,” *Phys. Rev. D*, vol. 65, p. 024033, 2001.

[194] R. L. Workman *et al.*, “Review of Particle Physics,” *PTEP*, vol. 2022, p. 083C01, 2022.

[195] G. Colangelo, M. Hoferichter, and P. Stoffer, “Constraints on the two-pion contribution to hadronic vacuum polarization,” *Phys. Lett. B*, vol. 814, p. 136073, 2021.

[196] M. Lindner, M. Platscher, and F. S. Queiroz, “A Call for New Physics : The Muon Anomalous Magnetic Moment and Lepton Flavor Violation,” *Phys. Rept.*, vol. 731, pp. 1–82, 2018.

[197] P. Athron, C. Balázs, D. H. J. Jacob, W. Kotlarski, D. Stöckinger, and H. Stöckinger-Kim, “New physics explanations of a_μ in light of the FNAL muon $g-2$ measurement,” *JHEP*, vol. 09, p. 080, 2021.

[198] Y. Afik, S. Bar-Shalom, K. Pal, A. Soni, and J. Wudka, “Multi-lepton probes of new physics and lepton-universality in top-quark interactions,” *Nucl. Phys. B*, vol. 980, p. 115849, 2022.

[199] R. Jackiw and S. Weinberg, “Weak interaction corrections to the muon magnetic moment and to muonic atom energy levels,” *Phys. Rev. D*, vol. 5, pp. 2396–2398, 1972.

[200] A. Crivellin and M. Hoferichter, “The Anomalous Magnetic Moment of the Muon: Beyond the Standard Model via Chiral Enhancement,” 7 2022.

[201] D. Stöckinger and H. Stöckinger-Kim, “On the role of chirality flips for the muon magnetic moment and its relation to the muon mass,” *Front. in Phys.*, vol. 10, p. 944614, 2022.

[202] A. Freitas, J. Lykken, S. Kell, and S. Westhoff, “Testing the Muon g-2 Anomaly at the LHC,” *JHEP*, vol. 05, p. 145, 2014. [Erratum: JHEP 09, 155 (2014)].

[203] D. Sabatta, A. S. Cornell, A. Goyal, M. Kumar, B. Mellado, and X. Ruan, “Connecting muon anomalous magnetic moment and multi-lepton anomalies at LHC,” *Chin. Phys. C*, vol. 44, no. 6, p. 063103, 2020.

[204] R. Capdevilla, D. Curtin, Y. Kahn, and G. Krnjaic, “No-lose theorem for discovering the new physics of (g-2)μ at muon colliders,” *Phys. Rev. D*, vol. 105, no. 1, p. 015028, 2022.

[205] N. Arkani-Hamed and K. Harigaya, “Naturalness and the muon magnetic moment,” *JHEP*, vol. 09, p. 025, 2021.

[206] K. S. Babu, S. Jana, and M. Lindner, “Large Neutrino Magnetic Moments in the Light of Recent Experiments,” *JHEP*, vol. 10, p. 040, 2020.

[207] A. Crivellin and M. Hoferichter, “Hints of lepton flavor universality violations,” *Science*, vol. 374, no. 6571, p. 1051, 2021.

[208] N. G. Deshpande and X.-G. He, “Consequences of R-parity violating interactions for anomalies in $\bar{B} \to D^{(*)}\tau\bar{\nu}$ and $b \to s\mu^+\mu^-$,” *Eur. Phys. J. C*, vol. 77, no. 2, p. 134, 2017.

[209] D. Bardhan, D. Ghosh, and D. Sachdeva, “$R_{K^{(*)}}$ from RPV-SUSY sneutrinos,” 7 2021.

[210] M.-D. Zheng, F.-Z. Chen, and H.-H. Zhang, “Explaining anomalies of B-physics, muon $g-2$ and W mass in R-parity violating MSSM with seesaw mechanism,” *Eur. Phys. J. C*, vol. 82, no. 10, p. 895, 2022.

[211] D. Decamp *et al.*, “Searches for new particles in Z decays using the ALEPH detector,” *Phys. Rept.*, vol. 216, pp. 253–340, 1992.

[212] G. Aad *et al.*, “Search for supersymmetry in events with four or more charged leptons in 139 fb^{-1} of $\sqrt{s} = 13$ TeV pp collisions with the ATLAS detector,” *JHEP*, vol. 07, p. 167, 2021.

[213] J. P. Leveille, “The Second Order Weak Correction to (G-2) of the Muon in Arbitrary Gauge Models,” *Nucl. Phys. B*, vol. 137, pp. 63–76, 1978.

[214] M. Chakraborti, S. Iwamoto, J. S. Kim, R. Masełek, and K. Sakurai, “Supersymmetric explanation of the muon g – 2 anomaly with and without stable neutralino,” *JHEP*,

vol. 08, p. 124, 2022.

[215] M. Aaboud *et al.*, “Search for lepton-flavor violation in different-flavor, high-mass final states in pp collisions at $\sqrt{s} = 13$ TeV with the ATLAS detector,” *Phys. Rev. D*, vol. 98, no. 9, p. 092008, 2018.

[216] W. Fetscher, H. J. Gerber, and K. F. Johnson, “Muon Decay: Complete Determination of the Interaction and Comparison with the Standard Model,” *Phys. Lett. B*, vol. 173, pp. 102–106, 1986.

[217] V. D. Barger, G. F. Giudice, and T. Han, “Some New Aspects of Supersymmetry R-Parity Violating Interactions,” *Phys. Rev. D*, vol. 40, p. 2987, 1989.

[218] S. Davidson and M. Losada, “Basis independent neutrino masses in the R(p) violating MSSM,” *Phys. Rev. D*, vol. 65, p. 075025, 2002.

[219] A. Alloul, N. D. Christensen, C. Degrande, C. Duhr, and B. Fuks, “FeynRules 2.0 - A complete toolbox for tree-level phenomenology,” *Comput. Phys. Commun.*, vol. 185, pp. 2250–2300, 2014.

[220] R. D. Ball *et al.*, “Parton distributions for the LHC Run II,” *JHEP*, vol. 04, p. 040, 2015.

[221] S. Catani, Y. L. Dokshitzer, M. H. Seymour, and B. R. Webber, “Longitudinally invariant K_t clustering algorithms for hadron hadron collisions,” *Nucl. Phys. B*, vol. 406, pp. 187–224, 1993.

[222] S. Mrenna and P. Skands, “Automated Parton-Shower Variations in Pythia 8,” *Phys. Rev. D*, vol. 94, no. 7, p. 074005, 2016.

[223] M. L. Mangano, M. Moretti, F. Piccinini, and M. Treccani, “Matching matrix elements and shower evolution for top-quark production in hadronic collisions,” *JHEP*, vol. 01, p. 013, 2007.

[224] J. de Favereau, C. Delaere, P. Demin, A. Giammanco, V. Lemaître, A. Mertens, and M. Selvaggi, “DELPHES 3, A modular framework for fast simulation of a generic collider experiment,” *JHEP*, vol. 02, p. 057, 2014.

[225] M. Cacciari, G. P. Salam, and G. Soyez, “The anti-k_t jet clustering algorithm,” *JHEP*, vol. 04, p. 063, 2008.

[226] M. Cacciari, G. P. Salam, and G. Soyez, “FastJet User Manual,” *Eur. Phys. J. C*, vol. 72, p. 1896, 2012.

[227] M. Cacciari and G. P. Salam, “Dispelling the N^3 myth for the k_t jet-finder,” *Phys. Lett. B*, vol. 641, pp. 57–61, 2006.

[228] “Expected performance of the ATLAS b-tagging algorithms in Run-2,” Tech. Rep. ATL-PHYS-PUB-2015-022, CERN, Geneva, Jul 2015.

[229] “Reconstruction, Energy Calibration, and Identification of Hadronically Decaying Tau Leptons in the ATLAS Experiment for Run-2 of the LHC,” tech. rep., CERN, Geneva, Nov 2015.

[230] W. Verkerke and D. P. Kirkby, “The RooFit toolkit for data modeling,” *eConf*, vol. C0303241, p. MOLT007, 2003.

[231] G. Aad *et al.*, “Search for new phenomena in events with an energetic jet and missing transverse momentum in pp collisions at $\sqrt{s}$ =13 TeV with the ATLAS detector,” *Phys. Rev. D*, vol. 103, no. 11, p. 112006, 2021.

[232] “A Combination of preliminary electroweak measurements and constraints on the standard model,” 12 2003.

[233] P. Achard *et al.*, “Single photon and multiphoton events with missing energy in e^+e^- collisions at LEP,” *Phys. Lett. B*, vol. 587, pp. 16–32, 2004.

[234] H. E. Haber and D. Wyler, “RADIATIVE NEUTRALINO DECAY,” *Nucl. Phys. B*, vol. 323, pp. 267–310, 1989.

[235] H. K. Dreiner, D. Köhler, S. Nangia, and Z. S. Wang, “Searching for a single photon from lightest neutralino decays in R-parity-violating supersymmetry at FASER,” *JHEP*, vol. 02, p. 120, 2023.

[236] L. Covi, J. Hasenkamp, S. Pokorski, and J. Roberts, “Gravitino Dark Matter and general neutralino NLSP,” *JHEP*, vol. 11, p. 003, 2009.

[237] M. Abe *et al.*, “A New Approach for Measuring the Muon Anomalous Magnetic Moment and Electric Dipole Moment,” *PTEP*, vol. 2019, no. 5, p. 053C02, 2019.

[238] G. Colangelo *et al.*, “Prospects for precise predictions of a_μ in the Standard Model,” 3 2022.

[239] G. Abbiendi *et al.*, “Measuring the leading hadronic contribution to the muon g-2 via μe scattering,” *Eur. Phys. J.*, vol. C77, no. 3, p. 139, 2017.

[240] P. S. B. Dev, W. Rodejohann, X.-J. Xu, and Y. Zhang, “MUonE sensitivity to new physics explanations of the muon anomalous magnetic moment,” 2020.

[241] A. Masiero, P. Paradisi, and M. Passera, “New physics at the MUonE experiment at CERN,” 2020.

[242] L. Wolfenstein, “Neutrino Oscillations in Matter,” *Phys. Rev. D*, vol. 17, pp. 2369–2374, 1978.

[243] Y. Farzan and M. Tortola, “Neutrino oscillations and Non-Standard Interactions,” *Front. in Phys.*, vol. 6, p. 10, 2018.

[244] *Neutrino Non-Standard Interactions: A Status Report*, vol. 2, 2019.

[245] M. Aaboud *et al.*, “Search for supersymmetry in events with four or more leptons in $\sqrt{s} = 13$ TeV pp collisions with ATLAS,” *Phys. Rev. D*, vol. 98, no. 3, p. 032009, 2018.

[246] P. S. Bhupal Dev, A. Soni, and F. Xu, “Hints of natural supersymmetry in flavor anomalies?,” *Phys. Rev. D*, vol. 106, no. 1, p. 015014, 2022.

[247] H. K. Dreiner, M. Kramer, and B. O’Leary, “Bounds on R-parity violating supersymmetric couplings from leptonic and semi-leptonic meson decays,” *Phys. Rev. D*, vol. 75, p. 114016, 2007.

[248] G. Aad *et al.*, “Search for electroweak production of charginos and sleptons decaying into final states with two leptons and missing transverse momentum in $\sqrt{s} = 13$ TeV pp collisions using the ATLAS detector,” *Eur. Phys. J. C*, vol. 80, no. 2, p. 123, 2020.

[249] A. M. Sirunyan *et al.*, “Search for supersymmetry in final states with two oppositely charged same-flavor leptons and missing transverse momentum in proton-proton collisions at $\sqrt{s} = 13$ TeV,” *JHEP*, vol. 04, p. 123, 2021.

[250] T. L. Collaboration, A. Collaboration, D. Collaboration, L. Collaboration, O. Collaboration, the LEP Electroweak Working Group, the SLD Electroweak, and H. F. Groups, “A combination of preliminary electroweak measurements and constraints on the standard model,” 2004.

[251] E. J. Eichten, K. D. Lane, and M. E. Peskin, “New tests for quark and lepton substructure,” *Phys. Rev. Lett.*, vol. 50, pp. 811–814, Mar 1983.

[252] P. D. Group, R. L. Workman, *et al.*, “Review of Particle Physics,” *Progress of Theoretical and Experimental Physics*, vol. 2022, 08 2022. 083C01.

[253] K. S. Babu, P. S. B. Dev, S. Jana, and A. Thapa, “Non-Standard Interactions in Radiative Neutrino Mass Models,” *JHEP*, vol. 03, p. 006, 2020.

[254] Z. Berezhiani and A. Rossi, “Limits on the nonstandard interactions of neutrinos from e+ e- colliders,” *Phys. Lett. B*, vol. 535, pp. 207–218, 2002.

[255] L3 Collaboration, M. Acciarri, *et al.*, “Determination of the number of light neutrino species from single photon production at lep,” *Physics Letters B*, vol. 431, no. 1, pp. 199–208, 1998.

[256] L3 Collaboration, P. Achard, *et al.*, "Single photon and multiphoton events with missing energy in e^+e^- collisions at LEP," *Phys. Lett. B*, vol. 587, pp. 16–32, 2004.

[257] R. Abbasi *et al.*, "Non-standard neutrino interactions in IceCube," *PoS*, vol. EPS-HEP2021, p. 245, 2022.

[258] J. Barranco, O. G. Miranda, C. A. Moura, and J. W. F. Valle, "Constraining non-standard neutrino-electron interactions," *Phys. Rev. D*, vol. 77, p. 093014, 2008.

[259] M. Deniz *et al.*, "Constraints on Non-Standard Neutrino Interactions and Unparticle Physics with Neutrino-Electron Scattering at the Kuo-Sheng Nuclear Power Reactor," *Phys. Rev. D*, vol. 82, p. 033004, 2010.

[260] S. K. Agarwalla *et al.*, "Constraints on flavor-diagonal non-standard neutrino interactions from Borexino Phase-II," *JHEP*, vol. 02, p. 038, 2020.

[261] P. Adamson *et al.*, "Search for Flavor-Changing Non-Standard Neutrino Interactions by MINOS," *Phys. Rev. D*, vol. 88, no. 7, p. 072011, 2013.

[262] S. Abe *et al.*, "Precision Measurement of Neutrino Oscillation Parameters with KamLAND," *Phys. Rev. Lett.*, vol. 100, p. 221803, 2008.

[263] A. Bolanos, O. G. Miranda, A. Palazzo, M. A. Tortola, and J. W. F. Valle, "Probing non-standard neutrino-electron interactions with solar and reactor neutrinos," *Phys. Rev. D*, vol. 79, p. 113012, 2009.

[264] P. Coloma, M. C. Gonzalez-Garcia, M. Maltoni, J. a. P. Pinheiro, and S. Urrea, "Global constraints on non-standard neutrino interactions with quarks and electrons," 5 2023.

[265] R. Acciarri *et al.*, “Long-Baseline Neutrino Facility (LBNF) and Deep Underground Neutrino Experiment (DUNE): Conceptual Design Report, Volume 2: The Physics Program for DUNE at LBNF,” 12 2015.

[266] S. S. Chatterjee, P. S. B. Dev, and P. A. N. Machado, “Impact of improved energy resolution on DUNE sensitivity to neutrino non-standard interactions,” *JHEP*, vol. 08, p. 163, 2021.

[267] R. H. Parker, C. Yu, W. Zhong, B. Estey, and H. Müller, “Measurement of the fine-structure constant as a test of the standard model,” *Science*, vol. 360, pp. 191 – 195, 2018.

[268] L. Morel, Z. Yao, P. Cladé, and S. Guellati-Khélifa, “Determination of the fine-structure constant with an accuracy of 81 parts per trillion,” *Nature*, vol. 588, no. 7836, pp. 61–65, 2020.

[269] J. F. Gunion, H. E. Haber, G. L. Kane, and S. Dawson, *The Higgs Hunter’s Guide*, vol. 80. 2000.

[270] J. F. Gunion, “Extended Higgs sectors,” in *10th International Conference on Supersymmetry and Unification of Fundamental Interactions (SUSY02)*, pp. 80–103, 12 2002.

[271] M. Carena and H. E. Haber, “Higgs Boson Theory and Phenomenology,” *Prog. Part. Nucl. Phys.*, vol. 50, pp. 63–152, 2003.

[272] J. D. Lykken, “Beyond the Standard Model,” 5 2010.

[273] J. C. Pati and A. Salam, "Lepton Number as the Fourth Color," *Phys. Rev. D*, vol. 10, pp. 275–289, 1974. [Erratum: Phys.Rev.D 11, 703–703 (1975)].

[274] R. N. Mohapatra and J. C. Pati, "A Natural Left-Right Symmetry," *Phys. Rev. D*, vol. 11, p. 2558, 1975.

[275] G. Senjanovic and R. N. Mohapatra, "Exact Left-Right Symmetry and Spontaneous Violation of Parity," *Phys. Rev. D*, vol. 12, p. 1502, 1975.

[276] R. N. Mohapatra, F. E. Paige, and D. P. Sidhu, "Symmetry Breaking and Naturalness of Parity Conservation in Weak Neutral Currents in Left-Right Symmetric Gauge Theories," *Phys. Rev. D*, vol. 17, p. 2462, 1978.

[277] P. S. Bhupal Dev, R. N. Mohapatra, and Y. Zhang, "Probing TeV scale origin of neutrino mass at future lepton colliders via neutral and doubly-charged scalars," *Phys. Rev. D*, vol. 98, no. 7, p. 075028, 2018.

[278] T. D. Lee, "A Theory of Spontaneous T Violation," *Phys. Rev. D*, vol. 8, pp. 1226–1239, 1973.

[279] H. E. Haber and G. L. Kane, "The Search for Supersymmetry: Probing Physics Beyond the Standard Model," *Phys. Rept.*, vol. 117, pp. 75–263, 1985.

[280] J. F. Gunion and H. E. Haber, "Higgs Bosons in Supersymmetric Models. 1.," *Nucl. Phys. B*, vol. 272, p. 1, 1986. [Erratum: Nucl.Phys.B 402, 567–569 (1993)].

[281] G. C. Branco, P. M. Ferreira, L. Lavoura, M. N. Rebelo, M. Sher, and J. P. Silva, "Theory and phenomenology of two-Higgs-doublet models," *Phys. Rept.*, vol. 516,

pp. 1–102, 2012.

[282] M. Black, A. D. Plascencia, and G. Tetlalmatzi-Xolocotzi, “Enhancing Bs→e+e- to an observable level in the two-Higgs-doublet model,” *Phys. Rev. D*, vol. 107, no. 3, p. 035013, 2023.

[283] W. Konetschny and W. Kummer, “Nonconservation of Total Lepton Number with Scalar Bosons,” *Phys. Lett. B*, vol. 70, pp. 433–435, 1977.

[284] M. Magg and C. Wetterich, “Neutrino Mass Problem and Gauge Hierarchy,” *Phys. Lett. B*, vol. 94, pp. 61–64, 1980.

[285] J. Schechter and J. W. F. Valle, “Neutrino Masses in SU(2) x U(1) Theories,” *Phys. Rev. D*, vol. 22, p. 2227, 1980.

[286] T. P. Cheng and L.-F. Li, “Neutrino Masses, Mixings and Oscillations in SU(2) x U(1) Models of Electroweak Interactions,” *Phys. Rev. D*, vol. 22, p. 2860, 1980.

[287] G. Lazarides, Q. Shafi, and C. Wetterich, “Proton Lifetime and Fermion Masses in an SO(10) Model,” *Nucl. Phys. B*, vol. 181, pp. 287–300, 1981.

[288] H. Baer *et al.*, “The International Linear Collider Technical Design Report - Volume 2: Physics,” 6 2013.

[289] L. Evans and S. Michizono, “The International Linear Collider Machine Staging Report 2017,” 11 2017.

[290] E. Accomando *et al.*, "Physics at the CLIC multi-TeV linear collider," in *11th International Conference on Hadron Spectroscopy*, CERN Yellow Reports: Monographs, 6 2004.

[291] M. J. Boland *et al.*, "Updated baseline for a staged Compact Linear Collider," 8 2016.

[292] Y. Amhis *et al.*, "Averages of b-hadron, c-hadron, and τ-lepton properties as of summer 2016," *Eur. Phys. J. C*, vol. 77, no. 12, p. 895, 2017.

[293] L. Willmann *et al.*, "New bounds from searching for muonium to anti-muonium conversion," *Phys. Rev. Lett.*, vol. 82, pp. 49–52, 1999.

[294] J. Abdallah *et al.*, "Measurement and interpretation of fermion-pair production at LEP energies above the Z resonance," *Eur. Phys. J. C*, vol. 45, pp. 589–632, 2006.

[295] "Search for doubly charged Higgs boson production in multi-lepton final states using 139 fb^{-1} of proton-proton collisions at $\sqrt{s} = 13$ TeV with the ATLAS detector," *CERN-EP-2022-212*, 11 2022.

[296] F. S. Queiroz and W. Shepherd, "New Physics Contributions to the Muon Anomalous Magnetic Moment: A Numerical Code," *Phys. Rev. D*, vol. 89, no. 9, p. 095024, 2014.

[297] D. Yu, M. Ruan, V. Boudry, and H. Videau, "Lepton identification at particle flow oriented detector for the future e^+e^- Higgs factories," *Eur. Phys. J. C*, vol. 77, no. 9, p. 591, 2017.

[298] Y. Cai, T. Han, T. Li, and R. Ruiz, "Lepton Number Violation: Seesaw Models and Their Collider Tests," *Front. in Phys.*, vol. 6, p. 40, 2018.

[299] P. S. Bhupal Dev and Y. Zhang, “Displaced vertex signatures of doubly charged scalars in the type-II seesaw and its left-right extensions,” *JHEP*, vol. 10, p. 199, 2018.

[300] A. G. Akeroyd and M. Aoki, “Single and pair production of doubly charged Higgs bosons at hadron colliders,” *Phys. Rev. D*, vol. 72, p. 035011, 2005.

[301] A. Hektor, M. Kadastik, M. Muntel, M. Raidal, and L. Rebane, “Testing neutrino masses in little Higgs models via discovery of doubly charged Higgs at LHC,” *Nucl. Phys. B*, vol. 787, pp. 198–210, 2007.

[302] W. Chao, Z.-G. Si, Z.-z. Xing, and S. Zhou, “Correlative signatures of heavy Majorana neutrinos and doubly-charged Higgs bosons at the Large Hadron Collider,” *Phys. Lett. B*, vol. 666, pp. 451–454, 2008.

[303] A. Zee, “Charged Scalar Field and Quantum Number Violations,” *Phys. Lett. B*, vol. 161, pp. 141–145, 1985.

[304] A. Zee, “Quantum Numbers of Majorana Neutrino Masses,” *Nucl. Phys. B*, vol. 264, pp. 99–110, 1986.

[305] K. S. Babu, “Model of ’Calculable’ Majorana Neutrino Masses,” *Phys. Lett. B*, vol. 203, pp. 132–136, 1988.

[306] B. Fuks, M. Nemevšek, and R. Ruiz, “Doubly Charged Higgs Boson Production at Hadron Colliders,” *Phys. Rev. D*, vol. 101, no. 7, p. 075022, 2020.

[307] P. S. B. Dev, R. N. Mohapatra, and Y. Zhang, “Long Lived Light Scalars as Probe of Low Scale Seesaw Models,” *Nucl. Phys. B*, vol. 923, pp. 179–221, 2017.

[308] M. Ibe, S. Kobayashi, Y. Nakayama, and S. Shirai, “Cosmological constraints on dark scalar,” *JHEP*, vol. 03, p. 198, 2022.

[309] S. Balaji, P. S. B. Dev, J. Silk, and Y. Zhang, “Improved stellar limits on a light CP-even scalar,” *JCAP*, vol. 12, p. 024, 2022.

[310] J. L. Feng *et al.*, “The Forward Physics Facility at the High-Luminosity LHC,” 3 2022.

[311] A. Crivellin, M. Ghezzi, L. Panizzi, G. M. Pruna, and A. Signer, “Low- and high-energy phenomenology of a doubly charged scalar,” *Phys. Rev. D*, vol. 99, no. 3, p. 035004, 2019.

[312] J. Gluza, M. Kordiaczynska, and T. Srivastava, “Discriminating the HTM and MLRSM models in collider studies via doubly charged Higgs boson pair production and the subsequent leptonic decays,” *Chin. Phys. C*, vol. 45, no. 7, p. 073113, 2021.

[313] G. Bambhaniya, J. Chakrabortty, J. Gluza, T. Jelinski, and R. Szafron, “Search for doubly charged Higgs bosons through vector boson fusion at the LHC and beyond,” *Phys. Rev. D*, vol. 92, no. 1, p. 015016, 2015.

[314] “Prospects for a Search for Doubly Charged Higgs Bosons at the HL-LHC,” *CMS-PAS-FTR-22-006*, 2022.

[315] R. Ruiz, “Doubly charged Higgs boson production at hadron colliders II: a Zee-Babu case study,” *JHEP*, vol. 10, p. 200, 2022.

[316] A. Abada *et al.*, “FCC-hh: The Hadron Collider: Future Circular Collider Conceptual Design Report Volume 3,” *Eur. Phys. J. ST*, vol. 228, no. 4, pp. 755–1107, 2019.

[317] P. S. B. Dev, M. J. Ramsey-Musolf, and Y. Zhang, "Doubly-Charged Scalars in the Type-II Seesaw Mechanism: Fundamental Symmetry Tests and High-Energy Searches," *Phys. Rev. D*, vol. 98, no. 5, p. 055013, 2018.

[318] J. Brod, M. Gorbahn, and E. Stamou, "Two-Loop Electroweak Corrections for the $K \to \pi\nu\bar{\nu}$ Decays," *Phys. Rev.*, vol. D83, p. 034030, 2011.

[319] D. Buttazzo, A. Greljo, G. Isidori, and D. Marzocca, "B-physics anomalies: a guide to combined explanations," *JHEP*, vol. 11, p. 044, 2017.

[320] M. Bordone, *B-physics in the standard model and beyond.* PhD thesis, Zurich U., 2018.

[321] L. Di Luzio, M. Kirk, A. Lenz, and T. Rauh, "ΔM_s theory precision confronts flavour anomalies," *JHEP*, vol. 12, p. 009, 2019.

[322] A. J. Buras, S. Jager, and J. Urban, "Master formulae for Delta F=2 NLO QCD factors in the standard model and beyond," *Nucl. Phys.*, vol. B605, pp. 600–624, 2001.

[323] A. Bazavov *et al.*, "$B^0_{(s)}$-mixing matrix elements from lattice QCD for the Standard Model and beyond," *Phys. Rev.*, vol. D93, no. 11, p. 113016, 2016.

[324] P. A. Boyle, L. Del Debbio, N. Garron, A. Juttner, A. Soni, J. T. Tsang, and O. Witzel, "SU(3)-breaking ratios for $D_{(s)}$ and $B_{(s)}$ mesons," 2018.

[325] S. Aoki *et al.*, "FLAG Review 2019: Flavour Lattice Averaging Group (FLAG)," *Eur. Phys. J. C*, vol. 80, no. 2, p. 113, 2020.

[326] R. Aaij *et al.*, "Search for the rare decay $D^0 \to \mu^+\mu^-$," *Phys. Lett.*, vol. B725, pp. 15–24, 2013.

[327] M. Misiak *et al.*, “Updated NNLO QCD predictions for the weak radiative B-meson decays,” *Phys. Rev. Lett.*, vol. 114, no. 22, p. 221801, 2015.

Appendix A: Low Energy Constraints

Despite the many free parameters, our RPV3 scenario is remarkably well-constrained by various low-energy flavor observables so much so that more accurate measurements of $R_{D^{(*)}}$, $R_{K^{(*)}}$ and $(g-2)_\mu$ preserving the central values could have appreciable adverse consequences on our RPV3 explanation of these anomalies. In this section, we summarize all relevant constraints on our RPV3 scenario shown in Fig. 2.5. For more details and additional constraints (which are weaker, and therefore not mentioned here), see Ref. [80].

A.1 $B \to K^{(*)}\nu\bar{\nu}$

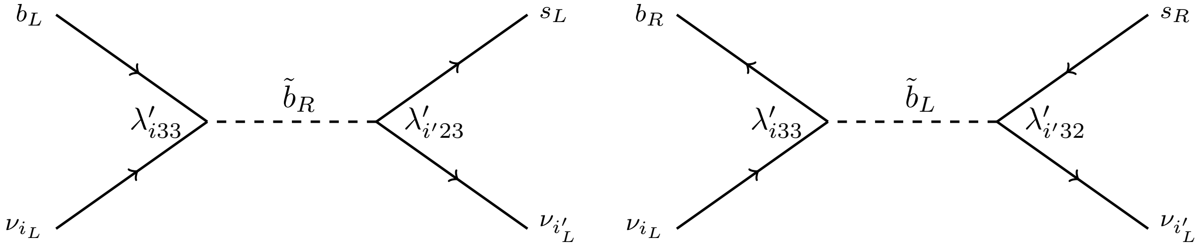

Figure A.1: Contributions to $B \to K^{(*)}\nu\bar{\nu}$ via λ' interactions in RPV3.

As shown in Fig. A.1, $B \to K^{(*)}\nu\bar{\nu}$ receives a tree-level RPV3 contribution via sbottom exchange. The branching ratio is given by

$$\begin{aligned} R_{B\to K^{(*)}\nu\bar{\nu}} &\equiv \frac{\mathrm{BR}(B \to K^{(*)}\nu\bar{\nu})}{\mathrm{BR}(B \to K^{(*)}\nu\bar{\nu})_{\mathrm{SM}}} \\ &= \frac{1}{3}\left|\delta_{ii'} - \frac{v^2\pi s_w^2}{2\alpha_{\mathrm{em}}}\frac{\lambda'_{i33}}{V_{tb}V_{ts}^*}\left(\frac{\lambda'_{i'23}}{m_{\tilde{b}_R}^2} + \frac{\lambda'_{i'32}}{m_{\tilde{b}_L}^2}\right)\frac{1}{X_t}\right|^2 . \end{aligned} \tag{A.1}$$

with the top loop function $X_t = 1.469 \pm 0.017$ [318] and s_w being the weak mixing angle. We consider both $\tilde{b}_L$ and $\tilde{b}_R$ exchanges assuming that $m_{\tilde{b}_L} = m_{\tilde{b}_R}$ for numerical purposes.

An experimental upper bound for this ratio exists: $R_{B\to K^{(*)}\nu\overline{\nu}} < 5.2$ at 95% CL [319, 320], which was adopted for our original parameter setting and indicated in Fig. 2.5 as the solid brown line. However, stronger upper bounds of $R_{B\to K\nu\overline{\nu}} < 3.9$ and $R_{B\to K^{*}\nu\overline{\nu}} < 2.7$ have been quoted by Belle but at 90% CL [187]. In order to make a fair comparison with the other low-energy and collider bounds which are all given at 95% CL, we have derived an approximate 95% CL equivalent bound using the Belle data provided in Ref. [187]. We get $R_{B\to K^{*}\nu\overline{\nu}} \lesssim 3.2$, where we have used the theoretical uncertainty from Ref. [188] and have also taken into account the propagation of uncertainty. This 95% CL upper limit is shown in Fig. 2.5 by the dashed brown line.

A.2 $B_s - \overline{B}_s$ Mixing

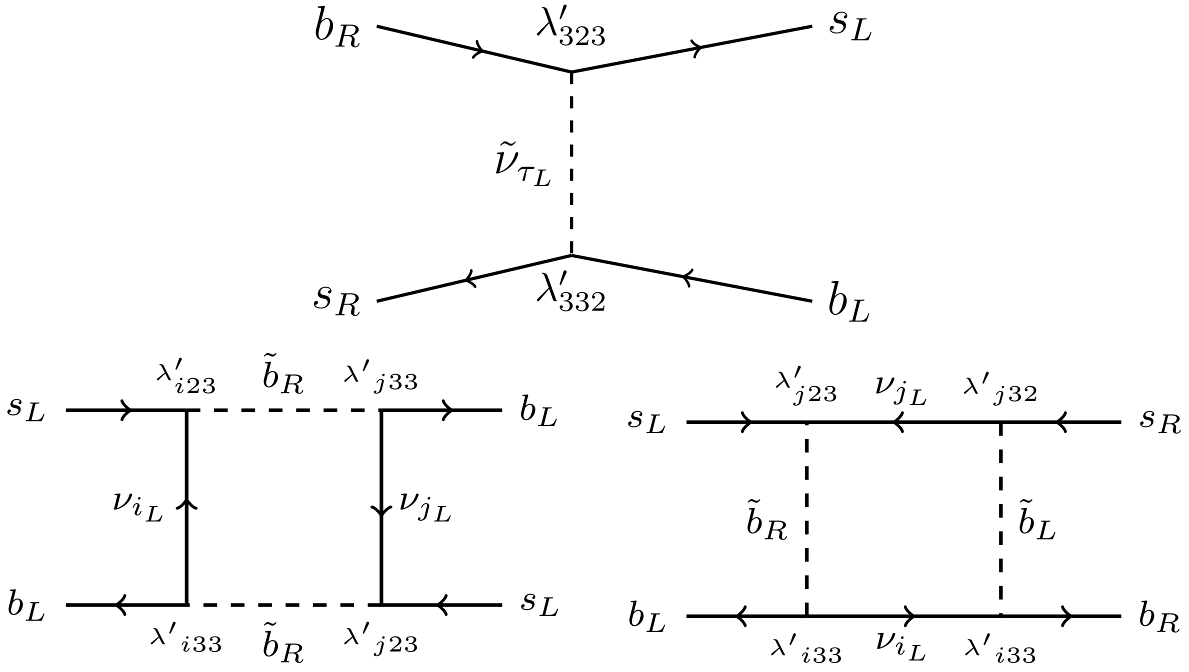

Figure A.2: Relevant contributions to $B_s - \overline{B}_s$ mixing via λ' couplings in RPV3.

Experimentally, the mass difference ΔM_{B_s} in neutral B_s meson mixing is measured with excellent precision, $\Delta M_{B_s} = (17.757 \pm 0.021)\,\mathrm{ps}^{-1}$ [77], dominated by LHCb and still statistically limited. On the other hand, the SM prediction $\Delta M_{B_s}^{\mathrm{SM}} = (19.3 \pm 1.7)\,\mathrm{ps}^{-1}$ [321, 80]

has sizable uncertainties stemming mainly from the hadronic matrix elements and the CKM matrix element V_{cb}.

In RPV3, additional contributions can arise at the tree level from sneutrino exchange, or at the one-loop level from box diagrams with sbottoms, sneutrinos, or stops (see Fig. A.2). For the mass difference, we obtain

$$\begin{aligned}\Delta M_{B_s}^{\rm RPV} &= \frac{2}{3} m_{B_s} f_{B_s}^2 \left| P_1^{VLL} \frac{\lambda'_{i23}\lambda'_{j33}\lambda'_{j23}\lambda'_{i33}}{128\pi^2 m_{\tilde{b}_R}^2} \right. \\ &\left. + P_1^{LR} \frac{\lambda'_{i23}\lambda'_{j33}\lambda'_{i32}\lambda'_{j33}}{128\pi^2 m_{\tilde{b}_R} m_{\tilde{b}_L}} + P_2^{LR} \frac{\lambda'_{332}\lambda'_{323}}{2m_{\tilde{\nu}}^2} \right| , \end{aligned} \tag{A.2}$$

where

$$P_1^{VLL} = 0.80 \, , \; P_1^{LR} = -2.52 \text{ and } P_2^{LR} = 3.08 \; , \tag{A.3}$$

are the updated hadronic P factors from Ref. [322] with the latest lattice input from Ref. [323] (see also Refs. [324, 325]), $f_{B_s} = (274 \pm 8)$ MeV is the B_s decay constant, and i, j are neutrino-flavor indices in the box graphs. Combining our SM prediction with the experimental result we obtain the following bound at 95% C.L. on

$$0.78 < \left| \frac{\Delta M_{B_s}}{\Delta M_{B_s}^{\rm SM}} \right| < 1.12 \; , \tag{A.4}$$

which constrains the RPV3 contribution in Eq. (A.2). This bound is indicated as the magenta-shaded region in Fig. 2.5.

A.3 $D^0 \to \mu^+\mu^-$

As shown in Fig. A.3, there is a tree-level contribution from sbottom exchange to this rare D^0 decay width which can be expressed as

$$\begin{aligned}\Gamma(D^0 \to \mu^+\mu^-) &= \frac{1}{128\pi} \left| \frac{\lambda'_{2j3}\lambda'_{2j'3} V_{uj'} V_{cj}}{m_{\tilde{b}_R}^2} \right|^2 f_D^2 \\ &\times m_D m_\mu^2 \sqrt{1 - 4m_\mu^2/m_D^2} \, , \end{aligned} \tag{A.5}$$

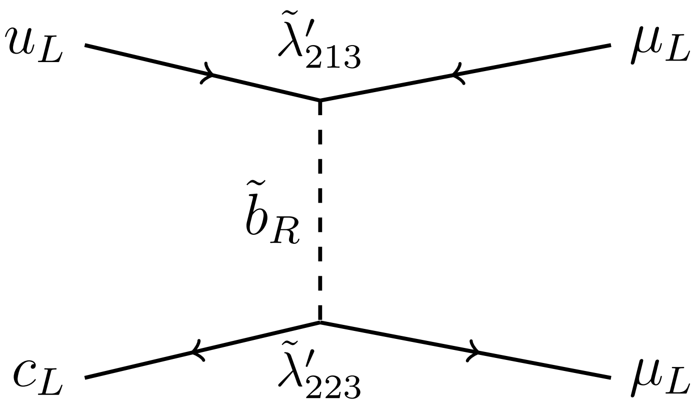

Figure A.3: Contribution to $D^0 \to \mu^+\mu^-$ from λ' in RPV3.

where $f_D = (212 \pm 1)$ MeV is the D^0 decay constant. Using the experimental upper bound on this branching ratio [326] of 7.6×10^{-9} at 95% CL, we calculate the corresponding bound on the RPV3 parameter space, as shown by the purple-shaded region in Fig. 2.5.

A.4 $Z \to \ell\bar{\ell}^{'}$

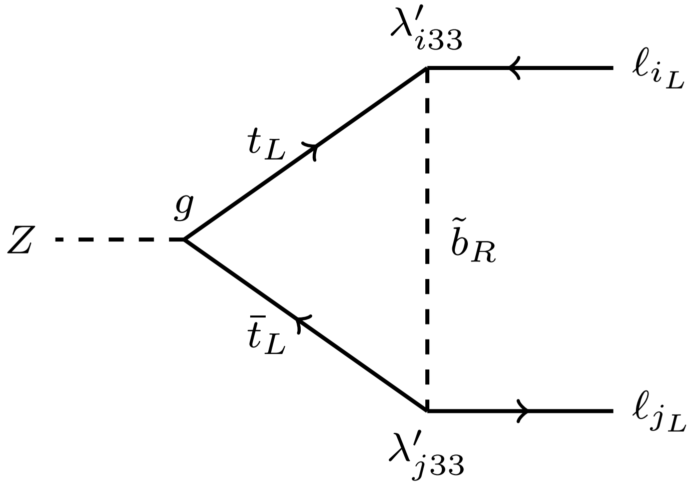

Figure A.4: Contribution to $Z \to \ell\bar{\ell}^{'}$ from λ' in RPV3.

This process gets modified by top-sbottom loops, as shown in Fig. A.4. A change in the Z decay from the SM prediction will affect the ratios of the vector and axial-vector couplings of the Z boson with different lepton flavors. Experimental measurements on these couplings are [151]

$$\left(\frac{g_V^\tau}{g_V^e}\right)_{\text{exp}} = 0.9588 \pm 0.02997\,, \tag{A.6}$$

$$\left(\frac{g_A^\tau}{g_A^e}\right)_{\text{exp}} = 1.0019 \pm 0.00145\,. \tag{A.7}$$

The contributions to these ratios from RPV3 are given by

$$\left(\frac{g_V^\tau}{g_V^e}\right)_{\text{SM+RPV}} = 1 - \frac{2\,\delta g_{\ell_3\ell_3}}{1-4\,s_w^2}\,,$$

$$\left(\frac{g_A^\tau}{g_A^e}\right)_{\text{SM+RPV}} = 1 - 2\,\delta g_{\ell_3\ell_3}\,,$$

where

$$\delta g_{\ell_i\ell_j} \simeq \frac{3y_t^2}{32\sqrt{2}G_F\pi^2}\frac{\lambda'_{i33}\lambda'_{j33}}{m_{\tilde{b}_R}^2}\left[\log\left(\frac{m_{\tilde{b}_R}}{m_Z}\right) - 0.612\right]\,. \tag{A.8}$$

Taking i, j both equal to 3 and using Eqs. (A.6) and (A.7), we derive a bound on the RPV3 parameter space, as shown by the violet-shaded region in Fig. 2.5.

A.5 $b \to s\gamma$

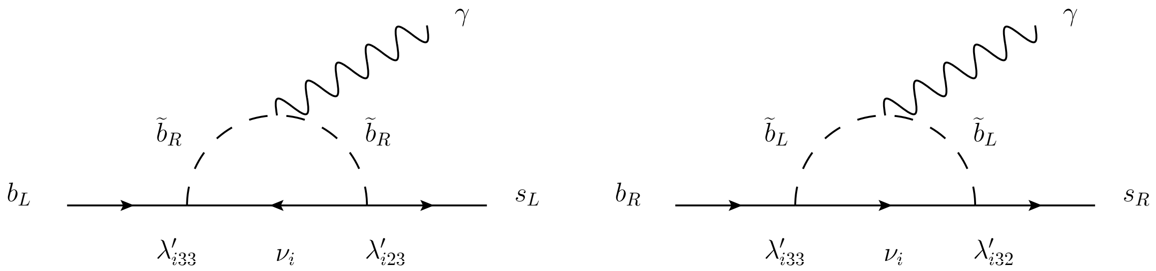

Figure A.5: Contribution to $b \to s\gamma$ from λ' couplings in RPV3.

The branching ratio of $b \to s\gamma$ has been measured [77] as:

$$\text{BR}(b \to s\gamma)_{\text{exp}} = (3.43 \pm 0.21 \pm 0.07) \times 10^{-4}\,, \tag{A.9}$$

which is consistent with SM [327]:

$$\text{BR}(b \to s\gamma)_{\text{SM}} = (3.36 \pm 0.23) \times 10^{-4}\,. \tag{A.10}$$

In RPV3, there are one-loop contributions involving both left- and right-handed sbottoms (see Fig. A.5). Comparing this to the difference between the experimental and SM results, we obtain the following bound at 95% CL:

$$|\lambda'_{223}\lambda'_{233}| \lesssim 0.025 \left(\frac{100\text{ GeV}}{m_{\tilde{b}_R}}\right)^{-2} \tag{A.11}$$

$$|\lambda'_{232}\lambda'_{233}| \lesssim 0.01 \left(\frac{100\text{ GeV}}{m_{\tilde{b}_L}}\right)^{-2} \tag{A.12}$$

This is shown by the grey-shaded region in Fig. 2.5.

Appendix B: Additional Kinematic Distributions

Additional kinematic observables can be used in order to enhance the sensitivity for a given model. For the RPV3 model considered in this work, we list a few of these and show the kinematic distributions of the signal (for three benchmark cases) and the SM backgrounds (shaded histograms) in Fig. B.1. This is to emphasize the future potential of the $\mu^+\mu^-\tau^+\tau^-$ channel at the HL-LHC. The variables considered here are:

- m^{max}: the maximum value of the invariant mass of a pair of a muon and the visible part of a hadronically decaying tau-lepton, $\tau_{\text{had}}^{\text{vis}}$, with opposite charges.[1] This observable is expected to peak close to the mass of the sneutrino for the signal.
- m^{min}: similar to the observable above, but with the minimum value instead.
- $(m^{\text{max}} - m^{\text{min}})/(m^{\text{max}} + m^{\text{min}})$: since the signal production includes two resonances with similar masses, we expect that the difference between the invariant masses of their decay products will be similar, different than the SM backgrounds.

---

[1] The charge of the hadronically decaying tau-lepton can be identified by the sum of charges of its decay products.

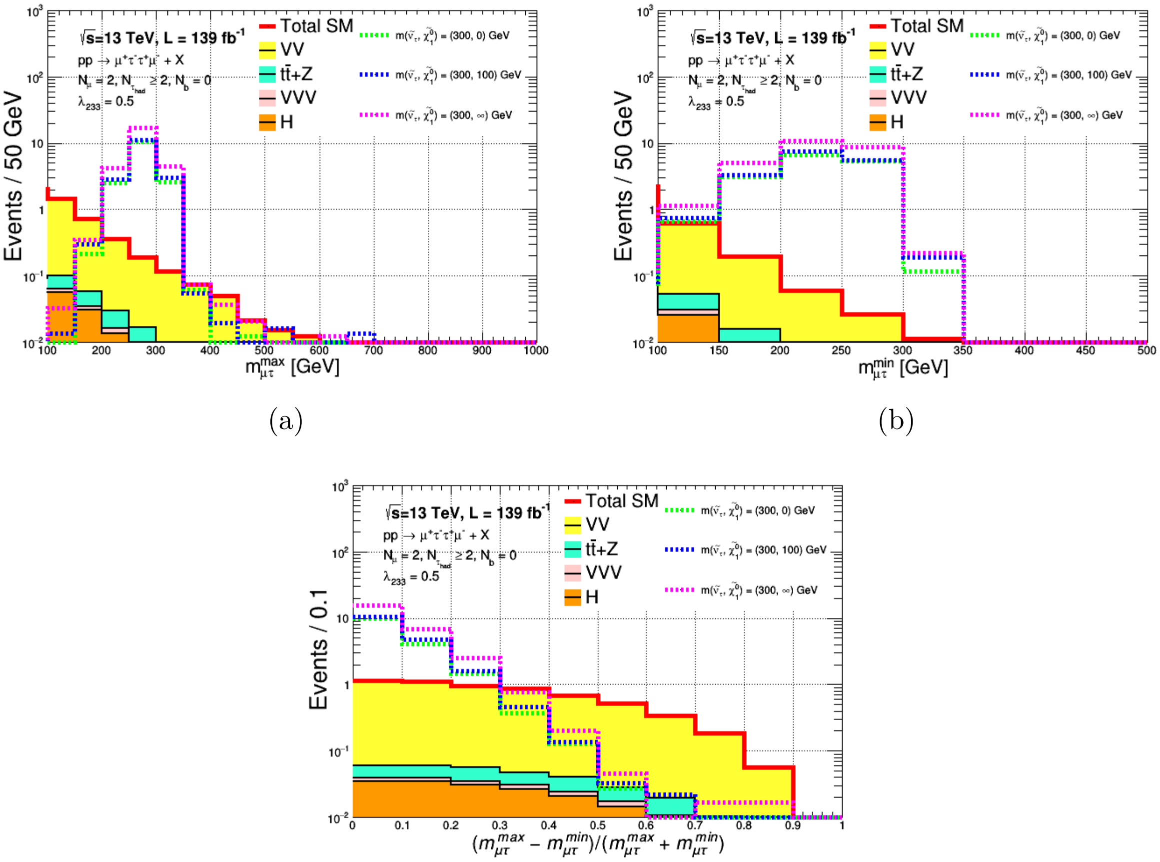

(a)

(b)

(c)

Figure B.1: Additional distributions that can be used in a dedicated analysis: (a) $m^{\max}$, (b) $m^{\min}$ and (c) $(m^{\max} - m^{\min})/(m^{\max} + m^{\min})$. All of the selections of SR2$^{\text{loose}}_{\text{bveto}}$-$\mu\mu$ and SR2$^{\text{tight}}_{\text{bveto}}$-$\mu\mu$ are implemented, as described in Tab. 3.1, beside the m_{eff} selection. Three signal points are presented by setting $m_{\tilde{\nu}_\tau} = 300$ GeV and $\lambda_{233} = 0.5$, for three different choices of $m_{\tilde{\chi}^0_1}$: with a very small value (0 GeV), 100 GeV, and a very large value (∞).